

https://dspace.org/

Synthesis and characterization of nitrogen-doped hollow carbon spheres/ Cu2S composites for potential application as counter electrodes in dye sensitized solar cells

Majola, Thelma

2022

https://hdl.handle.net/10539/33935

Downloaded from a DSpace repository. https://dspace.org/

Synthesis and Characterization of Nitrogen-doped hollow carbon spheres/ Cu_2S composites for potential application as counter electrodes in dye sensitized solar cells



UNIVERSITY OF THE
WITWATERSRAND,
JOHANNESBURG

A dissertation submitted to the Faculty of Science, University of the Witwatersrand, in partial fulfilment for the degree of

Master of Science

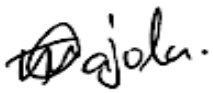
By

THELMA MAJOLA

549148

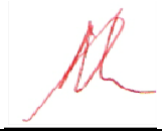


WITS
UNIVERSITY



Thelma Majola (Candidate)

01/2022
Date



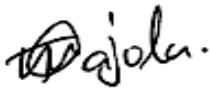
Supervisor

01/2022
Date

SUPERVISORS: DR ZIKHONA TETANA AND PROF NOSIPHO MOLOTO

Declaration

I declare that the work reported herein is my own independent work, submitted at the School of Chemistry, University of the Witwatersrand, Johannesburg. This work has not been submitted for any degree or examination in any other institution of higher learning.



Thelma Majola (Candidate)

/07/2021

Date

Abstract

Current solar cells have disadvantages that include weather dependency and high manufacturing costs. Dye-sensitized solar cells (DSSCs) have emerged as possible solutions for these drawbacks. Since it is predicted that the global warming effect will result in the sun emitting less energy. DSSCs have the added advantage of working in low-light conditions, and the ability to harness light energy from other devices. Although DSSCs have low production costs, their low efficiency due to the platinum (Pt) electrocatalyst limits their commercial implementation. DSSCs are made up of many components including dye, and counter electrode (CE). Modifications can be made on these components to improve efficiency and make the DSSC more eco-friendly. For instance, CE research has focused on finding substitute electrocatalysts. In this study copper sulfide (Cu_2S) and hollow carbon spheres (HCSs) have been considered as viable substitutes for Pt since they exhibit good electrocatalytic properties. Carbon materials have corrosion resistance towards iodine, and Cu_2S has superior oxidation resistance. Therefore, they can be used for electrolyte redox reactions at the CE in a DSSC. The properties of HCSs can be enhanced by making the carbon shell porous, increasing the number of carbon shells, or by doping the carbon shell with heteroatoms such as nitrogen (N). These modifications can improve the conductivity, surface area, adsorption, and electronic properties. For this research porous nitrogen doped single-shelled and double-shelled HCSs were synthesized.

To prepare the HCSs, a carbon shell was coated on the surface of the mesoporous silica spheres using the chemical vapour deposition method (CVD) with acetylene or toluene as carbon precursors at 900 °C for 1 h. Thereafter, the silica template was etched using 10 % HF at room temperature for 24 h. It was found that toluene produced HCSs with a higher surface area. Unexpectedly, the double-shelled HCSs were found to exhibit low surface areas than the single-shelled HCSs. Nitrogen doping improved the properties of both the single and double-shelled HCSs. The nitrogen-doped, single-shelled mesoporous hollow carbon spheres (N-HCS) showed better properties for electrocatalysis than the double-shelled HCSs. The Cu_2S nanoparticles were prepared using colloidal synthesis at 230 °C for 1 h with oleylamine (OLA) as the surfactant and 1-dodecanethiol (1-DDT) as the sulfur source. Different copper precursors were used which gave Cu_2S with varying compositions. Both precursors produced particles with a hexagonal morphology, however, copper (II) acetylacetonate ($Cu(acac)_2$) produced smaller particles (30 nm) compared to large particles (479 nm) from copper chloride (CuCl). A time study on the different copper sources showed a variance in nucleation and particle growth. The Cu_2S-HCS composites were prepared using OLA as the surfactant, with different percentages of Cu_2S and HCSs. The different composition mixtures were heated to 100 °C and then washed to remove the unreacted elements.

The synthesized materials were analyzed using various techniques. TEM showed the spherical morphology of HCSs, the hexagonal morphology of Cu_2S, and the successful formation of the composites. The surface area and porosity of the materials were measured using the BET technique. Graphitization of carbon and the phase composition of Cu_2S was analyzed using PXRD. The successful incorporation of N within the structure of the N-HCSs was confirmed using XPS. The electrocatalytic activities of the composites were investigated using CV,EIS, Tafel polarization, I-V and compared to Pt under similar conditions. The 75 wt% N-HCS: 25 wt% Cu_2S composite had higher current density, lower peak-to-peak separation, and high electrochemical double layer capacitive current, good adhesion to the FTO glass and great photovoltaic performance compared to Pt. This suggests that it was the better performing composite and has the potential to substitute Pt- CE in DSSCs.

Acknowledgments

My deepest gratitude to my supervisors Dr Zikhona Tetana and Prof Nosipho Moloto for their advice, support, and improving my scientific knowledge. Thankful for all the long nights spent going through my research and the valuable contributions.

A special thank you to Mrs Petra Dinham for her assistance with SEM images and EDX. Dr Rudolph Erasmus for his assistance with RAMAN measurements. I would also like to thank Ms Louise Mostert at CSIR NMISA for the XPS measurements and interpretation of the results. Thank you to Wits MMU unit for providing the microscopic instrumentation and expertise for XRD and TEM analysis. Completion of this work would not be possible without the School of Chemistry at the University of the Witwatersrand affording me the opportunity to carry out my research and the NRF funding my studies.

A huge thank you to the CATOMAT and NANO-WEB research groups for your inputs and for making my MSc journey memorable. Special thank you to Ms Grace Ngubeni, Dr Rudo Sithole, Dr Pumza Mente, Mr Zakhele Ndala, Mr Olusola Akinbami, and Prof Neil Coville for their assistance and corrections of my scientific writing.

I would like to thank my family for supporting me in pursuit of my dreams. A wholehearted thank you to my biggest supporter, my mother. Thank you for your constant encouragement during this challenging academic journey and for always believing in me. Your guidance and support did not go unnoticed. Lastly, thank you to God, my ancestors, and guardian angels for giving me strength throughout this academic journey.

Dedication

For my mother, late father and grandmothers.

Presentations

- Oral presentation at Nanomaterials for Water, Energy, Biomedical and Sensor Applications (NANO-WEBS) seminar held at Chemistry department, University of the Witwatersrand on the 27/08/2019
- Oral presentation at Catalysis Organometallics and materials' (CATOMAT) seminar held at Chemistry department, University of the Witwatersrand on the 06/09/2019
- Poster presentation at the 11th cross-faculty postgraduate symposium (WITS) 12/10/2020 to 14/10/2020. (Best poster 2nd place)
- Poster presentation at the Young STEM Online Poster symposium (SAIC) 17/11/2020 and 18/10/2020. (Best poster 1st place)
- Poster presentation at MSSA 2020 Online Workshop from 30/11/2020 to 3/12/2020. (Best Student Presentation Award)

Table of Contents

Declaration iii

Abstract iv

Acknowledgments vi

Dedication vii

Presentations viii

List of figures xi

List of schematics xiv

List of supplementary figures xv

List of tables xv

List of symbols and abbreviations xvi

Dissertation synopsis xviii

Chapter 1 1

GENERAL BACKGROUND 1

1.1 Introduction *1*

1.2 Problem statement *2*

1.3 Rationale *3*

1.4 Aims and objectives *4*

References *4*

Chapter 2 7

LITERATURE REVIEW 7

2.1 Carbon *7*

2.2 Metal sulfides *14*

2.3 Dye-sensitized solar cells (DSSCs) *21*

2.4 Carbon composites for use as counter electrodes in DSSCs *28*

References *31*

Chapter 3 45

SYNTHESIS AND CHARACTERIZATION OF POROUS NITROGEN-DOPED HOLLOW CARBON SPHERES 45

3.1 Introduction *45*

3.2 Experimental *49*

3.3 Results and discussion *52*

3.4 Conclusion *71*

References *71*

Chapter 4 76

COLLOIDAL SYNTHESIS AND CHARACTERIZATION OF COPPER SULFIDE NANOPARTICLES 76

4.1 Introduction *76*
4.2 Experimental *78*
4.3 Results and discussion *80*
4.4 Comparison of the resulting $Cu_{2-x}S$ nanostructures *94*
4.5 Conclusion *97*
References *97*

Chapter 5 102

PREPARATION, CHARACTERIZATION, AND ANALYSIS OF THE ELECTROCATALYTIC ACTIVITY OF N- HCS /CU2S COMPOSITES AS CE MATERIAL IN DSSCS 102
5.1 Introduction *102*
5.2 Experimental *104*
5.3 Results and discussion *107*
5.4 Conclusion *120*
References *120*

Chapter 6 127

GENERAL CONCLUSIONS AND RECOMMENDATIONS 127
6.1 Conclusions *127*
6.2 Recommendations *128*

Supplementary figures 129

List of figures

Figure 1.1: Graph showing the decline of electricity demand after lockdown was implemented for different countries (weather corrected). 1

Figure 2.1: Various molecular forms showing dimension categories for carbon nanostructures [9]. 7

Figure 2.4: Diagram showing different hollow carbon structures. 12

Figure 2.5: Diagram showing different morphologies of hollow carbon spheres and their possible uses. 13

Figure 2.6: Crystal structures of (a) the low-chalcocite), (b) high chalcocite (hexagonal), (c) cubic-chalcocite (cubic), (d) djurleite, (e) digenite, and (f) anilite. Blue and yellow represent copper and sulfur atoms respectively 16

Figure 2.7: Hexagonal unit cell showing the Cu-S system of triangular and tetrahedron coordination for copper (blue) and sulfur (yellow). 16

Figure 2.8: Descriptive diagram showing the relationship between bandgap energy and size of particles 17

Figure 2.9: Graphs (a-c) show bandgap dependence of copper sulfides with composition, size, and shape of nanostructures. 18

Figure 2.10: Graph shows the change in Gibbs free energy for clusters depending on their radius $\boldsymbol{rc}$. 19

Figure 2.11: Diagram showing LaMer plot for the generation of nuclei, nucleation, supersaturation and the successive growth of colloidal systems. 20

Figure 2.13: Diagram illustrating a cyclic voltammetry plot showing the cathodic potential (**Epc**) and current (**Ipc**). 24

Figure 2.14: An example of a Nyquist plot with an inset of the equivalent circuit for fitting the electrochemical impedance spectroscopy (EIS) data. 25

Figure 2.15: Diagram illustrating a Tafel polarization plot of a DSSC. 26

Figure 2.16: Plot of the current-voltage (I-V) curves of a solar cell in the dark and under illumination. 28

Figure 3.1: Different types of template materials that can be used for the synthesis of hollow materials [4]. 45

Figure 3.2: Nitrogen atom configurations in carbon materials: (1) pyridinic-N, (2) pyrrolic-N, and (3) quaternary-N.....48

Figure 3.5: Pristine silica (a) TEM micrograph, (b) particle size distribution (extracted from a low magnification image) and (c) SEM micrograph. 53

Figure 3.6: (a) TEM micrographs of mesoporous silica micrographs and (b) particle size distribution (extracted from a low magnification image). 54

Figure 3.7: BET surface area analysis of pristine and mesoporous silica spheres.....55

Figure 3.8: TEM micrographs of hollow carbon spheres synthesized from pristine silica with different carbon sources (a) acetylene, (b) toluene and their respective particle size distributions (c) and (d).....56

Figure 3.9: TEM micrographs of hollow carbon spheres synthesized from pristine silica with different carbon sources (a) acetylene, (b) toluene, their respective particle size distributions (c) and (d) and SEM micrographs (e) acetylene, (f) toluene. 57

Figure 3.10: BET surface area analysis of mesoporous hollow carbon spheres carbonized by toluene (red) and acetylene (black). 58

Figure 3.11: TEM micrographs of (a) SiO_2@m- SiO_2, (b) double-shelled m-SiO_2.....59

Figure 3.12: Double-shell mesoporous hollow carbon spheres micrographs (a-e) TEM, (f) SEM, and (g-h) the particle size.....60

Figure 3.13: Powder X-ray diffraction patterns of single and double-shelled mesoporous hollow carbon spheres.....61

Figure 3.14: Raman spectra of single and double-shelled mesoporous hollow carbon spheres. ...62

Figure 3.15: (a) Thermograms and (b) corresponding derivative profiles of unannealed single and double-shelled mesoporous hollow carbon spheres. 63

Figure 3.16: a) Thermograms and (b) corresponding derivative profiles of annealed single and double-shelled mesoporous hollow carbon spheres. 64

Figure 3.17: BET surface area analysis of nitrogen-doped mesoporous hollow carbon spheres. .65

Figure 3.18: (a) XPS survey spectrum of N-doped single-shelled HCS and (b)-(d) high-resolution spectra of nitrogen, carbon, and oxygen, respectively. 70

Figure 4.2: Simplified schematic diagram showing the synthesis sequence for $Cu_{2-x}S$ nanoparticles. 79

Figure 4.3: Synthesized $Cu_{2-x}S$ TEM micrographs at different reaction times (a) 10 min (b) 30 min, and (c) 60 min. The particle size distribution for the synthesized particles at 60 min reaction time. 81

Figure 4.4: Powder X-ray diffractogram patterns for synthesized $Cu_{2-x}S$ particles at different reactions times (10, 30, and 60 min) with the corresponding peak matching PXRD spectra for $Cu_{1.97}S$ and from the XRD database, $Cu_{1.8}S$ (JCPDS 622980). 83

Figure 4.5: (a) UV-vis absorption spectra of synthesized Cu2-xS particles at different reaction times, using CuCl as a Cu precursor and (b) their corresponding Tauc plots. 85

Figure 4.6: Near-infrared spectra of $Cu_{2-x}S$ nanostructures, showing absorption energy with relation to increasing copper deficiency. 85

Figure 4.7: EDX spectrum and corresponding SEM micrograph of synthesized $Cu_{2-x}S$ at 60 min. 87

Figure 4.8: Synthesized $Cu_{2-x}S$ TEM micrographs (a)-(c) and (d)-(e) particle size distribution for particles at 30 and 60 min reaction time using $Cu(acac)_2$ as a precursor. 89

Figure 4.9: Particle size distribution for synthesized $Cu_{2-x}S$ particles at 30 and 60 min reaction time using $Cu(acac)_2$ as a precursor. 90

Figure 4.10: TEM micrograph of different orientations for synthesized $Cu_{2-x}S$ at 60 min reaction time. 90

Figure 4.11: Powder X-ray diffraction patterns for as-synthesized Cu2-xS particles at different reactions times and the corresponding peak matching PXRD spectra for $\boldsymbol{\alpha}$ and $\boldsymbol{\beta}$ Cu_2S. 91

Figure 4.12: a) UV-Vis absorption spectra of synthesized Cu2-xS particles at different reaction times, using $Cu(acac)_2$ as a Cu precursor and (b) their corresponding Tauc plots. 93

Figure 4.13: EDX spectrum and corresponding SEM micrograph of synthesized $Cu_{2-x}S$ at 60 min. 94

Figure 4.14: Diagram illustrating different reaction systems when nucleation occurs (a) at random and (b) all at once, and how the nuclei (•) grows with increased reaction time. 96

Figure 4.15: Diagram showing the change in bandgap due to copper vacancies. 97

Figure 5.1 Diagram of a cyclic voltammetry plot, showing the redox reaction of the triiodide/iodide electrolyte. 104

Figure 5.2: Diagram illustrating the cell set-up for cyclic voltammetry analysis. 106

Figure 5.3: Structure of an assembled DSSC for current-voltage analysis of solar cell. 107

Figure 5.4: TEM micrographs of (a) 25 wt% N-HCS, (c) 50 wt% N-HCS and (e) 75 wt% N-HCS with their corresponding SEM micrographs (b, d, and f). 108

Figure 5.5: XPS survey spectrum for the 75 wt% N- HCS composite. 110

Figure 5.7: High resolution XPS spectra of (a) C 1s, (b) O 1s, (c) Cu 2p and (d) S 2p for the 75 wt% N-HCS composite. 111

Figure 5.8: Cyclic voltammograms for (a) Pt-CE, (b) Cu2S (c) N-HCS, (d) 75wt% N-HCS, (e) 50wt% N-HCS and (f) 25 wt% N-HCS counter electrode at various scan rate after 10 scans. ... 112

Figure 5.9: Capacitive current versus scan rate for the prepared composites, Pt, Cu_2S, and N-HCS electrocatalysts. 114

Figure 5.10: Nyquist plots of EIS for the symmetric cells with their electrochemical equivalent circuit for Pt, Cu_2S, N-HCS, 75 wt% N-HCS, 50 wt% N-HCS, and 25 wt% N-HCS. 116

Figure 5.11: Tafel plot of the Pt and the synthesized materials: Cu_2S, N-HCS, 75 wt% N-HCS, 50 wt% N-HCS, and 25 wt% N-HCS. 117

Figure 5.12: Current-voltage characteristic curves for the DSSCs of Pt, 75 wt% N-HCS, and 25 wt% N-HCS. 119

List of schematics

Figure 2.2: Schematic diagram showing the arrangement of a vertical CVD reactor. 10

Figure 2.3: Schematic diagram showing the arrangement of a horizontal CVD reactor. 11

Figure 2.12: Schematic diagram of a dye-sensitized solar cell. 22

Figure 3.3: Schematic diagram depicting the synthesis of single-shelled mesoporous hollow carbon spheres. 50

Figure 3.4: Schematic diagram depicting the synthesis of double-shelled mesoporous hollow carbon spheres. 51

Figure 4.1: Schematic diagram showing the synthesis sequences of the top-down and bottom-up approaches. 77

Figure 5.6: Schematic diagram showing the layering of elements in the composite material. 110

List of supplementary figures

Figure S4.1: XRD pattern of as-synthesized copper sulfide particles at various reaction times of 10, 30, and 60 min using CuCl as a Cu precursor. 129

Figure S4.2: XRD pattern of as-synthesized copper sulfide particles at various reaction times of 10, 30, and 60 min using $Cu(acac)_2$ as a Cu precursor. 129

List of tables

Table 2.1: Electrocatalytic parameters and photovoltaic performance of various carbon CE materials. ..... **Error! Bookmark not defined.**

Table 3.1: Pore volumes, BET surface areas and pore sizes of pristine, and mesoporous silica spheres 55

Table 3.2: Pore volumes, BET surface areas, and pore sizes of mesoporous hollow carbon spheres 58

Table 3.3: The I_D/I_G ratios of single and double-shelled mesoporous hollow carbon spheres. 62

Table 3.4: Pore volumes, BET surface areas, and pore sizes of single and double-shelled mesoporous hollow carbon spheres. 66

Table 3.5: Elemental nitrogen content of doped single and double-shelled mesoporous hollow carbon spheres 68

Table 3.6: XPS data of N-doped single-shelled mesoporous hollow carbon spheres 70

Table 5.1: Summary of the atomic composition stoichiometric assignments obtained from the fitting of the XPS spectra reported in Fig. 5.3 for the 75 wt%, 50 wt%, and 25 wt% N-HCS composites 112

Table 5.2: Summary of composites and Pt CE current densities and their peak-to-peak separations 114

Table 5.3: Electrochemical measurements obtained from EIS and Tafel polarization curves for Pt and the synthesized materials: Cu_2S, N-HCS, 75 wt% N-HCS, 50 wt% N-HCS, and 25 wt% N-HCS 118

Table 5.4: Current-voltage measurements for the DSSCs of Pt, 75 wt% N-HCS, and 25 wt% N-HCS 119

List of symbols and abbreviations

PV - photovoltaic

HCS - hollow carbon spheres

HCN -Hollow carbon nanomaterials

Pt - platinum

ZnS - Zinc Sulfide

$ZnIn_2S_4$ - Zinc indium sulfide

CdS - Cadmium sulfide

MoS_2 - molybdenum disulphide

Cu_2ZnSnS_4 - Copper zinc tin sulfide

Bi_2S_3 - Bismuth sulfide

Cu_2S - copper sulfide

CVD - chemical vapour deposition

C - carbon

O - oxygen

H - hydrogen

N - nitrogen

Cu - copper

S - sulfur

Cl – chloride

Ag - silver

Si - silicon

SS - single-shelled

DS - double-shelled

TiO_2 - titanium dioxide (TiO_2)

CB- Conduction band

VB - Valence band

CE - Counter-electrode

DSSC - Dye-sensitised solar cell

TCO - transparent conductive oxides

I_3^- / I^- - triiodide/iodide

FTO - Fluorine doped tin oxide

CV - Cyclic voltammetry

C_{18}TMS - n-octadecyltrimethoxysilane

CTAB - cetyltrimethylammonium bromide

N-HCS - nitrogen-doped hollow carbon sphere

DS-mHCS - double-shelled mesoporous hollow carbon spheres

SS-mHCS - single-shelled mesoporous hollow carbon spheres

PXRD – powder X-ray diffraction

TGA- thermogravimetric analysis

DTG - differential temperature gradient

BET - Bruanauer–Emmett–Teller

SEM - Scanning electron microscopy

TEM - Transmission electron microscope

XPS - X-ray photoelectron spectroscopy

1-DDT - 1-Dodecanethiol

OLA - Oleylamine

UV-Vis - Ultraviolet-visible spectrophotometry

EDX - Energy-dispersive X-ray spectroscopy

HOMO - Highest occupied molecular orbital

ITO - Indium-doped tin oxide

LUMO - Lowest unoccupied molecular orbital

E_g - Energy gap

I_D/I_G - intensity ratio of the D and G bands

PGM - platinum-group metals

TMC - Transition metal chalcogenides

NS - nanostructures

NP - Nanoparticle

CuCl - Copper chloride

$Cu(acac)_2$ - copper(II)acetylacetonate

α - alpha

β - beta

wt% - percentage weight

I_p - peak current

E_{pp}- peak-to-peak separation

WE - working electrode

RE - reference electrode

EIS - Electrochemical Impedance Spectroscopy

R_{ct} - charge transfer resistance

R_s - ohmic resistance

CPE - constant phase angle

V - potential

J_0 - exchange current density

J_{lim} - limiting diffusion current density

$I-V$ - current -voltage

J_{sc} - short-circuit current density

V_{oc} - open-circuit voltage

FF - Fill factor

PCE - Power conversion efficiency

P_{in} - Power in

P_{max} - Power max

Z_w - Warburg impedance

R_{sh} - shunt resistance

SiO_2 - silica

$Si(OR)_4$ - silicon alkoxide

TEOS - tetraethylorthosilicate

HCl – hydrochloric acid

NH_3 – ammonia

CH_3CN - Acetonitrile

HF - hydrofluoric acid

m- SiO_2 - mesoporous SiO_2

Dissertation synopsis

The aim of this research was to synthesize varied composites of copper sulfide and hollow carbon spheres that are porous and nitrogen doped. Evaluate their photovoltaic properties using cyclic voltammetry, electrochemical impedance spectroscopy, Tafel polarization and current-voltage analysis. Determine their potential use as counter electrodes in dye-sensitized solar cells as replacements for the expensive Pt counter electrode. A summary of the dissertation is given below:

Chapter 1: comprises of a brief background on the importance of dye-sensitized solar cells, and includes the problem statement, rationale, aims and objectives of the study.

Chapter 2: is the literature review of carbon, hollow carbon materials, metal sulfides, their properties and synthesis routes. It also includes a short assessment of DSSCs, counter electrodes and the use of hollow carbon spheres and metal sulfides as counter electrodes. Reviews on the electrochemical analysis techniques used to evaluate photovoltaic performances.

Chapter 3: focuses on the chemical vapour deposition synthesis of porous, nitrogen-doped single and double-shelled hollow carbon spheres and their post-synthesis nitrogen doping. Their characterisation through the variation of reaction parameters.

Chapter 4: focuses on the colloidal synthesis of copper sulfides**.** Reports on the effect of the copper precursor and reaction time on the morphology and properties of the synthesized Cu_2S.

Chapter 5: reports on the synthesis of the composite materials and evaluation of their electrocatalytic properties.

Chapter 6: gives a general summary on the research work, investigations of the synthesized materials, and conclusions. The chapter also gives recommendations for further studies.

Chapter 1

General background

1.1 Introduction

Electricity is an integral part of our day-to-day lives in the modern world of the 21st century. Industrial growth and the insatiable appetite for modern technology, smart living, and the increase in human population continue to rise exponentially. The development of the world over the years has shifted more to digitization even in the most rural of areas [1], this has resulted in unquenchable energy consumption as the energy demand increases at an unmanageable rate. Although the global COVID-19 pandemic resulted in a decline in energy consumption (**Figure 1.1**) due to industrial shutdown and a decrease in service delivery during lockdown, there was an increase in the renewable energy sector [1]–[3]. The Texas blackout that occurred at the beginning of this year during the city's winter months. Death of patients on oxygen machines in South Africa due to electrical outages [4], are both incidents that have reinforced the need for reliable energy. Renewable energy supplies that are environmentally friendly have become a priority for both under-developed and first world countries.

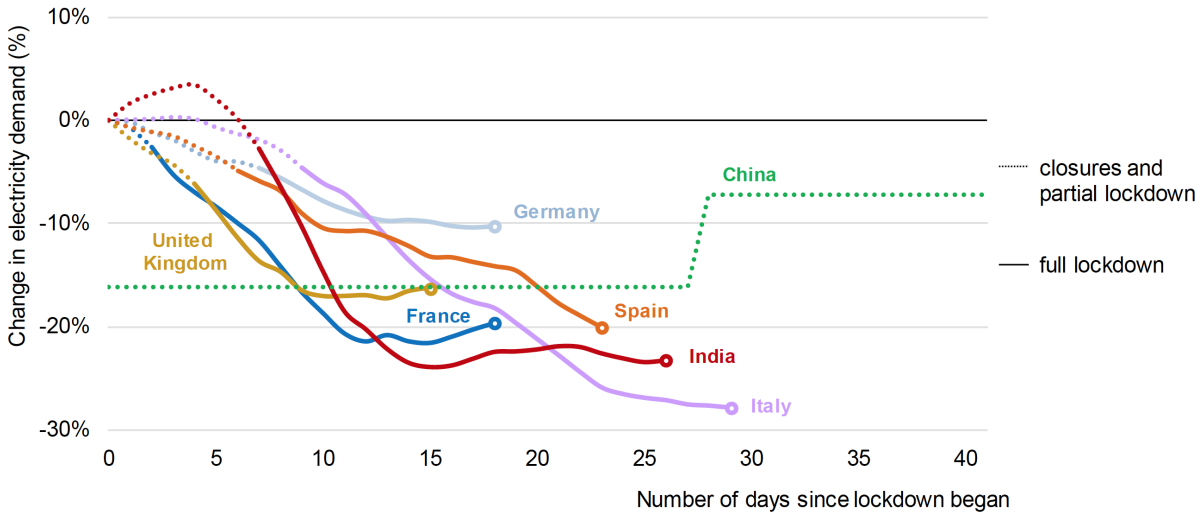


Figure 1.1: Graph showing the decline of electricity demand after lockdown was implemented for different countries (weather corrected) [3].

The dangers of this country's major reliance on the burning of biomass and fossil fuels has resulted in a negative environmental impact. Greenhouse gases are emitted during the energy deriving processes and this has been followed by irreparable damage to this planet's natural bionetwork. Over the years, the energy sector has constantly invented or reinvent sustainable energy sources that are also renewable, in a bid to preserve the natural resources that are currently being used and introduce clean living. Solar cells also known as photovoltaic devices (PV) continue to be the most advantageous and greenest form of renewable energy as they convert readily available sunlight into electricity. The semiconducting materials that are used in solar cell technology facilitate this. Under the umbrella of the first-generation solar cells, silicon materials were found to have high efficiency and high production costs [5],[6]. This catapulted more research into finding materials that have high efficiency and lower production costs [7]. Second-generation solar cells reduced production costs by using thin-film technology. Non-silicon materials such as cadmium telluride (CdTe) and copper indium gallium selenide (CIGS) were some of the materials that were found to have good efficiencies [5]. However silicon still rivalled all of the materials due to its high absorption rate [5], [8], [9], which is an important factor as it determines the efficiency of the solar cell [10].

Although the goal of production cost reduction was accomplished, the materials discovered did not have high conversion efficiencies that surpassed the silicon material of the first generation. Third-generation solar cells aim to enhance the electrical performances of second-generation thin-film technology and to further reduce production costs. This is done by using nanotechnology and recently discovered compounds such as nanocrystalline films, multilayer inorganics, active quantum dots, and polymers [11], [12]. Dye-sensitized solar cells (DSSCs) have emerged as a promising 3rd generation solar cell due to their low cost, ability to work in low-light conditions, and harness energy from other lights [13]. This makes them possible to use in countries that have overcast weather.

1.2 Problem statement

According to the 2020 annual report by the department of energy for South Africa, Africa's energy demand is twice that of the global rate [14]. In South Africa, the burning of biomass and fossil fuels represents over 90 % of the electrical energy generated. Given that the country has a major dependency on fossil fuels and is still unable to sufficiently provide the country with a reliable energy supply, alternative energy sources are needed.

With the energy demand increasing and more people shifting to the use of solar cells for cleaner living, the prices of the current solar cells continue to increase [15]. To combat these challenges, alternative renewable energy devices can be employed. Extensive research has gone into finding readily available materials and cheaper alternatives to depleting noble materials such as platinum (Pt) which is being used as a counter electrode (CE) material in dye sensitized solar cells (DSSC) [16]. Although this third-generation technology has shown promise, there is still a need for improvement on the efficiencies, commercialization, and energy capture within the solar spectrum for the materials used. A viable alternative to the low efficiencies and high cost of Pt-CE is needed.

1.3 Rationale

According to the Department of Energy's annual performance plan (2020/21) and its strategic plan (2020-2025) [14], [17], energy is a fundamental part of our growing economy, and to meet this country's demand, it is imperative for South Africa to grow its energy supply. This gives scientists the critical task of assisting the energy sector with materials or devices that can support the economic expansions and address the unreliability of our electricity supply. Therefore, the materials suggested in our research and the devices in which they will be used can support the nation's energy goals. The versatility of DSSC to be used in low-light countries and use energy from other light devices, makes it an expandible market that was valued at 90.5 million in 2019 and is set to have a 12.4 % increase by 2027 [18]. Social, economic, health, and academic sectors can be impacted by this research. As more knowledge and understanding of the materials synthesized and their potential applications will be explored. The energy demand crisis will be combated, aiding in social and economic improvement.

As the goal of this research is to synthesize environmentally friendly materials, there would be a reduction in pollution resulting in better environmental and human health [19]. The proposed materials are the use of doped hollow carbon spheres and copper sulfide (Cu_2S) composite material as a substitute for platinum-based counter electrodes in dye sensitized solar cells. The combination of their electrocatalytic properties can rival those of Pt-CE and both materials are non-toxic and considered cheaper alternatives to Pt.

1.4 Aims and objectives

This research aims to prepare both single-shelled and double-shelled hollow carbon spheres that are nitrogen-doped and possess mesoporous qualities. The horizontal chemical vapour deposition (CVD) technique will be used to obtain the carbon structures. Different parameters such as carbon and nitrogen sources will be altered to investigate their effect and obtain the carbon with promising catalytic properties. Synthesis of copper sulfide will be done using the colloidal synthesis route and the copper precursors will be altered to investigate their effect on the shapes and sizes of the particles with respect to reaction time. Lastly different weight percentages of the carbon and copper sulfide materials as composites will be prepared. The electrochemical properties of the composites will be investigated using cyclic voltammetry for application as CEs in dye-sensitized solar cells.

To achieve these aims the following objectives were implemented:

- Synthesis of mesoporous single-shelled and double-shelled hollow carbon spheres using the CVD method with different carbon precursors (acetylene or toluene) and mesoporous silica as the sacrificial template.
- Investigation of the effect of different carbon precursors.
- Nitrogen doping of the synthesized mesoporous single-shelled and double-shelled hollow carbon spheres using different nitrogen sources (acetonitrile and ammonia).
- Investigation of the effect of different nitrogen sources.
- Colloidal synthesis of copper sulfide particles and investigate the effect of different copper precursors.
- Preparation of the different compositions of the carbon and copper sulfide composites.
- Investigation of the electrochemical properties of the composites and their potential use as alternative counter electrode material in dye-sensitized solar cells.

References

[1] IEA, “Digitalization & Energy,” *Digitalization & Energy*, 2017. [Online]. Available: https://www.iea.org/reports/digitalisation-and-energy. [Accessed: 15-Jan-2021].

[2] I. Santiago, A. Moreno-Munoz, P. Quintero-Jiménez, F. Garcia-Torres, and M. J. Gonzalez-Redondo, “Electricity demand during pandemic times: The case of the COVID-19 in Spain,” *Energy Policy*, vol. 148, no. May 2020, 2021.

[3] IEA, “Global Energy Review 2020,” *Global Energy Review 2020*, 2020. [Online]. Available: https://www.iea.org/reports/global-energy-review-2020. [Accessed: 29-Jan-2021].

[4] “Emergency oxygen tanks are sold out – as load shedding cripples home-use concentrators.” [Online]. Available: https://www.businessinsider.co.za/emergency-oxygen-tanks-are-sold-out-as-load-shedding-cripples-home-use-concentrators-2021-1. [Accessed: 27-Jan-2021].

[5] V. V. Tyagi, N. A. A. Rahim, N. A. Rahim, and J. A. L. Selvaraj, “Progress in solar PV technology: Research and achievement,” *Renew. Sustain. Energy Rev.*, vol. 20, pp. 443–461, 2013.

[6] C. Becker, T. Sontheimer, S. Steffens, S. Scherf, and B. Rech, “Polycrystalline silicon thin films by high-rate electronbeam evaporation for photovoltaic applications - Influence of substrate texture and temperature,” *Energy Procedia*, vol. 10, pp. 61–65, 2011.

[7] J. A. Luceño-Sánchez, A. M. Díez-Pascual, and R. P. Capilla, “Materials for photovoltaics: State of art and recent developments,” *Int. J. Mol. Sci.*, vol. 20, no. 4, p. 976, 2019.

[8] B. Parida, S. Iniyan, and R. Goic, “A review of solar photovoltaic technologies,” *Renew. Sustain. Energy Rev.*, vol. 15, no. 3, pp. 1625–1636, 2011.

[9] T. D. Lee and A. U. Ebong, “A review of thin film solar cell technologies and challenges,” *Renew. Sustain. Energy Rev.*, vol. 70, no. September 2015, pp. 1286–1297, 2017.

[10] R. Santbergen and R. J. C. van Zolingen, “The absorption factor of crystalline silicon PV cells: A numerical and experimental study,” *Sol. Energy Mater. Sol. Cells*, vol. 92, no. 4, pp. 432–444, 2008.

[11] W. A. Badawy, “A review on solar cells from Si-single crystals to porous materials and Quantum dots,” *J. Adv. Res.*, vol. 6, no. 2, pp. 123–132, 2015.

[12] K. D. G. I. Jayawardena, L. J. Rozanski, C. A. Mills, M. J. Beliatis, N. A. Nismy, and S. R. P. Silva, “‘Inorganics-in-Organics’: Recent developments and outlook for 4G polymer solar cells,” *Nanoscale*, vol. 5, no. 18, pp. 8411–8427, 2013.

[13] W. Soutter, “What is a Dye-Sensitized Solar Cell ?,” 2014. [Online]. Available: http://www.azonano.com/article.aspx?ArticleID=3175. [Accessed: 29-Jan-2021].

[14] DMRE, “Department of mineral resources and energy, South Africa 2020/21.” [Online]. Available: http://www.energy.gov.za/files/aboutus/DMRE-Annual-

Performance-Plan-2020-2021.pdf. [Accessed: 05-Jan-2021].

[15] "Global supply chain squeeze, soaring costs threaten solar energy boom." [Online]. Available: https://www.engineeringnews.co.za/article/global-supply-chain-squeeze-soaring-costs-threaten-solar-energy-boom-2021-06-09. [Accessed: 15-Jun-2021].

[16] J. Wu *et al.*, "Counter electrodes in dye-sensitized solar cells," *Chem. Soc. Rev.*, vol. 46, no. 19, pp. 5975–6023, 2017.

[17] "DMRE Strategic plan 2020–2025," 2020. [Online]. Available: http://www.energy.gov.za/files/aboutus/DMRE-Strategic-Plan-2020-2025.pdf. [Accessed: 05-Jan-2021].

[18] "Dye Sensitized Solar Cell Market Size Worth $231.1 Million By 2027." [Online]. Available: https://www.grandviewresearch.com/press-release/global-dye-sensitized-solar-cell-market. [Accessed: 27-Nov-2020].

[19] M. Markiewicz, C. Zalitis, and A. Kucernak, "Performance measurements and modelling of the ORR on fuel cell electrocatalysts - The modified double trap model," *Electrochim. Acta*, vol. 179, pp. 126–136, 2015.

Chapter 2

Literature review

2.1 Carbon

The diversity of carbon uses, structures, and sources makes it a unique element that has been described as the basis of all forms of life [1]. The unique capability of a carbon (C) element to connect with itself through sp^3 (C-C) and sp^2 (C=C) hybridization [2] to produce carbon forms that have a variety of possibilities makes it an interesting research material. The introduction of buckminsterfullerene in the 80s opened an area of carbon science research that has continued to grow exponentially over decades. Due to more configurations being discovered from multi-walled carbon nanotubes [3] to carbon nano-onions [4]. Depending on the arrangement of the carbon framework, the formed materials can be classified into three categories which are graphitic, diamond, and amorphous carbon [5]. Amorphous carbon is made up of localized of π-electrons and short-range orders with different inter-atomic bonding and/distance [6]. Diamond-like carbon is an amorphous material that is hard and largely made up of sp^3 carbon bonded to some hydrogen atoms [7]. Graphitic carbon is soft with Van der Waals forces present in-between the layers and strong covalent bonds in the carbon plane [5]. The dimensionalities of carbon also vary with 0D, 1D, 2D, and 3D [1], [8]–[10] (**Figure 2.1**) this expands the range of carbon materials that can be synthesized as they would need to be classified by both their dimensions and carbon atom arrangement.

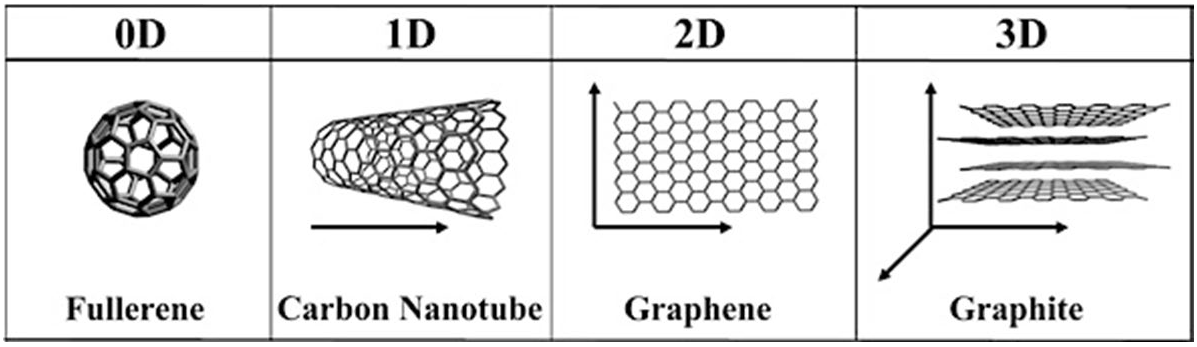


Figure 2.1: Various molecular forms showing dimension categories for carbon nanostructures [9].

Depending on the carbon-to-carbon bonding, Mhlanga *et al.* stated that carbon materials have exceptional qualities. They are thermally conductive [11], lightweight, non-toxic, the strongest synthesized materials when in their tubular form [12]. The surface can be chemically altered to enhance its functionality [13], and they can act as conductors, semiconductors, or insulators. To prepare these materials, different techniques can be employed subject to the classification, application, and structure quality desired.

2.1.1 Synthesis of carbon materials

Some of the synthesis methods include arc discharge [14], this technique was discovered by Iijima in 1991 [15] and was used to produce carbon nanotubes. An arc is generated using constant current at both the anode and cathode electrodes, which can be arranged vertically or horizontally. The anode electrode contains the carbon precursor; the current of the arc produces a plasma at very high temperatures causing the precursor to convert into a vapour that drifts towards the cathode where it cools. The carbon nanotubes are collected at the cathode and purified. Another high-quality carbon synthesis technique is laser ablation [3], [16], the reaction takes place in a quartz tube where a pulsed laser is concentrated on the heated carbon target. The resulting vapours are carried to a cooled collector by an inert gas such as argon and the condensed carbon is collected and purified.

For the simple one-step synthesis of carbon microspheres, hydrothermal synthesis can be used [17]. Different types of biopolymers, mono-, di-, and polysaccharides, biomass, and cellulosic carbohydrates [18] can be used as carbon sources, depending on the properties desired for the microspheres. At mild temperatures and pressure, the reaction occurs in a sealed autoclave, and carbonization of the carbon sources occurs through dehydration or polymerization [19]. The temperature, pressure, and reagents are used to determine the graphitization of the synthesized carbon [20]. The exfoliation method has been employed to extract graphene from natural graphite. Through this technique, large quantities of graphene can be produced from the bulk graphite using chemical or mechanical exfoliation. Solvents such as acids [21] are used as chemical exfoliants and mechanical forces through stirring or shaking [22] are employed for physical separation of the layered materials. Both procedures are used to weaken the van der Waals interactions between the graphite layers resulting in graphene sheets [23].

In comparison to the synthesis techniques described above, the chemical vapour deposition (CVD) route can be used to fabricate a variety of carbon materials such as graphene [24], carbon nanotubes [25], carbon nano-anions [26], and different morphologies of carbon spheres [27]–[29]. To generate a substantial amount of solid phase carbon materials with high performance and high quality [30], the CVD method is used.

2.1.2 Chemical vapour deposition (CVD)

The introduction of CVD can be traced back to de Lodyguine [31] in the 1890s who deposited tungsten on carbon lamp filaments, however, the work of de Boer and van Arkel [32] modified the CVD method by using high temperatures for the process. CVD can be described as the decomposition of volatile precursor/s at high temperatures resulting in a film of solid material forming on the substrate. The precursors are delivered as gases to the reaction chamber and as they pass through the reactor, they encounter the heated substrate. A reaction occurs and a layer of carbon is deposited, an inert gas such as argon (Ar) or nitrogen (N_2) is used as diluent gas during the reaction [33]–[35]. Different parameters such as reaction time, substrate choice, precursor, diluent gases, reaction temperatures, and the rate of flow for the gases are all important parameters during a CVD reaction as they determine the type of carbon material synthesized and its growth.

The carbon layer deposited on the substrate surface is formed through nucleation and growth. When the reaction occurs between the substrate and precursor gases stable nuclei consisting of some carbon atoms form on preferred sites of the substrate surface [36]. As the reaction proceeds, there is diffusion and adsorption of carbon atoms on the substrate surface. Growth occurs through the addition of C atoms from the precursor gas, and from surface diffusion across the uncovered portions of the substrate [36]–[38]. Therefore, the substrate used is important as the deposit to substrate adherence can determine the surface area or shape of carbon material. Saeed *et al.* found that there is continuous growth as the reaction time increases, only up to a certain ideal time, thereafter the carbon layers begin to disintegrate [39]. Chowdhury *et al.* found that an increase in the precursor gas flow rate increased the carbon deposition [40]. In the experimental work done by Tewari, it was deduced that different diluent gases affect the growth of the carbon material with Ar being the better diluent gas [41].

Temperature affects the deposition and coating morphologies of a material. CVD reactions require high temperatures for a reaction to occur, however, temperatures should not exceed 1000 °C as this results in thermal degradation of the synthesized carbon [42], [43]. Although the horizontal orientation of CVD is widely used for the synthesis of carbon, the vertical orientation is possible. This orientation is mainly used for the synthesis of solid carbon spheres [44]. For spheres with a small diameter of less than 10 nm the vertical CVD (**Figure 2.2**) is employed. These are also known as carbon dots (CDots) and are produced due to the short reaction time of the carbon precursors in the reactor [45], [46]. To achieve spheres with even smaller diameters the reaction chamber can be shortened to reduce the carbon precursors dwelling time in the chamber [47]. For carbon spheres with a larger diameter, horizontal CVD (**Figure 2.3**) is used due to a longer reactivity time.

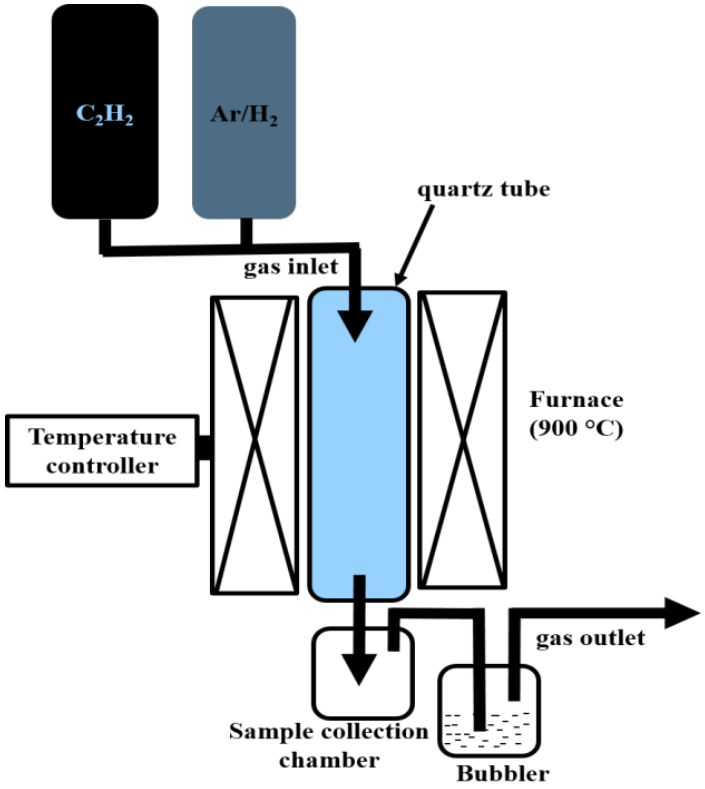


Figure 2.2: Schematic diagram showing the arrangement of a vertical CVD reactor [44].

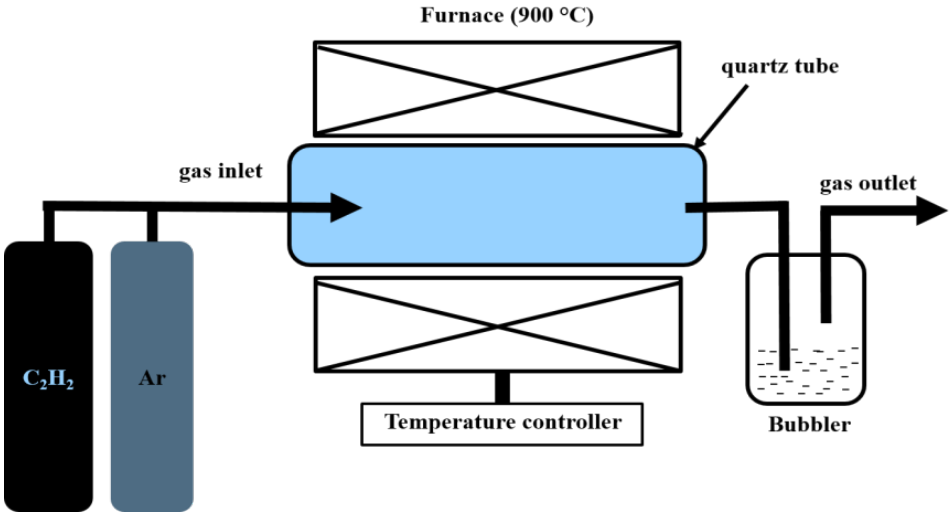


Figure 2.3: Schematic diagram showing the arrangement of a horizontal CVD reactor [44].

2.1.3 Hollow carbon nanomaterials (HCN)

The CVD method can also be used to synthesis hollow carbon structures which have gained traction in recent years due to their morphologies. The novelty of possessing an inner cavity that could be used to encapsulated other elements and an outer shell that can exhibit porous properties has made these structures an interesting area of research. Gangatharan *et al.* built helical carbon fibers inside hollow carbon spheres, using copper (Cu) as a catalyst [48] and Zhang *et al.* were able to confine Iron (Fe) -Nickel (Ni) nanoparticles inside a hollow nanobox [49]. Different studies have shown that carbon structures with a hollow center exhibit outstanding qualities for energy conversion and storage, catalysis, electric conductivity, and biomedical uses due to their interior voids and tunable shells [50]–[52]. Hollow carbon structures can be synthesized through the template-free method or with the use of templates to obtain the desired outer shape. The template-free method also known as the self-templating method is used when the precursor or raw materials with the desired structure are the carbon sources and can be converted into hollow carbon structures. The templating method uses particles with the intended shape, a reaction occurs where the carbon coats the shaped particles which are then removed through a chemical or physical procedure [53]. Different possible morphologies can be synthesized from these methods such as nanoboxes [54], nanofibers [52], bow-like structures [55], and hollow spheres [56] as shown in (**Figure 2.4**).

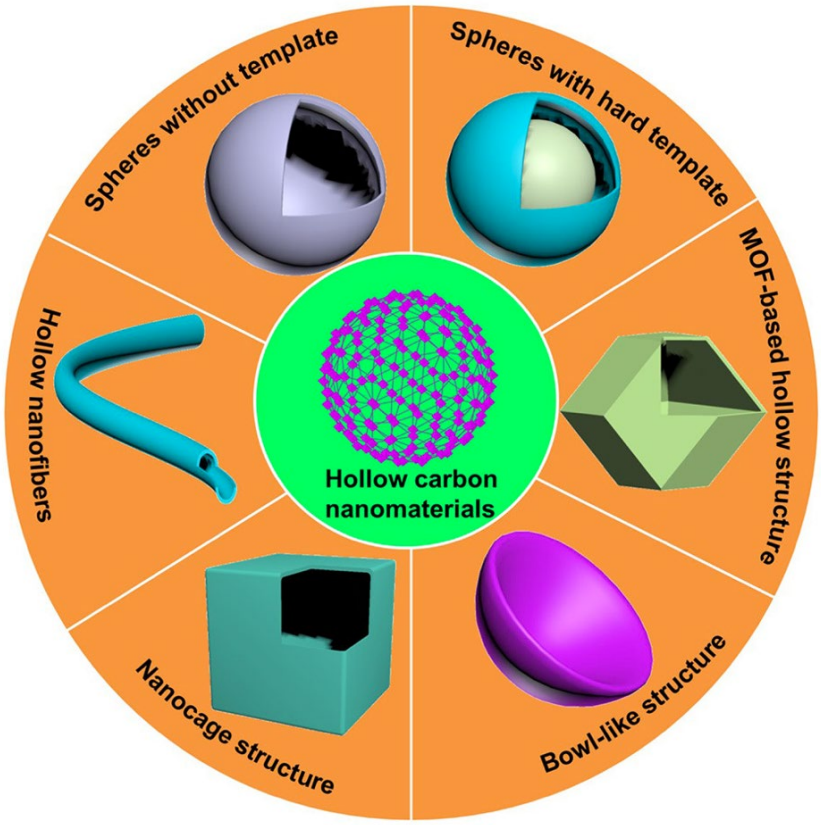


Figure 2.4: Diagram showing different hollow carbon structures [53].

The template-free method can produce materials with morphologies resembling the intended shape however it is difficult to finely tune the hollow morphology. The template method uses the preformed template particles and produces structures that resemble the shapes of the sacrificial templates. This is the most used method of synthesis as it gives control over the end product. Among these hollow carbon structures, hollow carbon spheres (HCSs) have shown promise as electrode material in the electrochemical industry. The shells of hollow carbon spheres can be altered to produce desired characteristics. These alterations, such as doping and creating a porous carbon shell can improve the catalytic abilities of hollow carbon spheres. Enhancing the capabilities of HCSs by doping their carbon layer with heteroatoms such as nitrogen (N) and boron (B) effectively alters their conductivity, reactivity, adsorption, and chemical properties [28], [57]–[60]. These characteristics have made doped HCSs an ideal electrode material to use in areas such as fuel cells, gas sensors, supercapacitors, and solar cells [61]–[63]. Sanetuntikul *et al*. synthesized nitrogen-doped hollow carbon spheres for their efficiency and durability as electrocatalysts. They found that the nitrogen-doped hollow carbon spheres exhibited better electrochemical stability compared to platinum/carbon catalysts [64]. The porous surfaces of the shells and the cavity can be effectively used for electrocatalytic

activity [65], [66]. In the work done by Ariyanto *et al*. they found that porous hollow carbon spheres showed promise as a catalyst for electrochemical applications [67]. Their shape allows for use of different spherical template materials and the synthesis of hollow spheres with multiple layers [56] (**Figure 2.5**).



Figure 2.5: Diagram showing different morphologies of hollow carbon spheres and their possible uses [56].

2.1.3.1 Single-shelled and double-shelled hollow carbon spheres

Hollow carbon spheres (HCSs) have distinctive morphology, low density, large surface area, and high conductivity [44], [59]. This has resulted in the synthesis of single-shelled HCSs for various electrochemical applications [68]. The added advantage of parameter manipulation during synthesis can result in higher surface areas. This would influence the conductivity of the carbon layers and increase the number of active sites as found by Xu *et al.* through the synthesis of double-shelled HCSs [69]. Double-shelled hollow carbon spheres have the same qualities as single-shelled hollow carbon spheres with the added advantages of larger surface area to volume ratios, multi-porosity that gives easy access to the electrolyte in photovoltaic devices, highly conductive, a larger number of active sites, and a large core void [70]–[72].

The review and work done by the group Qi *et al.* found that the use of multi-layered structures as electrode materials, provided additional activity sites and improved catalytic capacity [73].

2.2 Metal sulfides

Metal oxides such as titanium dioxide (TiO_2) have long been an area of research for electrocatalytic reactions due to the presence of oxygen (O) allowing redox reactions to occur [74]. However, another group of nanoparticles has shown electro and photochemical properties that rival metal oxide properties. Composites of metal oxides with metal sulfides have resulted in the enhancement of metal oxide properties [75], [76]. Mittal *et al.* found that although TiO_2 has exceptional qualities such as long-term stability, it has a high bandgap that does not utilize most of the solar energy. On the other hand, binary metal sulfides, ZnS and CdS have the desired bandgaps but are unstable and easily oxidized. From their study, a co-catalyst of these materials (ZnS/CdS-TiO_2) showed an improved efficiency [77] compared to TiO_2 alone. Metal sulfides have narrow bandgaps that allow them to harness more of the sun's radiation. This can be attributed to the high electron affinity and low ionization potential of sulfur compared to oxygen [78], [79].

The inorganic anion (S^{2-}) can react with a majority of transitional metals in the first row to produce different types of binary (CdS, Bi_2S_3), ternary ($ZnIn_2S_4$, Cu_3SnS_4), and quaternary (Cu_2ZnSnS_4) metal sulfides [80]. In a study carried out by Nguyen *et al.*, they found that ternary sulfide $Zn_xCd_{1-x}S$ showed high photostability and the addition of MoS_2 as a co-catalyst enhanced the catalytic performance of the material [81]. Given that the addition of metal sulfides to metal oxides enhances their electrochemical properties and co-catalysts of different metal sulfide combinations result in materials with superior qualities makes metal sulfides an interesting area of research. Their addition to other organic or inorganic materials can enhance their properties. Binary sulfides have simple chemical structures, low-cost production, easy synthesis methods, and favourable qualities. Which include large redox reaction sites and high conductivity making them suitable candidates for electrode materials in energy devices [82]. Ternary and quaternary sulfides also exhibit exceptional electrocatalytic activities and conductivity. However, compared to the monometallic sulfides, the addition of more metals adds to the complexities of composition, synthesis, and chemical structures [80], [83]. Amongst the binary sulfide semiconductors, copper sulfide (Cu_2S) is an exceptional p-type and absorber

material with a narrow bandgap of 1.2 eV that shows great conductivity for application in solar cells [84], [85].

2.2.1 Copper sulfides

Copper sulfides have attractive optical and electrical properties, high carrier mobility, and great electrocatalytic abilities [86]–[88]. Various stoichiometric forms (**Figure 2.6**) of solid-phase $Cu_{2-x}S$ exist, from copper-rich; high-chalcocite (hexagonal $Cu_{2.0-1.94}S$), low-chalcocite (monoclinic $Cu_{2.0-1.997}S$), cubic- chalcocite (Cu_2S), djurleite ($Cu_{1.96}S$), digenite ($Cu_{1.8}S$), anilite ($Cu_{1.75}S$), and copper-poor; covellite (CuS) [89]–[91]. The Cu-S system is a complex structure with a triangular formation of CuS_3 groups and S-S bonds within the CuS_4 tetrahedrons (**Figure 2.7**) [92], [90].

The work done by Evan *et al.* determined that low chalcocite has a monoclinic crystal structure that consists of 24 Cu atoms and 12 S atoms in a distorted hexagonal-close packed framework with fully occupied Wyckoff sites [93]. Its unit cell consists of 144 atoms made up of 96 copper atoms and 48 sulfur atoms. Low and high chalcocite have closely related structures due to their hexagonal lattices; however, their copper atom arrangements are different. Both high and cubic chalcocite do not have fully occupied Wyckoff sites [90]. Djurleite is also monoclinic with a reduced copper concentration. A unit cell that consists of 62 Cu atoms, 52 in a triangular formation, 9 in the tetrahedral formation, and 1 in linear coordination [94]. Depending on the temperature used during synthesis digenite can exist as hexagonal, cubic, or rhombohedral phases. At high temperatures digenite can convert to structures with high symmetry [95]. Anilite has the P*nma* space group therefore it has an orthorhombic Cu-S system, in which the S atoms are in an fcc arrangement with 28 Cu atoms ordered in the interstitial positions. The unit cell is made up of 20 Cu atoms in triangular coordination and 8 are in tetrahedral coordination [96], [97]. The Cu poor CuS (covellite) is made up of a simple Cu-S system, with CuS_3 and CuS_4 groups [92].

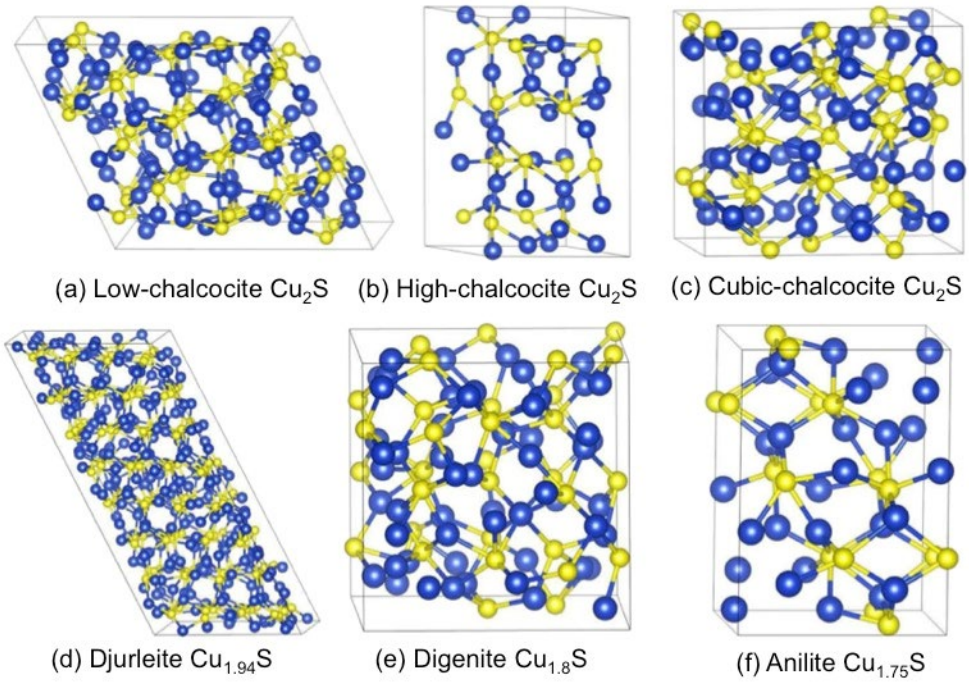


Figure 2.6: Crystal structures of (a) the low-chalcocite), (b) high chalcocite (hexagonal), (c) cubic-chalcocite (cubic), (d) djurleite, (e) digenite, and (f) anilite. Blue and yellow represent copper and sulfur atoms respectively [97].

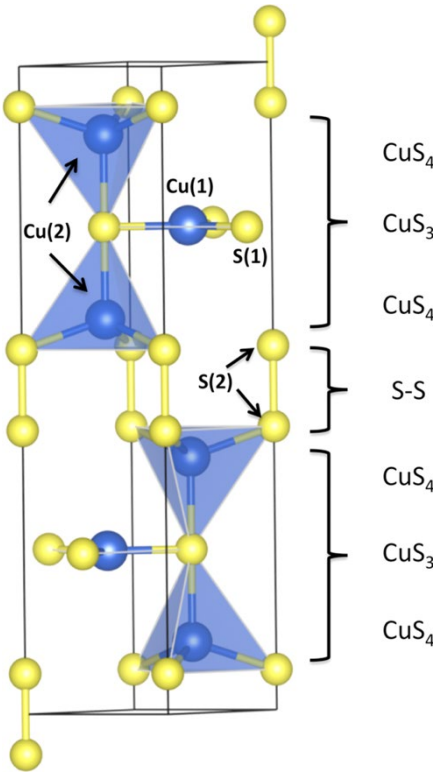


Figure 2.7: Hexagonal unit cell showing the Cu-S system of triangular and tetrahedron coordination for copper (blue) and sulfur (yellow) [92].

2.2.2 Quantum effects

The bandgaps of these different copper (Cu) and sulfur (S) compositions vary depending on the copper deficiency of the material. Free-holes due to Cu-vacancies results in larger bandgaps due to unfilled orbitals [89]. Therefore more energy is needed to excite an electron from the valance band (VB) to the conduction band (CB) this is called the Moss-Burstein effect [98]. Band energy (E_g) is not only affected by the Cu concentration, but also by the size and shape of the copper sulfide particles. A change in the sizes of the nanostructured semiconductors alters their chemical and physical properties due to the quantum confinement effect [99], [100]. To determine the size effect on quantum confinement, the absorption spectra can be used. In work done by Luther *et al.*, they found that there was a blue shift to higher energy in the UV-Vis absorption spectra when the $Cu_{2-x}S$ particles decreased in size [101]. Many studies [98], [102], [103] found that $Cu_{2-x}S$ nanoparticles with sizes of less than 10 nm showed a blue-shifted bandgap absorption compared to bulk materials of $Cu_{2-x}S$ with larger sizes (**Figure 2.8**). Therefore, more energy is required to create an electron-hole pair. Roy et al found that size dependency prevails over the Moss-Burstein effect [104].

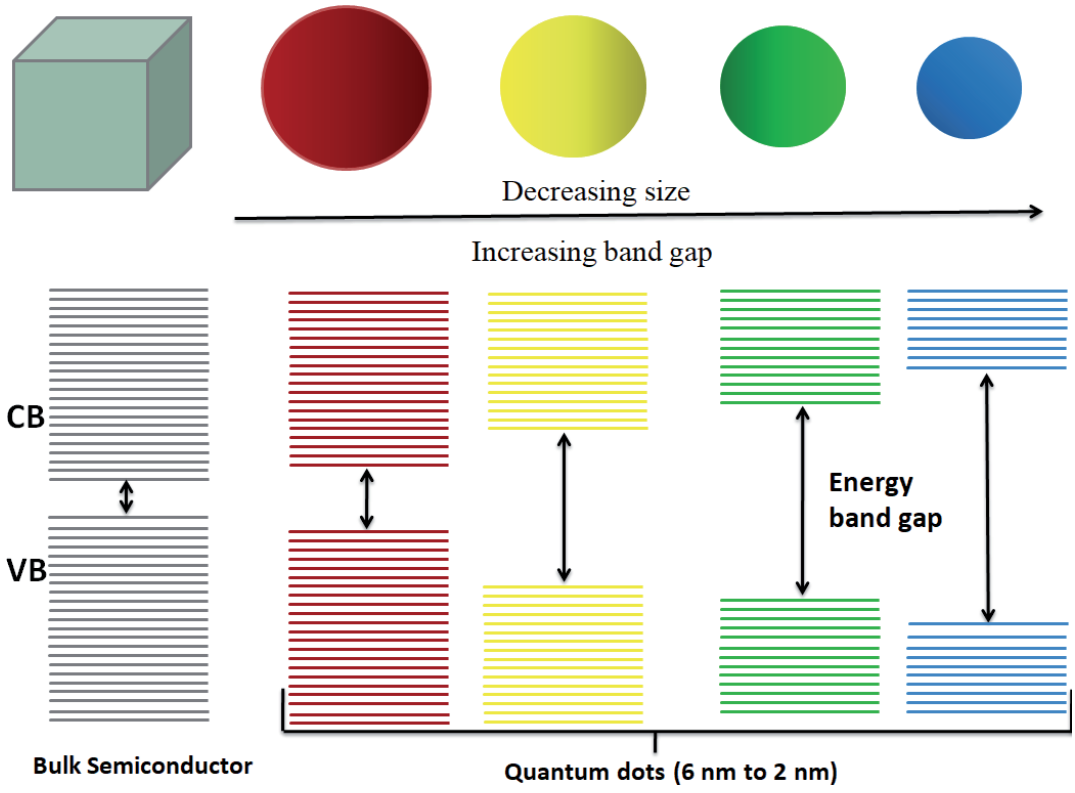


Figure 2.8: Descriptive diagram showing the relationship between bandgap energy and size of particles [100].

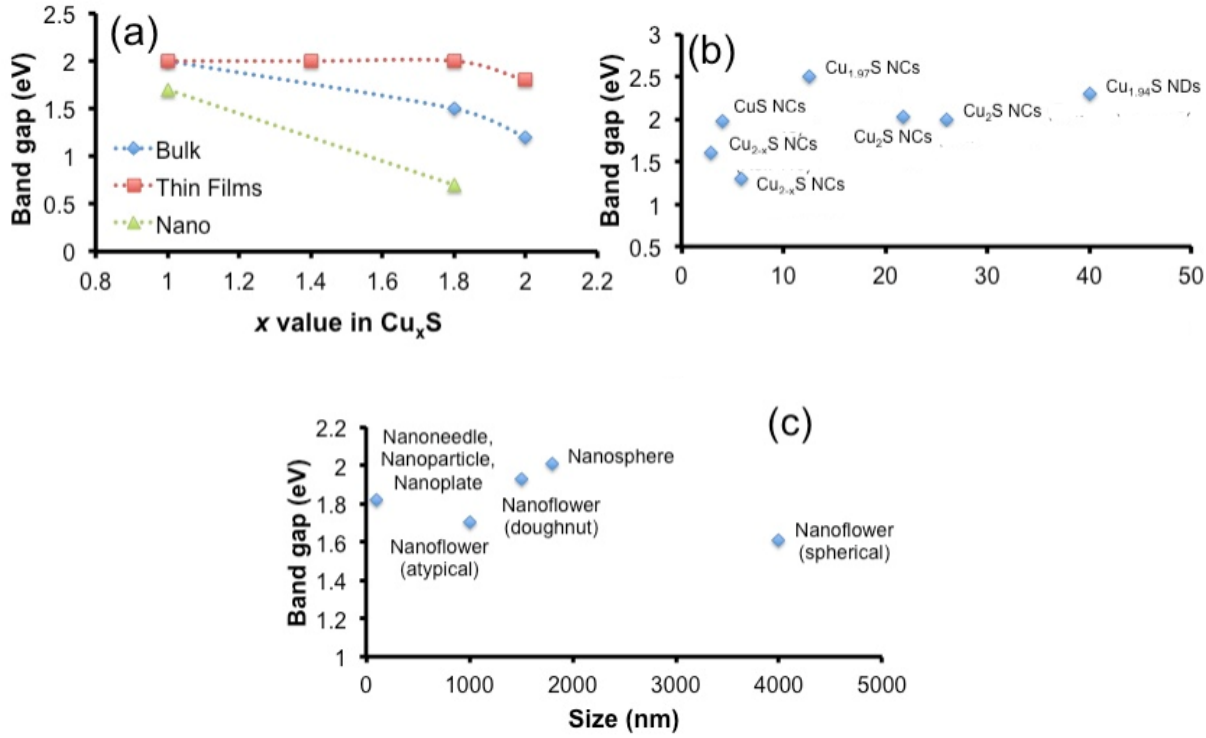


Figure 2.9: Graphs (a-c) show bandgap dependence of copper sulfides with composition, size, and shape of nanostructures [104].

2.2.3 Colloidal synthesis

To produce high-quality semiconducting Cu chalcogenide nanoparticles with distinct shapes and sizes, colloidal synthesis is used [105]. This synthesis method allows for control over the crystal phase, size, and shape of the particles by altering the precursors used, reaction time, reaction temperature, and capping agents. Other advantages of using colloidal synthesis are the monodispersity of synthesized particles and their high crystallinity [89]. Either the heat up or the hot injection route can be used in colloidal synthesis. The heat-up route allows for an increase in yield. The hot-injection route allows for more control on the shape and sizes of the nanoparticles [106] as the nucleation and growth stages are dependent on the injection time. General steps of synthesis involve nucleation from a homogeneous solution, growth of the nuclei, isolation of synthesized particles, and then post-synthesis treatment to remove unreacted precursors [107].

The nucleation process can occur through the heterogeneous or homogeneous route [108], [109]. In a precursor saturated solution, homogeneous nucleation will occur spontaneously and produce uniform nuclei. Heterogeneous nucleation occurs at a pre-existing solid phase nucleation site that is in contact with precursors in their liquid or vapour phases. Although

homogeneous nucleation occurs spontaneously a supercritical state of precursor saturation is required for the reaction to start. The Gibbs free energy for the systems nuclei formation is represented by ΔG in equation (2.1). Where $|\Delta G_V|$ is the difference of Gibbs free energy per unit volume, r is the radius, and the surface energy per unit area is expressed as γ. The negative term of the equation expresses a decrease in Gibbs free energy therefore a favourable bonding will occur between a monomer and a cluster. An increase in the Gibbs free surface energy is expressed by the positive term. This is due to the unfavourable bonding of a monomer. The ΔG due to the bonding between a monomer and cluster corresponds to the contest between a decrease in volume energy and an increase in surface energy. The curve of Gibbs free energy for a cluster is shown in **Figure 2.10**, with r_c representing the critical radius (equation 2.2) that corresponds to the activation energy barrier, ΔG_c.

$$\Delta G = -\frac{4}{3}\pi r^3 |\Delta G_V| + 4\pi^2\gamma \qquad \textbf{(2.1)}$$

$$r_c = \frac{2\gamma}{|\Delta G_V|} \qquad \textbf{(2.2)}$$

Growth is unfavourable for clusters that are smaller than the maximum radius (r_c), due to the positive surface energy increase being larger than the volume energy therefore the system pushes for dissolution. When the clusters are larger than r_c, there is a higher negative volume energy decrease therefore growth is favourable [110], [111].

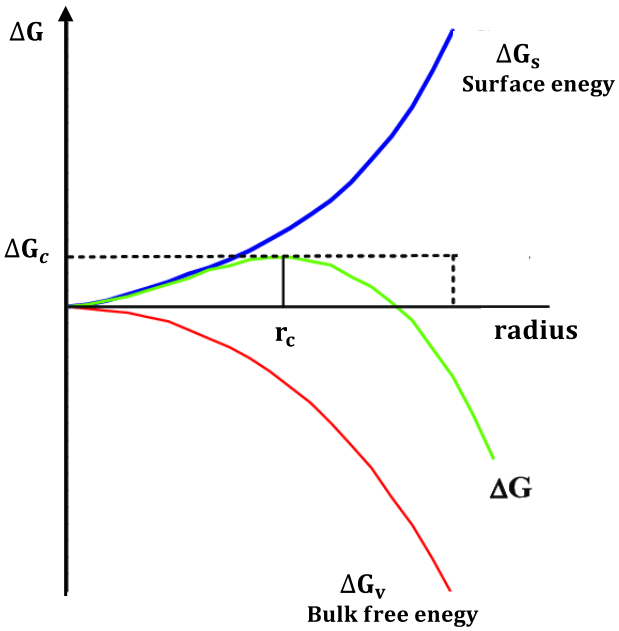


Figure 2.10: Graph shows the change in Gibbs free energy for clusters depending on their radius r_c.

2.2.3.1 LaMer Theory

In the 50s Victor LaMer developed the nucleation-growth theory, his burst nucleation concept depends on the separation of nucleation and nanoparticle growth [112], [113]. For homogeneous nucleation, nuclei are produced at the same time and growth occurs without additional nucleation. The burst nucleation mechanism is exhibited in **Figure 2.11,** and it illustrates the change of monomer concentration as the reaction time increases. In section I, precursors are converted into monomers due to the critical temperature of the reaction being reached. This causes an increase in the monomer concentration until supersaturation is reached (C_s). Section II shows a burst in nucleation, the concentration of monomers has continued to increase from section I until the minimum concentration for nucleation (C_{min}) was reached. At C_{min} level, the activation energy needed for nucleation is surpassed therefore rapid self-nucleation occurs. This causes the monomer concentration to decline therefore ending the nucleation process. For section III nucleation has stopped, the supersaturation level continues to decrease as the remaining monomers bond to existing nuclei resulting in nanoparticle growth.

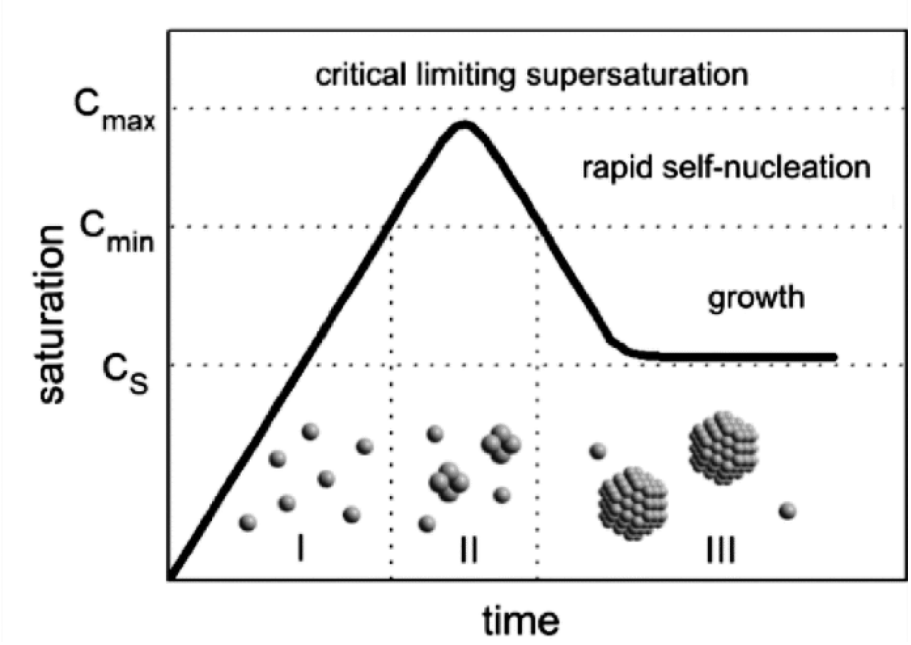


Figure 2.11: Diagram showing LaMer plot for the generation of nuclei, nucleation, supersaturation and the successive growth of colloidal systems [110].

2.2.3.2 Nanoparticle growth

Nanoparticle growth can occur through different mechanisms and is dependent on two parameters, surface reactions and the diffusion of monomers to the surface [114]. For the Ostwald ripening growth mechanism [115], the size of the nanoparticles determines their solubility. The surface energy of the smaller particles and their high solubility in solution allows them to redissolve and attach to large particles which then increase in size. This is seen in work done by Sugimoto *et al.* [116]. The inverse occurs in work done by Lee *et al.* [117] where particle growth occurs through digestive ripening, this involves large particles breaking down into smaller particles. The Finke-Watzky two-step mechanism [118] involves the nucleation and growth processes occurring simultaneously. The initial step involves slow continuous nucleation ($A \rightarrow B$) and the second step is the autocatalytic growth of particles from the precursors ($A + B \rightarrow 2B$), therefore is not diffusion-controlled [119]. Intraparticle growth occurs under distinct conditions where the energy of the nanoparticle's crystal facets is higher than the energy for monomers in the solution.

Therefore, the energy for the bulk solution resembles the particle's surface energy which determines the particles growth. If the facets of the particles have high surface energy they will break down and if the energy is low, they grow and intraparticle diffusion will occur. Peng *et al.* [120], [121] describe intraparticle growth as the overtime alteration of the nanoparticle shape due to the diffusion of monomers on the surface of the particles. Other growth mechanisms are coalescence where there is random orientation of the lattice plane and no attachment preference [122]. For orientated attachment, a crystallographic alignment exists for attachment to occur [123], as seen in the work done by Li *et al.* [124] who found that the particles rotated until the crystallographic orientation matched.

2.3 Dye-sensitized solar cells (DSSCs)

As one of the most promising third-generation solar technologies, dye-sensitized solar cells (DSSCs) have been an area of intensive research since they were introduced by O'Regan and Grätzel in 1991 [125], [126]. This increasing interest is because these technologies are easy to assemble and have low fabrication costs due to the thin-film technology being used. DSSCs are made up of 5 different components [127]. These are, the counter electrode (CE) that is capable of regenerating the redox mediator, an electrolyte containing a redox couple which is typically I^- / I_3^-. Mechanical support that is coated with transparent conductive oxides (TCO)

(i.e. tin indium oxide - ITO), a semiconducting film (TiO_2), and lastly a sensitizer absorbed onto the surface of the semiconductor (e.g. dye) [128], [129].

The schematic diagram of a DSSC, **Figure 2.12** shows that with sunlight exposure the sensitized dye in the DSSC is excited by the photons. The released electrons move from the valance band to the conduction band of the mesoporous oxide film and create an electron-hole pair.[130] The dye then promotes the diffusion of electrons towards the anode and the electrons move through the external circuit to the counter electrode. The electrolyte containing the I^- / I_3^- redox ions is used as an electron mediator between the photoelectrode and the counter electrode. The oxidized dye molecules are regenerated by receiving electrons from the I^- ion redox mediator that gets oxidized to I_3^- to complete the dye cycle [125], [131], [132].

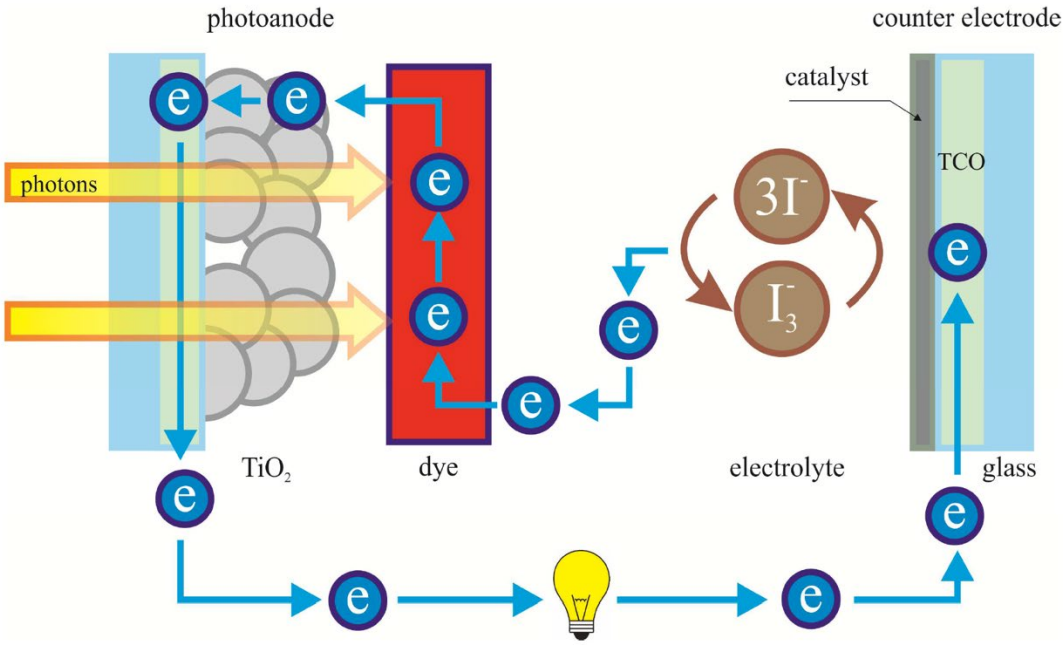


Figure 2.12: Schematic diagram of a dye-sensitized solar cell [127].

2.3.1 Counter electrode (CE)

The counter electrode (CE) is one of the crucial components of a DSSC as it plays an important role in the efficiency of the device. It also collects electrons from the external circuit and catalyzes the redox reaction in the electrolyte thus influencing the photovoltaic performance and long-life stability of the device [133]. Currently, platinum-coated fluorine-doped tin oxide (FTO) is used as a CE material for DSSCs, due to its high conductivity, and high catalytic

activity [134]. However, it comes with several disadvantages such as high cost since platinum is a noble metal, undersupply, and low stability in the electrolyte [135] this limits large-scale production.

2.3.2 Electrochemical analysis of the counter electrodes

2.3.2.1 Cyclic voltammetry (CV)

Cyclic voltammetry (CV) [136] is an electroanalytical technique that is used to obtain qualitative and quantitative data for an electroactive material. A linear potential sweep is applied to the working electrode at a steady scan rate from the high potentials to the low potentials and then in the reverse direction. Since CV is an amperometric technique, the current produced at the surface of the electrode is measured at each applied potential. To measure the electrocatalytic activity of a CE material two negatively correlated components are important in CV, the peak current density (I_p). and the peak-to-peak separation (E_{pp}). Given that the performance of the DSSC is dependent on the reduction reaction. The reductive (cathodic) peak shows this reduction of I_3^- to I^- [137]. For each CE material, the I_p and E_{pp} data obtained from the reductive peak will determine if the material can potentially replace the Pt-CE. A high reductive peak current density and low peak-to-peak separation suggest that the CE material has good electrocatalytic activity as electrons participate in the electrolyte redox reaction. The surface area, morphology, and composition of the CE materials affect the I_p and E_{pp}parameters. To determine the stability of the CE material several cycles of the CV analysis are conducted. Changes in the characteristics of the CV curves are then used to assess the stability of the various CE materials.

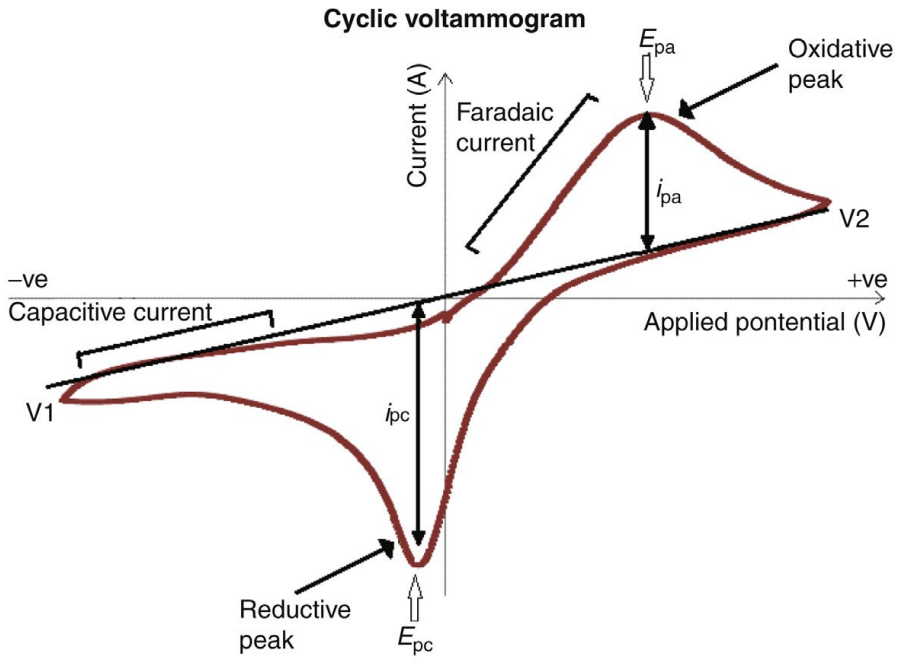


Figure 2.13: Diagram illustrating a cyclic voltammetry plot showing the cathodic potential (E_{pc}) and current (I_{pc}) [136].

2.3.2.2 Electrochemical Impedance Spectroscopy (EIS)

Impedance spectroscopy of an electrochemical cell can produce relevant information that is used to determine the capacitance and resistance occurring between the electrolyte and the counter electrode [138]. A Nyquist plot is obtained from the EIS measurement and consists of imaginary part impedance values on the *y*-axis and real part on the *x*-axis. The real part impedance values relate to the resistances whilst the imaginary part relates to the capacitance. The electrochemical cell typically used for EIS measurements enables accurate evaluation of the impedance occurring at the electrolyte and counter electrode interface. For purpose of analysis, an equivalent circuit of the Nyquist plot (**Figure 2.14**) is used to provide information on the resistances occurring in a dye-sensitized solar cell. The high-frequency intercept on the real impedance axis corresponds to the ohmic resistance (R_s).

This gives the series resistance of the conductive fluorine-doped tin oxide (FTO) substrate, the adhered counter electrode material on the conductive substrate, and the counter-resistance. The charge transfer resistance (R_{ct}). is given by the radius of the semicircle which corresponds to the constant phase angle (CPE) found at the counter electrode/electrolyte interface for the

reduction reaction of I_3^- ions. The fast charge transfer rate suggests that there is good electrocatalytic activity at the counter electrode and this is represented by a low R_{ct}.

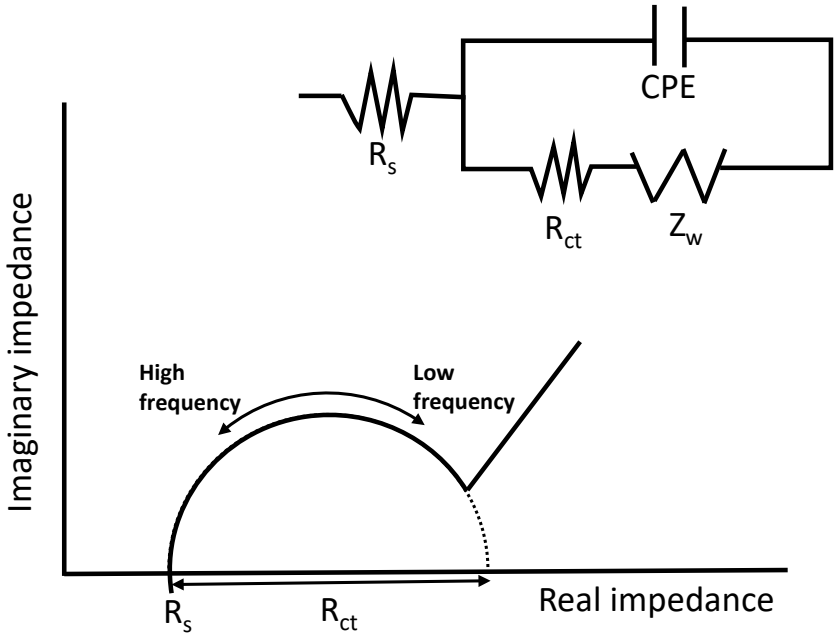


Figure 2.14: An example of a Nyquist plot with an inset of the equivalent circuit for fitting the electrochemical impedance spectroscopy (EIS) data.

2.3.2.3 Tafel polarization

To analyze the electrochemical reaction of electrolyte reduction from I_3^- to I^- by the counter electrode material, Tafel polarization can be used. The Tafel plot shows the logarithmic current density ($\log J$) as a function of the applied potential (V) as shown in **Figure 2.15**. A Tafel curve can be split into three parts, with the lower region representing the polarization zone. The middle region of the curve is the Tafel zone, this corresponds to the electrocatalytic activity of a counter electrode [139], [140]. The high potential region is the third part of the curve which represents the diffusion zone. This relates to the diffusion of the electrolyte ions at the electrode surface. Other information that can be obtained from the polarization curves is the exchange current density (J_0) and the limiting diffusion current density (J_{lim}). These parameters relate to the electrocatalytic activity of the counter electrode. From equation 2.3, the exchange current density (J_0) is inversely proportional to the charge transfer resistance (R_{ct}):

$$J_o = \frac{RT}{nFR_{ct}} \qquad (\mathbf{2.3})$$

where T is the temperature (298 K), R is the gas constant, n is the number of electrons, and F is the Faraday's constant [141]. Therefore, for an increase in electrocatalytic activity of the counter electrode, a high J_0 value and low R_{ct} is exhibited. The electrocatalytic activity, ion adsorption, and diffusion ions have an effect on the limiting diffusion current density. J_{lim} corresponds to the maximum number of ions that can diffuse onto the CE. This is shown in equation 2.4 as the diffusion coefficient (D) of the electrolyte is directly proportional to J_{lim} [141].

$$D = \frac{L}{2nFC} J_{\text{lim}} \qquad \textbf{(2.4)}$$

In the equation above, the spacer thickness is represented by L, F is the Faraday's constant, and n is the number of electrons involved in the reaction. Therefore, for an increase in electrocatalytic activity of the CE, a high J_0 value and low R_{ct} is exhibited. It follows that a high J_{lim} suggests that the electrocatalytic performance of the CE has increased.

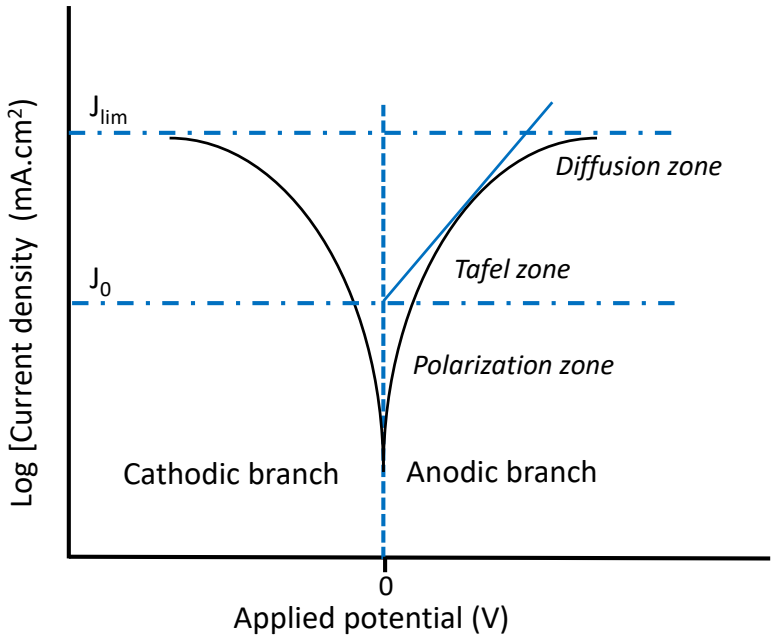


Figure 2.15: Diagram illustrating a Tafel polarization plot of a DSSC.

2.3.2.4 Current-voltage (I-V) measurements

The current density-voltage measurement is carried out on a fabricated DSSC device consisting of the photoanode and counter electrode connected to a potentiostat [142]. The generated current is measured against the applied potential from the potentiostat as shown in the $I-V$ plot (**Figure 2.16**). Four crucial parameters can be obtained from the $I-V$ graph, the open-

circuit voltage (V_{oc}), short-circuit current density (J_{sc}), fill factor (FF), and the power conversion efficiency (PCE) [143]. J_{sc} is the photocurrent density flowing through the external circuit when the applied potential is zero. This short-circuit current arises from light illumination on the solar cell with no external voltage. Factors such as the charge transmission efficiency at the photoanode, adsorption of the active layer, and electrolyte composition determine the J_{sc}. Open-circuit voltage (V_{oc}) is represented by the voltage between the terminals when the photocurrent is zero. The V_{oc} value is dependent on the difference between the Nernst potential (E_o) and the Fermi level (E_F) [144]. PCE is defined as the ratio of the output power to the input power therefore, it is the overall incident light (P_{in}) to electric power conversion efficiency ($P_{max,out}$) [140]. This is represented by equation 2.5:

$$PCE = \frac{P_{max,out}}{P_{in}} \text{ x } 100\ \% = \frac{\max(I\ x\ V)}{P_{in}} \text{x } 100\ \% \qquad \textbf{(2.5)}$$

The fill factor index represents the overall quality of the solar cell. This can be defined by the maximum power output from V_{oc} and J_{sc} as shown by equation 2.6. An ideal DSSC has no charge loss, sensitizer corrosion, or electron-hole recombination and would, therefore, exhibit a rectangular $I - V$ curve with a FF value of one.

$$FF = \frac{PCE}{J_{sc} \text{ x } V_{oc}} \text{ x } 100\ \% \qquad \textbf{(2.6)}$$

Factors such as the charge transfer resistance (R_{ct}), the Warburg impedance (Z_w), and the shunt resistance (R_{sh}) affect the FF value. Small charge transport (R_{ct}) in a solar cell corresponds to the reduced loss of open-circuit voltage (V_{oc}). The shunt resistance represents the efficiency of the electron-hole separation and a large R_{sh} corresponds to the reduced loss of short-circuit current density (J_{sc}) [145]. It follows that a small R_{ct} together with a large R_{sh} result in an increased FF value and better PCE.

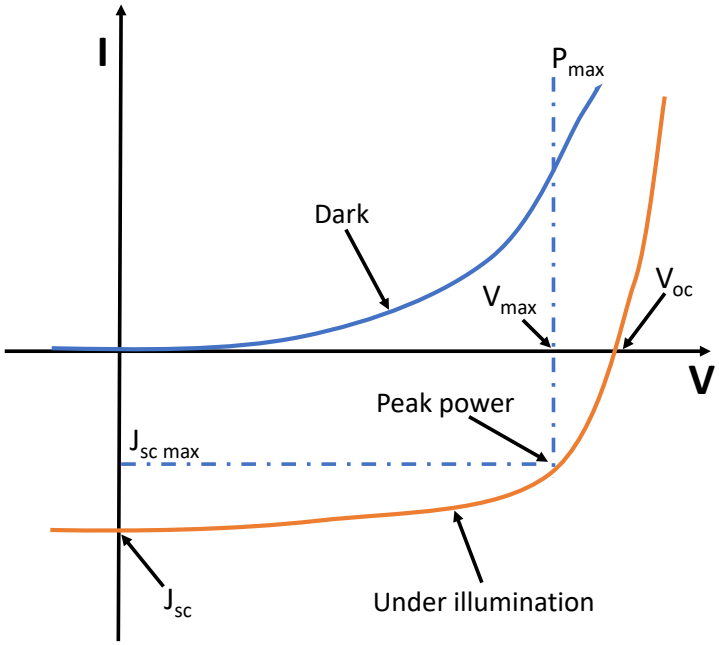


Figure 2.16: Plot of the current-voltage (I-V) curves of a solar cell in the dark and under illumination.

2.4 Carbon composites for use as counter electrodes in DSSCs

The performance of DSSCs is dependent on the semiconductor material used. Carbon structures have attracted several researchers for the use of counter electrodes in DSSC. This is due to their high conductivity and low-cost synthesis. Hollow structured carbon materials have been reported to have great photovoltaic properties. For example, Wu *et al*. conducted a study on solid carbon spheres (SCS), hollow carbon spheres (HCS), and open-end carbon spheres (OCS) in the iodide electrolyte [146]. They found that the OCS (8.7%), and HCS (8.1%) exhibited a higher power conversion efficiency (PCE) compared to SCS (7.8%), and their reference Pt (8.0%). Even after a 40-day stability test OCS and HCS retained high PCE's of 88.7 and 89.2%. The high conversion rates were attributed to the voids in the hollow structures which resulted in higher surface area and therefore, increase the active sites. This increase has also been reported with other hollow structures such as carbon nanotubes. An increase in efficiencies of these carbon materials can be achieved through heteroatom doping and/ synthesizing porous carbon materials. From the photovoltaic parameters listed in (**Table 2.1**), it can be noted that the mesoporous carbon exhibited a PCE that is almost three times that of macroporous carbon. This suggests that the mesoporous nature of the material assists with electrolyte reduction in DSSC.

Fang *et al.* found that hollow-core mesoporous shell carbon (HCMSC) had higher J_{sc} (15.85 mA/cm^2), V_{oc} (0.74 V), FF (0.67) and PCE (7.56%) [147]. This was in comparison to its carbon counterparts activated carbon (J_{sc} -15.00 mA/cm^2, V_{oc} -0.73 V, FF - 0.54 and PCE 6.24%)and ordered mesoporous carbon (J_{sc} -15.65 mA/cm^2, V_{oc} -0.73 V, FF - 0.61 and PCE 7.03%). These results suggest that a mesoporous shell on hollow carbon structures enhances the electrocatalytic activity of the material. This is due to the high surface area and accessible porosity of the carbon material [148]. The doping of porous carbon with nitrogen increases the conversion efficiency of the material. This was exhibited in the work done by Wang *et al.* they found that nitrogen-doped porous carbon had a V_{oc} of 0.707 V, J_{sc} of 15.19 mA cm^{-2}, FF of 0.66, and a PCE of 7.09% [149]. This electrocatalytic parameters where higher than those of undoped porous carbon (V_{oc} -0.667 V, J_{sc} -14.37 mA/cm^2, FF - 0.64 and PCE 6.13%). This enhanced photovoltaic performance is owed to not only the mesoporous nature and the high surface area but also the presence of nitrogen in the porous layers.

Single structured carbon materials have shown favourable electrocatalytic performances parameters, as seen in the table below. However, hybrid materials seem to exhibit better performances this could be ascribed to their multi-functionality behaviours. From the reviews conducted by Chen *et al*. and Samantaray *et al.* [150], [151]. They concluded that carbon structures including doped and mesoporous structures have high catalytic abilities for redox reactions. However, the application of hybrid carbon materials has great potential for DSSC. From the Meyer *et al.* review, carbon materials and their composites with metal sulfides exhibit slightly lower efficiencies as counter electrodes, compared to Pt [152]. Therefore more work needs to be conducted to produce better carbon-metal sulfide counter electrodes. To achieve this, their morphology can be manipulated to produce materials with high catalytic areas that facilitate high electron transfer at the CE interface. From the table below it can be concluded that hybrids of metal sulfides with carbon materials increased the efficiencies of the metal sulfides.

Table 2.1: Electrocatalytic parameters and photovoltaic performance of various carbon CE materials.

CE material	R_{ct} (ohm)	J_{sc} (mA/cm^2)	V_{co} (V)	FF %	PCE %	Ref
Microporous carbon	1.32	14.80	0.798	62	7.36	[153]
Ordered mesoporous carbon	6.50	13.56	0.797	69	7.46	[154]
Ordered macroporous carbon	4.70	14.10	0.772	52	2.91	[155]
Hollow ACN	6.80	14.50	0.730	62	6.58	[156]
N-HCS	6.17	14.03	0.719	61	6.14	[157]
Co-N- HCS	6.08	15.11	0.728	70	7.71	[157]
CuS	2.90	8.72	0.589	45	2.30	[158]
rGO:CuS	1.48	10.62	0.545	45	2.62	[158]
Cu_2S	5.05	16.20	0.560	41	3.77	[159]
rGO:Cu_2S	4.70	17.20	0.560	44	4.26	[159]
CZTS-MWCNT	4.19	16.62	0.760	72	9.04	[160]
$CoNi_2S_4$/rGO	12.20	21.96	0.880	85	10.21	[161]

Since carbon materials have shown potential as substitutes for platinum as the counter electrode, this is because carbon is environmentally friendly, cheap, abundant, stable, has good resistance towards iodide, and have high reactivity to triiodide reduction. The drawbacks of carbon in DSSCs are slow diffusion of the electrolyte through micropores therefore to combat this, mesoporous hollow carbon spheres were synthesized in this work. In most of the research that has been carried out on the use of carbon as a counter electrode, it was established that the composites of carbon with other carbon materials [162] or different materials such as titania [163] and polyaniline[164]. The composites were found to have enhanced charge transfer from the counter electrode to the electrolyte, high electrical conductivity, and good catalytic activity [165]. Copper sulfides have high conductivity, good electronic properties, and high oxidation resistance. However, Cu_2S is unstable, has Cu vacancy formation as the redox reactions occur. This leads to an increased bandgap and the material behaving as a degenerate semiconductor [166].

A composite between the two materials discussed could stabilize copper sulfide and enhance carbon properties. Single-shelled and double-shelled hollow carbon synthesis for this work was influenced by Mutuma *et al.* [44] and Zhang *et al.* [167] respectively. And the colloidal synthesis was influenced by Wang *et al.* [107]. Copper sulfide and single-shelled hollow carbon spheres have been individually researched for their possible use as CE materials in DSSC. However double-shelled hollow carbon spheres, their composite with Cu_2S, and the composite of single-shelled hollow carbon spheres with Cu_2S have not been explored as CE materials in DSSCs. This works aims to synthesize these materials and prepare composite materials with carbon and copper sulfide. Their electrocatalytic activity will then be investigated to determine if they exhibit better catalytic properties compared to Pt.

References

[1] S. Begum, A. N. Karim, M. N. Ansari, and M. S. Hashmi, "Nanomaterials. Reference Module in Materials Science and Materials Engineering," *Elsevier Inc.*, pp. 1–25, 2019.

[2] R. M. Ian A. S. Edwards, Harry Marsh, *Introduction to Carbon Science*. 1989.

[3] R. Vajtai, *Springer handbook of nanomaterials*. 2013.

[4] O. Mykhailiv, H. Zubyk, and M. E. Plonska-Brzezinska, "Carbon nano-onions: Unique carbon nanostructures with fascinating properties and their potential applications," *Inorganica Chim. Acta*, vol. 468, pp. 49–66, 2017.

[5] L. Dai, D. W. Chang, J. B. Baek, and W. Lu, "Carbon nanomaterials for advanced energy conversion and storage," *Small*, vol. 8, no. 8, pp. 1130–1166, 2012.

[6] H. Marsh and F. Rodríguez-Reinoso, "CHAPTER 9 - Production and Reference Material," H. Marsh and F. B. T.-A. C. Rodríguez-Reinoso, Eds. Oxford: Elsevier Science Ltd, 2006, pp. 454–508.

[7] D. D. L. Chung, "7 - Carbon-Matrix Composites," D. D. L. B. T.-C. C. (Second E. Chung, Ed. Butterworth-Heinemann, 2017, pp. 387–466.

[8] J. Ni and Y. Li, "Carbon Nanomaterials in Different Dimensions for Electrochemical Energy Storage," *Adv. Energy Mater.*, vol. 6, no. 17, pp. 1–21, 2016.

[9] F. M. Machado and S. B. Fagan, "Chapter 2 Carbon Nanoadsorbents," no. April, 2015.

[10] J. Zhang *et al.*, "Carbon science in 2016: Status, challenges and perspectives," *Carbon N. Y.*, vol. 98, no. May 2018, pp. 708–732, 2016.

[11] E. Pop, D. Mann, Q. Wang, K. Goodson, and H. Dai, "Thermal conductance of an

individual single-wall carbon nanotube above room temperature," *Nano Lett.*, vol. 6, no. 1, pp. 96–100, 2006.

[12] J. P. Salvetat *et al.*, "Elastic and shear moduli of single-walled carbon nanotube ropes," *Phys. Rev. Lett.*, vol. 82, no. 5, pp. 944–947, 1999.

[13] T. C. Dinadayalane and J. Leszczynski, "Remarkable diversity of carbon-carbon bonds: Structures and properties of fullerenes, carbon nanotubes, and graphene," *Struct. Chem.*, vol. 21, no. 6, pp. 1155–1169, 2010.

[14] N. Arora and N. N. Sharma, "Arc discharge synthesis of carbon nanotubes: Comprehensive review," *Diam. Relat. Mater.*, vol. 50, pp. 135–150, 2014.

[15] S. Iijima, "Helical microtubules of graphitic carbon," *Nature*, vol. 354, no. 6348, pp. 56–58, 1991.

[16] C.-C. Moise and M. Enachescu, "High-Quality Carbon Nanomaterials Synthesized by Excimer Laser Ablation," *Appl. Laser Ablation - Thin Film Depos. Nanomater. Synth. Surf. Modif.*, vol. 1985, 2016.

[17] A. N. Kapitonov, M. N. Egorova, A. E. Tomskaya, S. A. Smagulova, and A. A. Alekseev, "Hydrothermal synthesis of carbon dots and their luminescence," *AIP Conf. Proc.*, vol. 2041, no. May 2020, 2018.

[18] E. Sulistya *et al.*, "Hydrothermal synthesis of carbon microspheres from sucrose with citric acid as a catalyst: physicochemical and structural properties," *J. Taibah Univ. Sci.*, vol. 14, no. 1, pp. 1042–1050, 2020.

[19] F. Gao, Y. H. Zang, Y. Wang, C. Q. Guan, J. Y. Qu, and M. B. Wu, "A review of the synthesis of carbon materials for energy storage from biomass and coal/heavy oil waste," *Xinxing Tan Cailiao/New Carbon Materials*, vol. 36, no. 1. pp. 34–48, 2021.

[20] P. Bhagabati *et al.*, *Synthesis/Preparation of Carbon Materials*. 2019.

[21] M. S. A. Bhuyan, M. N. Uddin, M. M. Islam, F. A. Bipasha, and S. S. Hossain, "Synthesis of graphene," *Int. Nano Lett.*, vol. 6, no. 2, pp. 65–83, 2016.

[22] M. Yi and Z. Shen, "A review on mechanical exfoliation for the scalable production of graphene," *J. Mater. Chem. A*, vol. 3, no. 22, pp. 11700–11715, 2015.

[23] M. Cai, D. Thorpe, D. H. Adamson, and H. C. Schniepp, "Methods of graphite exfoliation," *J. Mater. Chem.*, vol. 22, no. 48, pp. 24992–25002, 2012.

[24] Y. Zhang, L. Zhang, and C. Zhou, "Review of Chemical Vapor Deposition of Graphene and Related Applications," *Acc. Chem. Res.*, vol. 46, no. 10, pp. 2329–2339, Oct. 2013.

[25] X.-D. Wang, K. Vinodgopal, and G.-P. Dai, "Synthesis of Carbon Nanotubes by

Catalytic Chemical Vapor Deposition," *Perspect. Carbon Nanotub.*, pp. 1–19, 2019.

[26] C. Zhang *et al.*, "The efficient synthesis of carbon nano-onions using chemical vapor deposition on an unsupported Ni–Fe alloy catalyst," *Carbon N. Y.*, vol. 49, no. 4, pp. 1151–1158, 2011.

[27] R. Panickar, C. B. Sobhan, and S. Chakravorti, "Chemical vapor deposition synthesis of carbon spheres: Effects of temperature and hydrogen," *Vacuum*, vol. 172, p. 109108, 2020.

[28] Z. N. Tetana, S. D. Mhlanga, and N. J. Coville, "Chemical vapour deposition syntheses and characterization of boron-doped hollow carbon spheres," *Diam. Relat. Mater.*, vol. 74, pp. 70–80, 2017.

[29] E. R. Phago, "Synthesis of Catalyst Nanoparticles Encapsulated in Mesoporous Carbon Spheres and their Subsequent use as Catalysts for the Oxygen Reduction Reaction," 2016.

[30] A. Behera, P. Mallick, and S. S. Mohapatra, "Chapter 13 - Nanocoatings for anticorrosion: An introduction," in *Micro and Nano Technologies*, S. Rajendran, T. A. N. H. Nguyen, S. Kakooei, M. Yeganeh, and Y. B. T.-C. P. at the N. Li, Eds. Elsevier, 2020, pp. 227–243.

[31] A. De Lodyguine, "Illuminesenz for incandescent lamps," 1897.

[32] A. E. van Arkel and J. H. de Boer, "Representation of pure titanium, zirconium, hafnium and thorium metal," *Zeitschrift für Anorg. und Allg. Chemie*, vol. 148, no. 1, pp. 345–350, 1925.

[33] W. A. Bryant, "The fundamentals of chemical vapour deposition," *J. Mater. Sci.*, vol. 12, no. 7, pp. 1285–1306, 1977.

[34] J. R. Creighton and P. Ho, "Chapter 1 Introduction to Chemical Vapor Deposition (CVD)," *Chem. Vap. Depos.*, no. Cvd, pp. 1–13, 2001.

[35] M. L. Green and R. A. Levy, "Chemical Vapor Deposition of Metals for Integrated Circuit Applications," *Jom*, vol. 37, no. 6, pp. 63–71, 1985.

[36] R. D. Gretz, C. M. Jackson, and J. P. Hirth, "Nucleation in surface catalyzed chemical vapor deposition (CVD)," *Surf. Sci.*, vol. 6, no. 2, pp. 171–192, 1967.

[37] J. Brice, "Condensation and evaporation," *Solid. State. Electron.*, vol. 7, p. 489, 1964.

[38] C. F. Powell, J. H. Oxley, J. M. Blocher, and J. Klerer, "Vapor Deposition," *J. Electrochem. Soc.*, vol. 113, no. 10, p. 266C, 1966.

[39] G. Saeed and M. U. Farooq, "Investigating the effects of CVD reaction time on the growth of carbon nanotubes," *Optoelectron. Adv. Mater. Rapid Commun.*, vol. 7, no.

9–10, pp. 707–711, 2013.

[40] M. A. Chowdhury and D. M. Nuruzzaman, “Influence of gas flow rate on the deposition rate on stainless steel 202 substrates,” *Tribol. Ind.*, vol. 34, no. 4, pp. 226–231, 2012.

[41] A. Tewari and S. C. Sharma, “Effect of different carrier gases and their flow rates on the growth of carbon nanotubes,” *Phys. Plasmas*, vol. 22, no. 4, 2015.

[42] S. Venkatesan, B. Visvalingam, G. Mannathusamy, V. Viswanathan, and A. G. Rao, “Effect of chemical vapor deposition parameters on the diameter of multi-walled carbon nanotubes,” *Int. Nano Lett.*, vol. 8, no. 4, pp. 297–308, 2018.

[43] M. Breckinridge, “Chapter 12,” in *Wide Neighborhoods*, no. Cvd, 2021, pp. 101–110.

[44] B. K. Mutuma, “Synthesis and characterization of solid, hollow, core-shell and worm-like carbon nanostructures for applications in organic photovoltaic devices and chemical sensors,” 2016.

[45] Y. Liu, H. Huang, W. Cao, B. Mao, Y. Liu, and Z. Kang, “Advances in carbon dots: from the perspective of traditional quantum dots,” *Mater. Chem. Front.*, vol. 4, no. 6, pp. 1586–1613, 2020.

[46] Y. Xu and X.-T. Yan, “Chemical Vapour Deposition Systems Design,” 2010, pp. 73–124.

[47] S. . I. . H. and R. . C. G . W . Young, “Flow Effects in a Vertical CVD Reactor,” vol. 52, no. 6, pp. 1509–1532, 2019.

[48] P. M. Gangatharan, M. S. Maubane-Nkadimeng, and N. J. Coville, “Building carbon structures inside hollow carbon spheres,” *Sci. Rep.*, vol. 9, no. 1, pp. 1–7, 2019.

[49] L. Zhang, J. S. Hu, X. H. Huang, J. Song, and S. Y. Lu, “Particle-in-box nanostructured materials created via spatially confined pyrolysis as high performance bifunctional catalysts for electrochemical overall water splitting,” *Nano Energy*, vol. 48, pp. 489–499, 2018.

[50] L. Zhang, H. Bin Wu, Y. Yan, X. Wang, and X. W. (David) Lou, “Hierarchical MoS2 microboxes constructed by nanosheets with enhanced electrochemical properties for lithium storage and water splitting,” *Energy Environ. Sci.*, vol. 7, no. 10, pp. 3302–3306, 2014.

[51] B. Cao *et al.*, “Graphitic Carbon Nanocage as a Stable and High Power Anode for Potassium-Ion Batteries,” *Adv. Energy Mater.*, vol. 8, no. 25, 2018.

[52] P. Ramakrishnan, S. G. Park, and S. Shanmugam, “Three-dimensional hierarchical nitrogen-doped arch and hollow nanocarbons: Morphological influences on

supercapacitor applications," *J. Mater. Chem. A*, vol. 3, no. 31, pp. 16242–16250, 2015.

[53] F. Liu *et al.*, "Carbon Nanomaterials With Hollow Structures: A Mini-Review," *Front. Chem.*, vol. 9, no. March, pp. 1–7, 2021.

[54] X.-Y. Yu, H. Hu, Y. Wang, H. Chen, and X. W. D. Lou, " Ultrathin MoS 2 Nanosheets Supported on N-doped Carbon Nanoboxes with Enhanced Lithium Storage and Electrocatalytic Properties ," *Angew. Chemie*, vol. 127, no. 25, pp. 7503–7506, 2015.

[55] F. Pei *et al.*, "From Hollow Carbon Spheres to N-Doped Hollow Porous Carbon Bowls: Rational Design of Hollow Carbon Host for Li-S Batteries," *Adv. Energy Mater.*, vol. 6, no. 8, 2016.

[56] J. Jiang *et al.*, "Nanohollow Carbon for Rechargeable Batteries: Ongoing Progresses and Challenges," *Nano-Micro Lett.*, vol. 12, no. 1, pp. 1–30, 2020.

[57] Z. Sun, S. Shen, L. Ma, D. Mao, and G. Lu, "Controlled synthesis of N-doped carbon spheres with different morphologies for supercapacitors," *RSC Adv.*, vol. 6, no. 106, pp. 104642–104647, 2016.

[58] H. Sun, Y. Zhu, B. Yang, Y. Wang, Y. Wu, and J. Du, "hollow carbon spheres for high-performance," pp. 12088–12097, 2016.

[59] H. Baloyi, N. J. Coville, and A. D. Wamwangi, "Synthesis of N-doped broken hollow carbon spheres and inorganic-organic hybrid perovskite materials for application in photovoltaic devices Master of Science in Chemistry."

[60] Z. N. Tetana, "Boron and nitrogen doped carbons for photochemical degradation reactions," 2013.

[61] B. K. Mutuma, C. I. Garcia-Martinez, R. C. Dias, B. J. Matsoso, N. J. Coville, and I. A. Hümmelgen, "Nitrogen-doped hollow carbon spheres as chemical vapour sensors," *New J. Chem.*, 2019.

[62] M. W. Dlamini, T. N. Phaahlamohlaka, D. O. Kumi, R. Forbes, L. L. Jewell, and N. J. Coville, "Post doped nitrogen-decorated hollow carbon spheres as a support for Co Fischer-Tropsch catalysts," *Catal. Today*, no. December 2018, pp. 0–1, 2019.

[63] T. Phaahlamohlaka, L. Jewell, and N. Coville, "Hollow carbon spheres as ideal supports for hydrogen spillover studies using ruthenium and cobalt nanoparticles," *Eur. Microsc. Congr. 2016 Proc.*, no. 1, pp. 1004–1005, 2016.

[64] J. Sanetuntikul, T. Hang, and S. Shanmugam, "Hollow nitrogen-doped carbon spheres as efficient and durable electrocatalysts for oxygen reduction," *Chem. Commun.*, vol.

50, no. 67, pp. 9473–9476, 2014.

[65] D. S. Bin, Y. S. Xu, S. J. Guo, Y. G. Sun, A. M. Cao, and L. J. Wan, "Manipulating Particle Chemistry for Hollow Carbon-based Nanospheres: Synthesis Strategies, Mechanistic Insights, and Electrochemical Applications," *Acc. Chem. Res.*, vol. 54, no. 1, pp. 221–231, 2021.

[66] X. Chen *et al.*, "Synthesis , Growth Mechanism , and Electrochemical Properties of Hollow Mesoporous Carbon Spheres with Controlled Diameter," pp. 17717–17724, 2011.

[67] T. Ariyanto, G. R. Zhang, A. Kern, and B. J. M. Etzold, "Preparation of hollow mesoporous carbon spheres and their performances for electrochemical applications," *IOP Conf. Ser. Mater. Sci. Eng.*, vol. 316, no. 1, pp. 2–7, 2018.

[68] S. Li, A. Pasc, V. Fierro, and A. Celzard, "Hollow carbon spheres, synthesis and applications-a review," *J. Mater. Chem. A*, vol. 4, no. 33, pp. 12686–12713, 2016.

[69] J. Xu, F. He, S. Gai, S. Zhang, L. Li, and P. Yang, "Nitrogen-enriched, double-shelled carbon/layered double hydroxide hollow microspheres for excellent electrochemical performance," *Nanoscale*, vol. 6, no. 18, pp. 10887–10895, 2014.

[70] X. Li, L. Zhang, and G. He, "Fe3O4 doped double-shelled hollow carbon spheres with hierarchical pore network for durable high-performance supercapacitor," *Carbon N. Y.*, vol. 99, pp. 514–522, 2016.

[71] H. J. Fan, "New way to multi-shelled hollow spheres for robust battery electrode," *Inorg. Chem. Front.*, vol. 3, no. 8, pp. 1004–1006, 2016.

[72] Y. Jiang, X. Qian, C. Zhu, H. Liu, and L. Hou, *Nickel Cobalt Sulfide Double-Shelled Hollow Nanospheres as Superior Bifunctional Electrocatalysts for Photovoltaics and Alkaline Hydrogen Evolution*, vol. 10, no. 11. 2018.

[73] J. Qi *et al.*, "Multi-shelled hollow micro-/nanostructures," *Chem. Soc. Rev.*, vol. 44, no. 19, pp. 6749–6773, 2015.

[74] I. A. Rutkowska and P. J. Kulesza, "Metal Oxide Cluster and Polyoxometallate Supports for Noble Metal Nanoparticles in Efficient Electrocatalysis," K. B. T.-E. of I. C. Wandelt, Ed. Oxford: Elsevier, 2018, pp. 207–216.

[75] L. Mao, Y. Wang, Y. Zhong, J. Ning, and Y. Hu, "Microwave-assisted deposition of metal sulfide/oxide nanocrystals onto a 3D hierarchical flower-like TiO2 nanofile:///Users/thelma/Downloads/Controllable growth of SnS2:SnO2 heterostructured nanoplates via a hydrothermal-assisted self-hydrolysis process a," *J. Mater. Chem. A*, vol. 1, no. 28, pp. 8101–8104, 2013.

[76] L. Mao, J. Li, Y. Xie, Y. Zhong, and Y. Hu, “Controllable growth of SnS2/SnO2 heterostructured nanoplates via a hydrothermal-assisted self-hydrolysis process and their visible-light-driven photocatalytic reduction of Cr(vi),” *RSC Adv.*, vol. 4, no. 56, pp. 29698–29701, 2014.

[77] A. Mittal, S. Sharma, V. Kumari, S. Yadav, N. S. Chauhan, and N. Kumar, “Highly efficient, visible active TiO2/CdS/ZnS photocatalyst, study of activity in an ultra low energy consumption LED based photo reactor,” *J. Mater. Sci. Mater. Electron.*, vol. 30, no. 19, pp. 17933–17946, 2019.

[78] J. L. Bredas, “Mind the gap!,” *Mater. Horizons*, vol. 1, no. 1, pp. 17–19, 2014.

[79] A. Balakrishnan, J. D. Groeneveld, S. Pokhrel, and L. Mädler, “Metal Sulfide Nanoparticles: Precursor Chemistry,” *Chem. - A Eur. J.*, vol. 27, no. 21, pp. 6390–6406, 2021.

[80] J. Wang, S. Lin, N. Tian, T. Ma, Y. Zhang, and H. Huang, “Nanostructured Metal Sulfides: Classification, Modification Strategy, and Solar-Driven CO2 Reduction Application,” *Adv. Funct. Mater.*, vol. 31, no. 9, pp. 1–39, 2021.

[81] M. Nguyen *et al.*, “In situ photo-assisted deposition of MoS2 electrocatalyst onto zinc cadmium sulphide nanoparticle surfaces to construct an efficient photocatalyst for hydrogen generation,” *Nanoscale*, vol. 5, no. 4, pp. 1479–1482, 2013.

[82] P. Kulkarni, S. K. Nataraj, R. G. Balakrishna, D. H. Nagaraju, and M. V. Reddy, “Nanostructured binary and ternary metal sulfides: Synthesis methods and their application in energy conversion and storage devices,” *J. Mater. Chem. A*, vol. 5, no. 42, pp. 22040–22094, 2017.

[83] G. Fu and J. M. Lee, “Ternary metal sulfides for electrocatalytic energy conversion,” *J. Mater. Chem. A*, vol. 7, no. 16, pp. 9386–9405, 2019.

[84] D. G. Moon *et al.*, “A review on binary metal sulfide heterojunction solar cells,” *Sol. Energy Mater. Sol. Cells*, vol. 200, no. March, p. 109963, 2019.

[85] C. H. Lai, M. Y. Lu, and L. J. Chen, “Metal sulfide nanostructures: Synthesis, properties and applications in energy conversion and storage,” *J. Mater. Chem.*, vol. 22, no. 1, pp. 19–30, 2012.

[86] Y. Guo *et al.*, “Copper(I) sulfide: a two-dimensional semiconductor with superior oxidation resistance and high carrier mobility,” *Nanoscale Horizons*, vol. 4, no. 1, pp. 223–230, 2019.

[87] C. S. Kim, S. H. Choi, and J. H. Bang, “New insight into copper sulfide electrocatalysts for quantum dot-sensitized solar cells: Composition-dependent

electrocatalytic activity and stability," *ACS Appl. Mater. Interfaces*, vol. 6, no. 24, pp. 22078–22087, 2014.

[88] T. Serrano and I. Gómez, "One pot synthesis, growth mechanism and optical properties of PbS/Cu 2S core-shell nanoparticles," *Lect. Notes Eng. Comput. Sci.*, vol. 3 LNECS, pp. 2087–2090, 2013.

[89] M. Giancaspro *et al.*, " Cu 2−x S nanocrystal synthesis: a chemical toolbox for controlling nanocrystal geometry, phase and plasmonic behavior ," *Mater. Chem. Front.*, vol. 5, no. 3, pp. 1341–1354, 2021.

[90] C. Coughlan, M. Ibáñez, O. Dobrozhan, A. Singh, A. Cabot, and K. M. Ryan, "Compound copper chalcogenide nanocrystals," *Chem. Rev.*, vol. 117, no. 9, pp. 5865–6109, 2017.

[91] M. Lotfipour, T. MacHani, D. P. Rossi, and K. E. Plass, "α-Chalcocite nanoparticle synthesis and stability," *Chem. Mater.*, vol. 23, no. 12, pp. 3032–3038, 2011.

[92] A. Morales-García, A. L. Soares, E. C. Dos Santos, H. A. De Abreu, and H. A. Duarte, "First-principles calculations and electron density topological analysis of covellite (CuS)," *J. Phys. Chem. A*, vol. 118, no. 31, pp. 5823–5831, 2014.

[93] H. T. EVANS, "Crystal Structure of Low Chalcocite," *Nat. Phys. Sci.*, vol. 232, no. 29, pp. 69–70, 1971.

[94] H. T. Evans, "Djurleite (Cu1.94S) and Low Chalcocite (Cu2S): New Crystal Structure Studies," *Science*, vol. 203, no. 4378, pp. 356–358, 1979.

[95] A. Putnis, "Electron diffraction study of phase transformations in copper sulfides," *Am. Mineral.*, vol. 62, no. 1–2, pp. 107–114, 1977.

[96] K. Koto and N. Morimoto, "The crystal structure of anilite," *Acta Crystallogr. Sect. B Struct. Crystallogr. Cryst. Chem.*, vol. 26, no. 7, pp. 915–924, 1970.

[97] Q. Xu, B. Huang, Y. Zhao, Y. Yan, R. Noufi, and S. H. Wei, "Crystal and electronic structures of Cu xS solar cell absorbers," *Appl. Phys. Lett.*, vol. 100, no. 6, 2012.

[98] Y. Zhao, H. Pan, Y. Lou, X. Qiu, J. Zhu, and C. Burda, "Plasmonic Cu 2-xS nanocrystals: Optical and structural properties of copper-deficient copper(I) sulfides," *J. Am. Chem. Soc.*, vol. 131, no. 12, pp. 4253–4261, 2009.

[99] M. Singh, M. Goyal, and K. Devlal, "Size and shape effects on the band gap of semiconductor compound nanomaterials," *J. Taibah Univ. Sci.*, vol. 12, no. 4, pp. 470–475, 2018.

[100] G. Ramalingam *et al.*, "Quantum Confinement Effect of 2D Nanomaterials," *Quantum Dots - Fundam. Appl.*, pp. 1–12, 2020.

[101] J. M. Luther, P. K. Jain, T. Ewers, and A. P. Alivisatos, “Localized surface plasmon resonances arising from free carriers in doped quantum dots,” *Nat. Mater.*, vol. 10, no. 5, pp. 361–366, 2011.

[102] Y. Jiang, S. Zhang, Q. Ji, J. Zhang, Z. Zhang, and Z. Wang, “Ultrathin Cu7S4 nanosheets-constructed hierarchical hollow cubic cages: one-step synthesis based on Kirkendall effect and catalysis property,” *J. Mater. Chem. A*, vol. 2, no. 13, pp. 4574–4579, 2014.

[103] P. Roy and S. K. Srivastava, “Solvothermal growth of flower-like morphology from nanorods of copper sulfides.,” *J. Nanosci. Nanotechnol.*, vol. 8, no. 3, pp. 1523–1527, Mar. 2008.

[104] P. Roy and S. K. Srivastava, “Nanostructured copper sulfides: Synthesis, properties and applications,” *CrystEngComm*, vol. 17, no. 41, pp. 7801–7815, 2015.

[105] M. Kruszynska *et al.*, “Size and shape control of colloidal copper(I) sulfide nanorods,” *ACS Nano*, vol. 6, no. 7, pp. 5889–5896, 2012.

[106] J. Chang and E. R. Waclawik, “Colloidal semiconductor nanocrystals: Controlled synthesis and surface chemistry in organic media,” *RSC Adv.*, vol. 4, no. 45, pp. 23505–23527, 2014.

[107] Y. Wang *et al.*, “One-pot synthesis and optical property of copper(I) sulfide nanodisks,” *Inorg. Chem.*, vol. 49, no. 14, pp. 6601–6608, 2010.

[108] N. T. K. Thanh, N. Maclean, and S. Mahiddine, “Mechanisms of nucleation and growth of nanoparticles in solution,” *Chem. Rev.*, vol. 114, no. 15, pp. 7610–7630, 2014.

[109] J. Lee, J. Yang, S. G. Kwon, and T. Hyeon, “Nonclassical nucleation and growth of inorganic nanoparticles,” *Nat. Rev. Mater.*, vol. 1, no. 8, 2016.

[110] J. Polte, “Fundamental growth principles of colloidal metal nanoparticles – a new perspective,” pp. 6809–6830, 2015.

[111] M. Nasilowski, B. Mahler, E. Lhuillier, S. Ithurria, and B. Dubertret, “Two-Dimensional Colloidal Nanocrystals,” *Chem. Rev.*, vol. 116, no. 18, pp. 10934–10982, 2016.

[112] V. K. La Mer, “Nucleation in Phase Transitions.,” *Ind. Eng. Chem.*, vol. 44, no. 6, pp. 1270–1277, 1952.

[113] V. K. LaMer and R. H. Dinegar, “Theory, Production and Mechanism of Formation of Monodispersed Hydrosols,” *J. Am. Chem. Soc.*, vol. 72, no. 11, pp. 4847–4854, Nov. 1950.

[114] T. Sugimoto, “CHAPTER 8 - CONTROL OF PARTICLE CHARACTERISTICS,” T. B. T.-M. P. Sugimoto, Ed. Amsterdam: Elsevier, 2001, pp. 368–452.

[115] W. Ostwald, “About the supposed isomerism of the red and yellow mercury oxide and the surface tension of solid bodies,” *Zeitschrift für Phys. Chemie*, vol. 34U, no. 1, pp. 495–503, 1900.

[116] T. Sugimoto, “Preparation of monodispersed colloidal particles,” *Adv. Colloid Interface Sci.*, vol. 28, pp. 65–108, 1987.

[117] W. Lee *et al.*, “Redox−Transmetalation Process as a Generalized Synthetic Strategy for Core−Shell Magnetic Nanoparticles,” *J. Am. Chem. Soc.*, vol. 127, no. 46, pp. 16090–16097, Nov. 2005.

[118] M. A. Watzky and R. G. Finke, “Nanocluster Size-Control and ‘Magic Number’ Investigations. Experimental Tests of the ‘Living-Metal Polymer’ Concept and of Mechanism-Based Size-Control Predictions Leading to the Syntheses of Iridium(0) Nanoclusters Centering about Four Sequential Magic ,” *Chem. Mater.*, vol. 9, no. 12, pp. 3083–3095, Dec. 1997.

[119] S. R. K. Perala and S. Kumar, “On the Two-Step Mechanism for Synthesis of Transition-Metal Nanoparticles,” *Langmuir*, vol. 30, no. 42, pp. 12703–12711, Oct. 2014.

[120] Z. A. Peng and X. Peng, “Mechanisms of the Shape Evolution of CdSe Nanocrystals,” *J. Am. Chem. Soc.*, vol. 123, no. 7, pp. 1389–1395, Feb. 2001.

[121] X. Peng *et al.*, “Shape control of CdSe nanocrystals,” *Nature*, vol. 404, no. 6773, pp. 59–61, 2000.

[122] H. Zheng, R. K. Smith, Y.-W. Jun, C. Kisielowski, U. Dahmen, and A. P. Alivisatos, “Observation of single colloidal platinum nanocrystal growth trajectories.,” *Science*, vol. 324, no. 5932, pp. 1309–1312, Jun. 2009.

[123] M. Niederberger and H. Cölfen, “Oriented attachment and mesocrystals: Non-classical crystallization mechanisms based on nanoparticle assembly,” *Phys. Chem. Chem. Phys.*, vol. 8, no. 28, pp. 3271–3287, 2006.

[124] D. Li, M. H. Nielsen, J. R. I. Lee, C. Frandsen, J. F. Banfield, and J. J. De Yoreo, “Direction-Specific Interactions Control Crystal Growth by Oriented Attachment,” *Science (80-.).*, vol. 336, no. 6084, pp. 1014 LP – 1018, May 2012.

[125] T. V Arjunan and T. S. Senthil, “Review: Dye sensitised solar cells,” *Mater. Technol.*, vol. 28, no. 1–2, pp. 9–14, 2012.

[126] A. Hagfeldt, “Brief overview of dye-sensitized solar cells,” *Ambio*, vol. 41, no.

SUPPL.2, pp. 151–155, 2012.

[127] A. Drygala, “Influence of TiO2film thickness on photovoltaic properties of dye-sensitized solar cells,” *IOP Conf. Ser. Earth Environ. Sci.*, vol. 642, no. 1, 2021.

[128] V. V. Tyagi, N. A. A. Rahim, N. A. Rahim, and J. A. L. Selvaraj, “Progress in solar PV technology: Research and achievement,” *Renew. Sustain. Energy Rev.*, vol. 20, pp. 443–461, 2013.

[129] A. Karmakar and J. Ruparelia, “A Critical Review on Dye Sensitized Solar Cells,” *Nuicone.Org*, pp. 1–5, 2011.

[130] M. T. Kibria, A. Ahammed, S. M. Sony, F. Hossain, and Shams-UI-Islam, “A Review : Comparative studies on different generation solar cells technology,” *Int. Conf. Environ. Asp. Bangladesh*, pp. 51–53, 2014.

[131] J. A. Luceño-Sánchez, A. M. Díez-Pascual, and R. P. Capilla, “Materials for photovoltaics: State of art and recent developments,” *Int. J. Mol. Sci.*, vol. 20, no. 4, p. 976, 2019.

[132] B. B. M. Rawal N., Vaishaly A.G., Sharma H., “Dye Sensitized Solar Cells: The Emerging Technology,” *Energy Power Eng. Sci.*, vol. 2, no. 2, pp. 46–52, 2015.

[133] J. Wu *et al.*, “Counter electrodes in dye-sensitized solar cells,” *Chem. Soc. Rev.*, vol. 46, no. 19, pp. 5975–6023, 2017.

[134] M. Wu and T. Ma, “Platinum-free catalysts as counter electrodes in dye-sensitized solar cells,” *ChemSusChem*, vol. 5, no. 8, pp. 1343–1357, 2012.

[135] M. Aftabuzzaman and H. K. Kim, “Porous Carbon Materials as Supreme Metal-Free Counter Electrode for Dye-Sensitized Solar Cells,” *Emerg. Sol. Energy Mater.*, no. August, 2018.

[136] O. J. Guy and K. A. D. Walker, *Graphene Functionalization for Biosensor Applications*, Second Edi. Elsevier Inc., 2016.

[137] N. Elgrishi, K. J. Rountree, B. D. McCarthy, E. S. Rountree, T. T. Eisenhart, and J. L. Dempsey, “A Practical Beginner’s Guide to Cyclic Voltammetry,” *J. Chem. Educ.*, vol. 95, no. 2, pp. 197–206, 2018.

[138] L. Zhou *et al.*, “Controlled synthesis of CuInS2/reduced graphene oxide nanocomposites for efficient dye-sensitized solar cells,” *J. Power Sources*, vol. 272, pp. 639–646, 2014.

[139] J. Y. Chang, S. C. Chang, S. H. Tzing, and C. H. Li, “Development of nonstoichiometric CuInS2 as a light-harvesting photoanode and catalytic photocathode in a sensitized solar cell,” *ACS Appl. Mater. Interfaces*, vol. 6, no. 24, pp. 22272–

22281, 2014.

[140] M. Ye, Q. Liu, J. Iocozzia, X. Hong, X. Liu, and Z. Lin, “Polycomponent Electrocatalysts for I-Mediated Dye-Sensitized Solar Cells,” *Counter Electrodes for Dye-sensitized and Perovskite Solar Cells*. pp. 323–348, 22-Oct-2018.

[141] G. Yue, X. Ma, W. Zhang, F. Li, J. Wu, and G. Li, “A highly efficient flexible dye-sensitized solar cell based on nickel sulfide/platinum/titanium counter electrode,” *Nanoscale Res. Lett.*, vol. 10, no. 1, pp. 1–9, 2015.

[142] M. Pazoki, U. B. Cappel, E. M. J. Johansson, A. Hagfeldt, and G. Boschloo, “Characterization techniques for dye-sensitized solar cells,” *Energy Environ. Sci.*, vol. 10, no. 3, pp. 672–709, 2017.

[143] H. Hardani, H. Hendra, M. I. Darmawan, C. Cari, and A. Supriyanto, “Fabrication of dye natural as a photosensitizers in dye-sensitized solar cells (DSSC),” *J. Phys. Theor. Appl.*, vol. 1, no. 1, p. 21, 2017.

[144] F. O. Otieno, “Enhancement of photo-conversion efficiency of organic solar cells by plasmon resonance effect,” 2015.

[145] M. Airo, “Synthesis and characterization of metal selenide nanocrystals for use in electronic devices,” University of Witwatersrand.

[146] M. Wu, Y. nan Lin, H. Guo, W. Li, Y. Wang, and X. Lin, “Design a novel kind of open-ended carbon sphere for a highly effective counter electrode catalyst in dye-sensitized solar cells,” *Nano Energy*, vol. 11, no. 2015, pp. 540–549, 2015.

[147] B. Fang *et al.*, “Incorporating Hierarchical Nanostructured Carbon Counter Electrode into Metal-Free Organic Dye-Sensitized Solar Cell,” *Langmuir*, vol. 26, no. 13, pp. 11238–11243, Jul. 2010.

[148] G. Wanga, L. Wang, and S. Zhuo, “Enhancing the performance of dye-sensitized solar cells by incorporating mesoporous carbon in polymer gel electrolyte,” *Mater. Sci. Forum*, vol. 685, pp. 44–47, 2011.

[149] G. Wang, J. Zhang, S. Kuang, and S. Zhuo, “Nitrogen-doped porous carbon prepared by a facile soft-templating process as low-cost counter electrode for High-performance dye-sensitized solar cells,” *Mater. Sci. Semicond. Process.*, vol. 38, pp. 234–239, 2015.

[150] M. Chen and L. L. Shao, “Review on the recent progress of carbon counter electrodes for dye-sensitized solar cells,” *Chem. Eng. J.*, vol. 304, pp. 629–645, 2016.

[151] M. R. Samantaray *et al.*, “Synergetic Effects of Hybrid Carbon Nanostructured Counter Electrodes for Dye-Sensitized Solar Cells: A Review,” *Materials* , vol. 13, no.

12. 2020.

[152] E. Meyer, A. Bede, N. Zingwe, and R. Taziwa, “Metal sulphides and their carbon supported composites as platinum-free counter electrodes in dye-sensitized solar cells: A review,” *Materials (Basel).*, vol. 12, no. 12, 2019.

[153] S. Peng, F. Cheng, J. Shi, J. Liang, Z. Tao, and J. Chen, “High-surface-area microporous carbon as the efficient photocathode of dye-sensitized solar cells,” *Solid State Sci.*, vol. 11, no. 12, pp. 2051–2055, 2009.

[154] E. Ramasamy, J. Chun, and J. Lee, “Soft-template synthesized ordered mesoporous carbon counter electrodes for dye-sensitized solar cells,” *Carbon N. Y.*, vol. 48, no. 15, pp. 4563–4565, 2010.

[155] Y. Chen, Y. Zhu, and Z. Chen, “Three-dimensional ordered macroporous carbon as counter electrodes in dye-sensitized solar cells,” *Thin Solid Films*, vol. 539, pp. 122–126, 2013.

[156] S. H. Park, H. R. Jung, and W. J. Lee, “Hollow activated carbon nanofibers prepared by electrospinning as counter electrodes for dye-sensitized solar cells,” *Electrochim. Acta*, vol. 102, pp. 423–428, 2013.

[157] W. Yang *et al.*, “Nitrogen-Enriched Hollow Carbon Spheres Coupled with Efficient Co-Nx-C Species as Cathode Catalysts for Triiodide Reduction in Dye-Sensitized Solar Cells,” *ACS Sustain. Chem. Eng.*, vol. 7, no. 2, pp. 2679–2685, 2019.

[158] A. Hessein and A. A. El-Moneim, “Two-step synthesis of copper sulfide-graphene counter electrode for cds quantum dot sensitized solar cells,” *Key Eng. Mater.*, vol. 786 KEM, pp. 400–408, 2018.

[159] A. Krishna Prasad, I.-R. Jo, S.-H. Kang, and K.-S. Ahn, “Novel method for synthesis of reduced graphene oxide–Cu2S and its application as a counter electrode in quantum-dot-sensitized solar cells,” *Appl. Surf. Sci.*, vol. 564, no. June, p. 150393, 2021.

[160] H. Chen, J. Wang, C. Jia, J. Mou, and L. Zhu, “Highly efficient dye-sensitized solar cell with a novel nanohybrid film of Cu2ZnSnS4-MWCNTs as counter electrode,” *Appl. Surf. Sci.*, vol. 422, pp. 591–596, 2017.

[161] G. Sankar, P. Anbarasu, R. Mahendran, K. Rajendran, and T. Sivakumar, “Pt-free and efficient counter electrode with nanostructured CoNi2S4/rGO for dye-sensitized solar cells,” *Inorg. Chem. Commun.*, vol. 126, no. January, p. 108475, 2021.

[162] X. Luo, Y. Zhang, and S. H. Kim, “Incorporation of Nanostructured Carbon Composite Materials into Counter Electrodes for Highly Efficient Dye-Sensitized

Solar Cells," *Nanoscale Res. Lett.*, vol. 13, pp. 1–10, 2018.

[163] E. T. MOMBESHORA, R. SIMOYI, V. O. NYAMORI, and P. G. NDUNGU, "Multiwalled carbon nanotube-titania nanocomposites: Understanding nano-structural parameters and functionality in dye-sensitized solar cells," *South African J. Chem.*, vol. 68, pp. 153–164, 2015.

[164] L. Saad, M. Y. Feteha, S. Ebrahim, M. Soliman, and T. M. Abdel-Fattah, "Dye Sensitized Solar Cell Based on Polyaniline-Carbon Nanotubes/Graphite Composite," *ECS J. Solid State Sci. Technol.*, vol. 3, no. 10, pp. M55–M60, 2014.

[165] Y. Chen, H. Zhang, Y. Chen, and J. Lin, "Study on Carbon Nanocomposite Counterelectrode for Dye-Sensitized Solar Cells," *J. Nanomater.*, vol. 2012, pp. 1–6, 2012.

[166] S. K. Barman and M. N. Huda, "Stability enhancement of Cu2S against Cu vacancy formation by Ag alloying," *J. Phys. Condens. Matter*, vol. 30, no. 16, p. 165701, 2018.

[167] Y. Zhang *et al.*, "Double-shelled hollow carbon sphere with microporous outer shell towards high performance lithium-sulfur battery," *Electrochim. Acta*, vol. 284, pp. 89–97, 2018.

Chapter 3

Synthesis and characterization of porous nitrogen-doped hollow carbon spheres

3.1 Introduction

Endotemplating and exotemplating also known as soft and hard templating respectively have remained two of the primary synthesis routes in the preparation of hollow carbon spheres. Although different modifications have been made under these two classifications over the years such as the addition of polyvinylpyrrolidone to the hard silica template [1] the basis of these synthesis techniques has remained the same over the years. In the process, a core is removed from a core-shell particle to give a negative replica of the original template. Soft templating synthesis refers to the use of soft matter. Such as vesicae, micelles, gas bubbles, polymer aggregates, or emulsions are used to make the core (**Figure 3.1**) [2]–[4]. Due to the fragility of the soft matter, the morphology of the targeted end product is harder to control [5]. Therefore, because of this disadvantage, the hard template method is preferable as it gives better synthesis control and because of the rigid mold, the resulting inverse replicas are more likely to have structural uniformity [6].

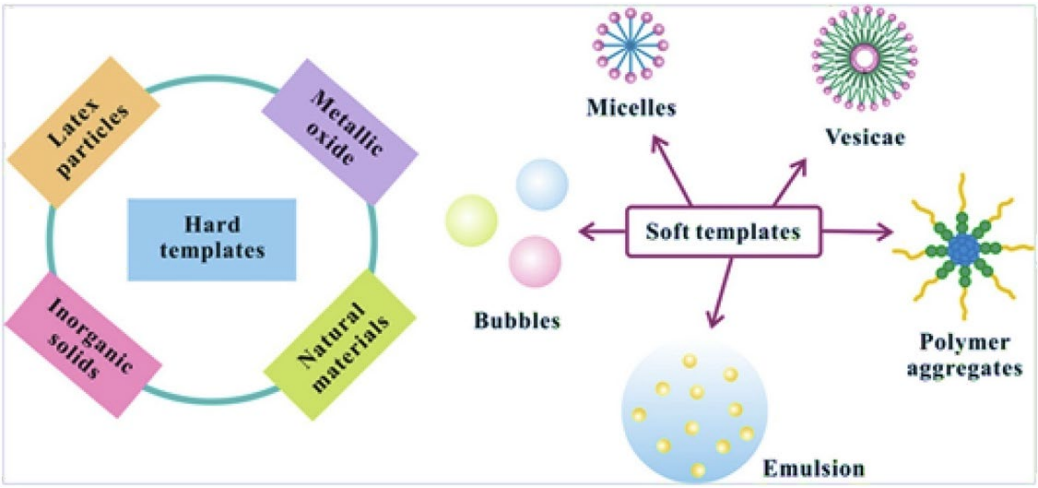


Figure 3.1: Different types of template materials that can be used for the synthesis of hollow materials [4].

For the synthesis of hollow carbon spheres using the hard template approach, silica (SiO_2) is the most frequently used matrix. This is due to its inorganic nature and excellent properties such as; being cost-effective, having great chemical stability, and that it is easily malleable [7]. The formation of SiO_2 can either be carried out using the sol-gel or the Stöber method. During the sol-gel method, silicon alkoxides ($Si(OR)_4$) in their monomer form such as (TEOS; tetraethylorthosilicate ($Si(OC_2H_5)_4$)) undergoes hydrolysis and condensation in the presence of an acid (e.g. HCl) or a base (e.g. NH_3) which acts as a catalyst for the reaction. In terms of TEOS, its hydrolysis forms silanol groups which are then converted to siloxane bridges (Si-O-Si) due to the condensation reaction between the silanol molecules or silanol and ethoxy molecules [8]–[10]. This creates a silica structure.

Primarily both methods undergo the same reactions; hydrolysis (Equation 1) where the ethoxy groups of TEOS molecules are attacked by the hydroxyl anions from water to form the intermediate [$Si(OC_2H_5)_{4-x}(OH)_x$]. The condensation reaction then occurs immediately with the intermediate hydroxyl group either reacting with another ethoxy group in TEOS to undergo alcohol condensation (Equation 2) or it reacts with a hydroxyl group of another intermediate which would result in water condensation (Equation 3) to form SiO_2 [11]. However, the Stöber method has the main advantage of the ability to control the distribution, morphology, and particle size by methodical variation of the reaction parameters [12].

$$Si\,(OC_2H_5)_4 + xH_2O \xrightarrow{\text{hydrolysis}} Si\,(OC_2H_5)_{4-x}\,(OH)_x + x\,C_2H_5OH \qquad (1)$$

$$\equiv Si - OC_2H_5 + HO - Si \equiv \xrightarrow{\text{alcohol condensation}} \equiv Si - O - Si \equiv + C_2H_5OH \qquad (2)$$

$$\equiv Si - OH + HO - Si \equiv \xrightarrow{\text{water condensation}} \equiv Si - O - Si \equiv + H_2O \qquad (3)$$

The overall reaction is:

$$Si\,(OC_2H_5)_4 + 2H_2O \rightarrow SiO_2 + 4C_2H_5OH$$

In comparison to typical solid silica spheres, mesoporous silica has attracted a substantial amount of interest due to its low toxicity, high surface area, permeability, well-ordered structure, high thermal stability, uniform pore distribution and, ability to productively react with other materials [13], [14]. The dense nonporous shell of the solid silica provides a limited surface area and a small number of active sites for binding, functionalization and, adsorption [15]. It is however more favourable to introduce a porous shell on the silica surface through

the use of pore-forming agents such as n-octadecyltrimethoxysilane (C_{18}TMS), cetyltrimethylammonium chloride (CTAC), or cetyltrimethylammonium bromide (CTAB) in a modified Stöber silica synthesis method [16], [10]. The synthesis of hollow carbon spheres is primarily dependent on the template used to obtain the spherical structures. Therefore this is one of the most important parts of the synthesis as the template can affect the carbon shell properties.

In recent research, single-shelled and double-shelled hollow carbon spheres have been synthesized using these mesoporous hard silica templates. They were found to exhibit excellent properties which include high surface area, good mass transport due to the cavity volume, good electrical conductivity, and great chemical, mechanical and thermal stability [17]–[19]. Due to these properties and the porous nature of these materials, they have played a pivotal role in electrochemical applications largely due to their high surface area that provides innumerable active sites for electrocatalytic activity [20]–[22]. Depending on the experimental parameters and the carbon source chosen, different carbonization techniques can be employed using exotemplating. These techniques include hydrothermal carbonization (HTC), chemical vapor deposition (CVD), arc-discharge, and laser ablation [3]. However, CVD synthesis is the most commonly used route as it is reproducible and results in the synthesis of high-quality carbon materials [23]. The carbon materials are then annealed at high temperatures to purify [24] and enhance their properties such as porosity [25].

For a typical single-shelled hollow carbon spheres synthesis via a CVD route, the rigid template is synthesized with characteristics resembling the desired end product morphology. The as-synthesized template is then coated with the chosen carbon precursor at high temperatures (> 600 ºC) in an inert atmosphere. Thereafter the silica template is then etched out using hydrofluoric acid (HF) or sodium hydroxide (NaOH) leaving a negative replica. These synthesis steps will be followed in this study to produce mesoporous single and double-shelled hollow carbon spheres. To achieve this mesoporous silica will be synthesized and used as the sacrificial templates. For double-shelled hollow carbon spheres, solid mesoporous silica spheres are synthesized followed by selective etching of the resulting silica spheres. This produces ring-shaped silica templates that are then carbonized using the CVD process detailed above and then the silica is etched out to produce mesoporous double-shelled hollow carbon spheres.

Doping of carbon materials with nitrogen (N) can improve their catalytic activity and electrochemical reactions [26], [6]. It has been noted in previous research that the heat treatment of N-doped carbon has the potential of detaching nitrogen atoms from the surface. To eliminate this drawback, post-synthesis doping can be implemented [27]. The incorporation of nitrogen atoms into the layers of carbon material can occur to give four types of C-N bonds (**Figure 3.2**). The formation of quaternary-N involves the simple substitution of a single C atom with a N atom resulting in N being bonded to three carbon atoms. Substitution to give nitrogen that would be bonded to two carbon atoms creates pyridinic-N (sp^2 hybridization). The N atom can also be bonded to two carbons and a O atom to give pyridinic N-O. Pyrrolic-N is formed when a N atom is included in a pentagonal ring (sp^2 or sp^3 hybridization) [28], [29]. Some experimental studies have indicated that high concentrations of pyrrolic and pyridinic nitrogen atom configurations improve carbon materials through enhanced hydrogen bonding and pi-bond interactions resulting in enhanced electrocatalytic performances and biocompatibility [30].

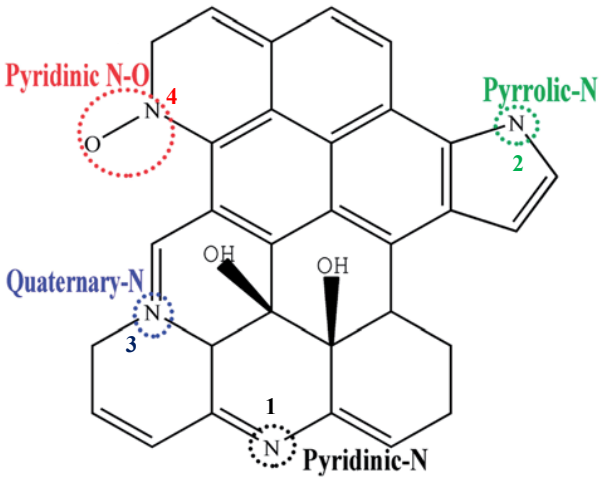


Figure 3.2: Nitrogen atom configurations in carbon materials: (1) pyridinic-N, (2) pyrrolic-N, and (3) quaternary-N [31].

Given that porous carbon shells, nitrogen doping, and the addition of carbon shells enhances the properties of hollow carbon spheres. In this study, single-shelled and double-shelled hollow carbon spheres will be synthesized with these properties to improve their electrochemical performance. Xu *et al*. found that nitrogen-doped double-shelled hollow carbon spheres exhibited great electrochemical properties, therefore, their template synthesis will be used to produce double-shelled hollow carbon spheres for this study [32]. Double-shelled HCSs

amplify the advantages and properties of HCSs. The increased surface area and large void allow for more catalytic reactions to occur [33]. Therefore, in this research, the properties of the synthesized single and double-shelled HCSs will be compared to determine the carbon material with great properties. Due to the advantages of CVD synthesis, horizontal CVD will be used to produce high-quality carbon materials which will then be purified by annealing them at high temperatures. Carbon and nitrogen sources will be varied to study the change in properties of the HCSs and obtain the carbon materials with the best catalytic abilities.

3.2 Experimental

3.2.1 Starting materials

Tetraethylorthosilicate, (TEOS, 98%, Aldrich), hexadecyltrimethylammonium bromide (≥ 98 %) (CTAB), octadecyltrimethoxysilane, (C_{18}TMS, 90%, Aldrich), ammonium hydroxide, (NH_4OH, 25% Fluka), ethanol (C_2H_5OH, 96%, Merck), sodium carbonate (Na_2CO_3, 99.5%, Merck) and deionized water were used as reagents for the synthesis of the pristine and mesoporous SiO_2 spheres. Hydrofluoric acid, (HF; 40%, Associated Chemical) was used for etching SiO_2. Acetylene (C_2H_2, 99.5%, Aldrich) and toluene (C_7H_8, 99.5%, Aldrich) were used as a carbon source and, argon (Ar) as the carrier gas.

3.2.2 Synthesis of mesoporous silica spheres and their single-shelled hollow carbon spheres

(i) SiO_2 synthesis

Silica spheres were synthesized by preparing a solution of 180 ml of ethanol (ETOH), 60 mL of distilled water (H_2O), and 10 mL of ammonium hydroxide (NH_4OH) which was then stirred for 10 min at room temperature. After the ETOH- H_2O- NH_4OH solution had been stirred, 35 mL of tetraethylorthosilicate (TEOS) was added slowly to obtain polydispersed silica spheres and the resulting solution was stirred at room temperature for 1 h [1], [34].

(ii) Mesoporous SiO_2 (m- SiO_2) synthesis

In 30 ml of ethanol, 1mL TEOS and 5ml of C_{18}TMS were dispersed and the resulting solution was then added to the solution of synthesized polydispersed silica spheres described above in part (i). The solution was then stirred for 6 h at room temperature to form the porous shell on the preformed silica. The synthesized mesoporous polydispersed SiO_2 spheres (m-SiO_2) were washed three times with an ethanol-water solution to remove undesired particles, centrifuged

at 4500 rpm for 20 min, oven-dried at 80 ºC for 12 h, and then calcined at 600 ºC for 6 h to remove any unreacted particles. This method of mesoporous silica synthesis produced a high yield, between 8-10 g.

(iii) Carbonization of m-SiO_2

Carbonization of m-SiO_2 spheres was carried out using the horizontal CVD method. In the process, 4 g of m-SiO_2 was placed in a quartz boat which was then placed in the horizontal quartz reactor and heated up to 900 ºC at a ramp rate of 10 ml/min under a constant supply of Ar gas with a flow rate of 100 ml/min. Acetylene gas and liquid toluene were used as the carbon precursors, acetylene gas was introduced into the reactor with Ar as the diluent gas. For liquid toluene, a bubbler was used to transport the liquid precursor using Ar gas as the carrier gas. **Figure 3.3** Once the reaction temperature of 900 ºC was reached, either acetylene gas or toluene was introduced into the reactor by use of a carrier gas for 2 h and then the reactor was allowed to cool to room temperature. Removal of the silica core particle was done using 10 % hydrofluoric acid (HF) for 24 h at room temperature. The synthesized hollow carbon spheres were filtered, washed with distilled water, and dried then annealed at 900 ºC under Ar gas for 1 h. This yielded 1.5 g – 2.0 g of carbon was collected after washing and drying.

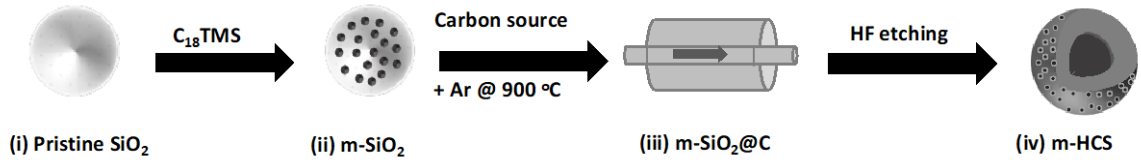


Figure 3.3: Schematic diagram depicting the synthesis of single-shelled mesoporous hollow carbon spheres.

3.2.3 Synthesis of double-shelled hollow carbon spheres

(i) Double-shelled m-SiO_2

Solution A was made up of 70 mL of ethanol, 15 mL of distilled water, and 4 mL of ammonium hydroxide was stirred at room temperature for 10 min. Whilst under magnetic stirring 6 mL of TEOS was then added slowly to the solution which was then stirred for a further 1 h. Solution B containing 10 mL of ethanol, 20 mL distilled water, 3 mL of ammonium hydroxide, and 1 g of CTAB was also stirred at room temperature to produce m-SiO_2. Solution A and B were then mixed and stirred for 30 min after which 2 mL of TEOS was added, and the resulting solution

was stirred for 6 h and then centrifuged. The oven-dried SiO_2@m-SiO_2 product was then dispersed in 100 ml of 0.6 M sodium carbonate (Na_2CO_3) and stirred at 80 ºC for 1 h to selectively etch out some of the solid silica.

Removal of the alkaline solution was done by washing thoroughly with distilled water until the pH was neutral, the product was dried under vacuum at 100 ºC and calcined at 600 ºC for 6 h to remove any unreacted CTAB.

(ii) Carbonization of double-shelled m-SiO_2

This was carried out with the same experimental set-up as stated in section 3.2.2 (iii) with toluene as the carbon source and argon as the carrier gas (**Figure 3.4**).

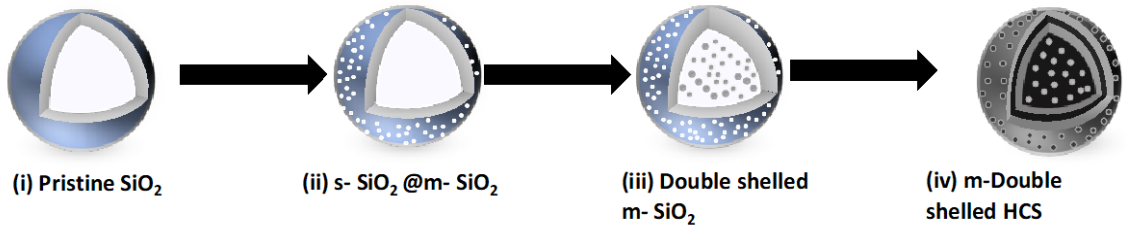


Figure 3.4: Schematic diagram depicting the synthesis of double-shelled mesoporous hollow carbon spheres.

3.2.4 Post-synthesis doping of single-shelled and double-shelled hollow carbon spheres

Both double-shelled and single-shelled carbons were synthesized as described above. Then 4 g were of the synthesized hollow carbon spheres were added to a quartz boat. Post synthesis doping was then carried out in a horizontal chemical vapour deposition (CVD) reactor. The temperature was increased at 10 mL/min until it reached the reaction temperature of 800 ºC. The hollow carbon spheres were doped for 1 h using ammonia gas or acetonitrile as the nitrogen source, with Ar as the carrier gas at a flow rate of 50 mL/min.

3.2.5 Characterization techniques

The thermal stability and decomposition temperature of the crude and annealed hollow carbon spheres (HCSs) were determined by the thermogravimetric analysis (TGA) using a Perkin Elmer Pyris 1 TGA. The procedure involved heating 10 mg of the HCSs from 35 °C to 900 °C

at a heating rate of 10 °C/min under air. Using the Brunner Emmet and Teller (BET) method, the specific surface area of the synthesized silica particles and HCSs was calculated from N_2 adsorption data and the pore size distributions were determined using the Barett-Joyner-Halenda (BJH) method by analyzing the desorption branches of the N_2 isotherms. To determine the surface area a Micromeritics RS232 BET surface analyzer was used. Nitrogen concentrations in the doped and undoped carbon materials were determined by CHN elemental analysis using a Carlo Erba NA 1500 Nitrogen Carbon Sulphur Analyzer. To analyze the morphology and structural properties of both the silica and carbon materials, scanning electron microscopy (SEM) using FEI Nova Nanolab 600 SEM, Raman spectroscopy using a John-Yvon T6400 micron Raman spectrophotometer, and transmission electron microscopy (TEM) using FEI Technai T12 electron microscope were used.

The amount of nitrogen incorporated within carbon layers of the hollow carbon spheres (HCSs) and the nitrogen bonding modes was evaluated using XPS (X-ray photoelectron spectroscopy) analysis. XPS analysis of the obtained samples was done on Thermo Scientific ESCAlab 250Xi using a 300 W Monochromatic Al kα (1486.7 eV) X-ray beam with a diameter of 900 μm. The measurement for the degree of graphitization and structure of the synthesized HCSs was done using Raman spectroscopic analysis, this was carried out using a Jobin-Yvon T6400 micro-Raman spectrometer equipped with a laser excitation wavelength of 514.5 nm and a liquid N_2 cooled charge-coupled device detector. The phase and structure of the as-synthesized carbon materials were determined using the Bruker (D2-205530) diffractometer using secondary graphite monochromated CuKα radiation (λ 1.54184 Å) at 30 kV/30 mA giving the powder X-ray diffraction (PXRD) pattern of the materials.

3.3 Results and discussion

3.3.1 Pristine and mesoporous silica with their respective single-shelled mesoporous hollow carbon spheres

Polydispersed silica spheres were synthesized by the slow addition of TEOS to a solution of water, ethanol, and ammonium hydroxide as the base. This initiated the hydrolysis reaction between the TEOS molecules and water. The silicon alkoxide addition was done slowly and thus different nucleation processes occurred resulting in the formation of polydispersed silica particles [35]. The dispersity of the as-synthesized silica particles is shown in the TEM micrographs and the particle size distributions graphs in **Figure 3.5**. The SEM and TEM

micrographs show the spherical morphology of the silica particles and from the particle size distribution graphs, the average particle size was found to be ca. 360 nm.

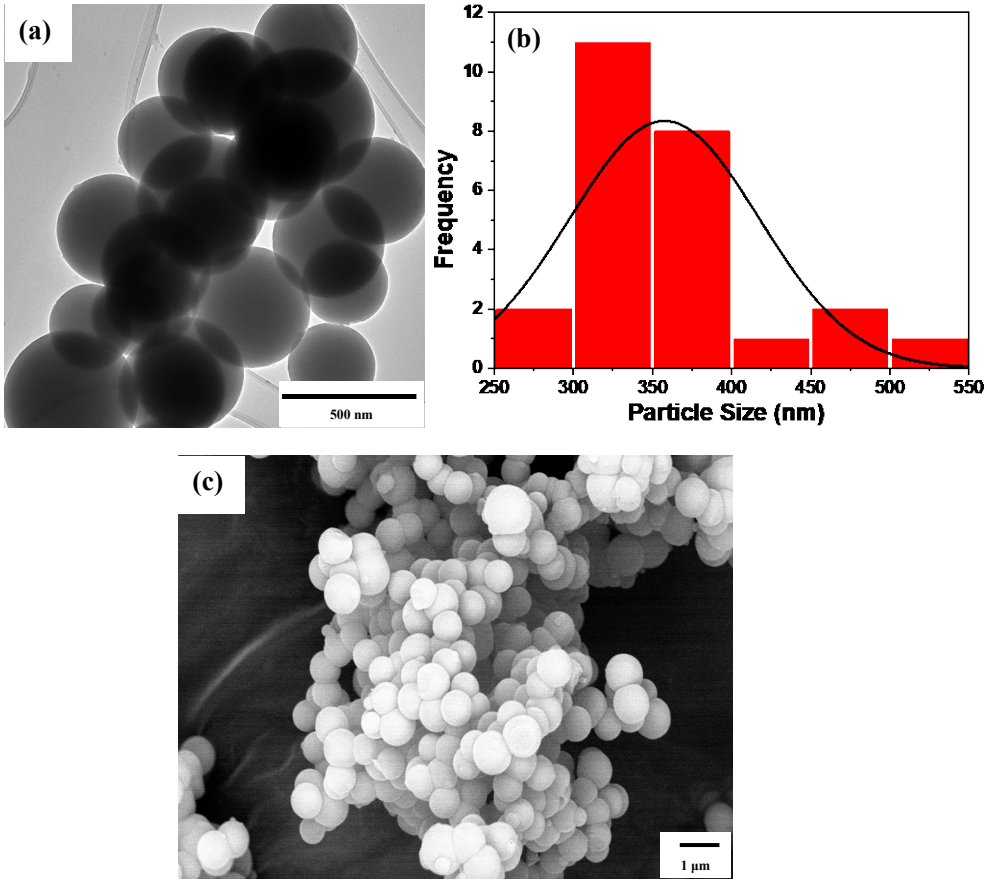


Figure 3.5: Pristine silica (a) TEM micrograph, (b) particle size distribution (extracted from a low magnification image) and (c) SEM micrograph.

The TEM micrographs of the pristine **Figure 3.5a** and mesoporous **Figure 3.6a** silica showed that the spherical morphology was preserved and that the pristine silica has a smooth outer surface whereas the mesoporous silica exhibited a rougher surface and a thick spherical mesoporous outer shell. The average shell thickness (**Figure 3.6a)** of the mesoporous silica layer was found to be 60 nm.

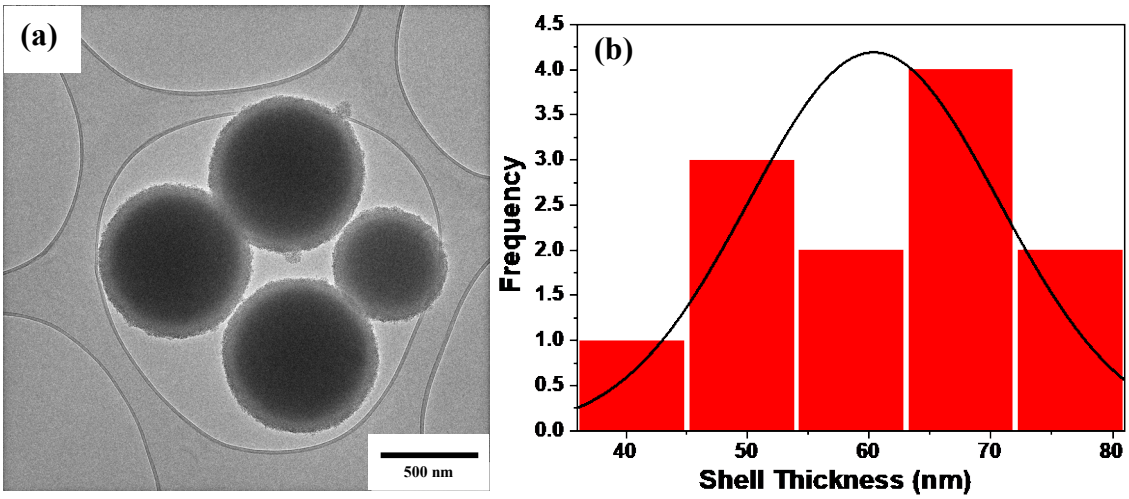


Figure 3.6: (a) TEM micrographs of mesoporous silica micrographs and (b) particle size distribution (extracted from a low magnification image).

The N_2 adsorption-desorption isotherm data obtained showed that pristine silica has a type (III) adsorption isotherm **Figure 3.7** according to the IUPAC report [36]. This suggests that the material has a non-porous surface. This is corroborated by the data shown in **Table 3.1** as the pristine silica has a low surface area and pore volume suggesting that it is non-porous or macroporous. Mesoporous silica adsorption isotherm also in **Figure 3.7** shows a type (I)b isotherm because of the steep uptake at low P/P_o (0.37) due to enhanced adsorbent-adsorptive interactions in the micropores, type (I) isotherms are found in conjunction with materials that have pore size distributions over a broad range, with narrow mesopores and wider micropores. Furthermore, in **Table 3.1** the mesoporous silica was found to have a high surface area and pore volume also confirming that the surface of the material has a porous nature.

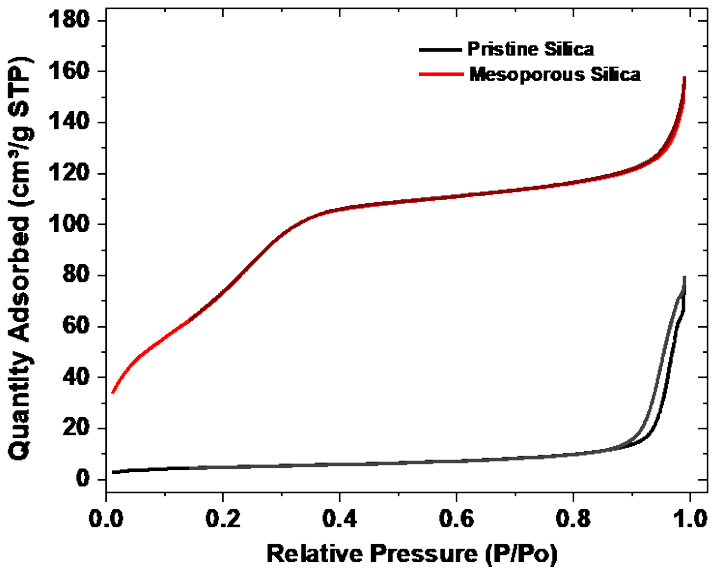


Figure 3.7: BET surface area analysis of pristine and mesoporous silica spheres.

Table 3.1: Pore volumes, BET surface areas and pore sizes of pristine, and mesoporous silica spheres.

Sample	BET surface area (m^2g^{-1})	Pore Volume (cm^3/g)	Pore Size (nm)
Pristine Silica	16.8	0.12	28
Mesoporous Silica	296	0.27	2.4

The morphologies of the hollow carbon spheres synthesized from the two types of silica were analyzed using TEM. The hollow carbon spheres obtained were not deformed owing to the rigidity of the spherically shaped silica. The resulting HCSs carbonized using pristine silica as a template, exhibited a very smooth thin shell with an average shell thickness of 21 nm when toluene was used as the carbon precursor. When acetylene was used as the carbon source, a bubble-like outer shell with a thickness of 10 nm was observed. During the carbonization process, the carbon atoms are adsorbed onto the surface of the silica spheres and due to the low surface area and pore volume of the pristine silica spheres, the surface becomes oversaturated resulting in the formation of a thin carbon shell. The small shell thickness can also be attributed to the long carbonization time as carbon atoms may start to be removed from the external area of the shell with an increase in CVD time, therefore decreasing the shell thickness [37]. Some of the disadvantages of thin shells are that upon further pyrolysis during the annealing or post doping process, the shells can become thinner resulting in deformation or breakage during

further processing thereby destroying its spherical morphology. The differences in shell thickness can be attributed to the different carbon sources used this is observed in the TEM micrographs **Figure 3.8(a) and Figure 3.9(a)** show that the acetylene gives a carbon morphology described as bubble-like.

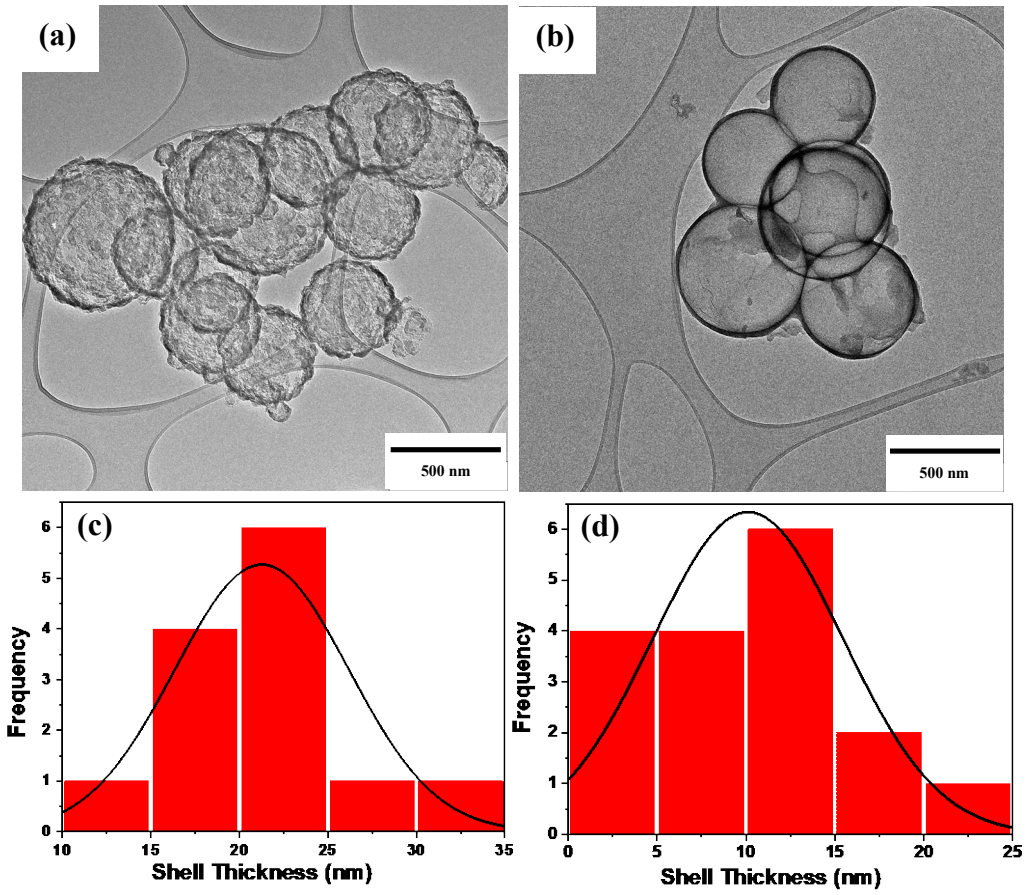


Figure 3.8: TEM micrographs of hollow carbon spheres synthesized from pristine silica with different carbon sources (a) acetylene, (b) toluene and their respective particle size distributions (c) and (d).

Carbonization of mesoporous silica is expected to produce hollow carbon spheres with thicker shells compared to pristine silica templated HCSs. This is due to the mesoporous channels on the silica, these get blocked by carbon atoms as the carbon precursor flows through the reactor. Upon removal of the silica template, the mesochannels remain on the carbon replica, and this suggests that the shell thickness of the mesoporous layer on the silica can influence the thickness of the resulting HCSs. The shell thickness of the acetylene mesoporous HCSs was found to be 46 nm and 49 nm for toluene. This difference in thickness is also shown in SEM

micrographs **Figure 3.9(e) and (f)**. The SEM micrographs in **Figure 3.9 (e-f)** show a bubbly surface which can be attributed to the mesoporous nature of the hollow carbon spheres.

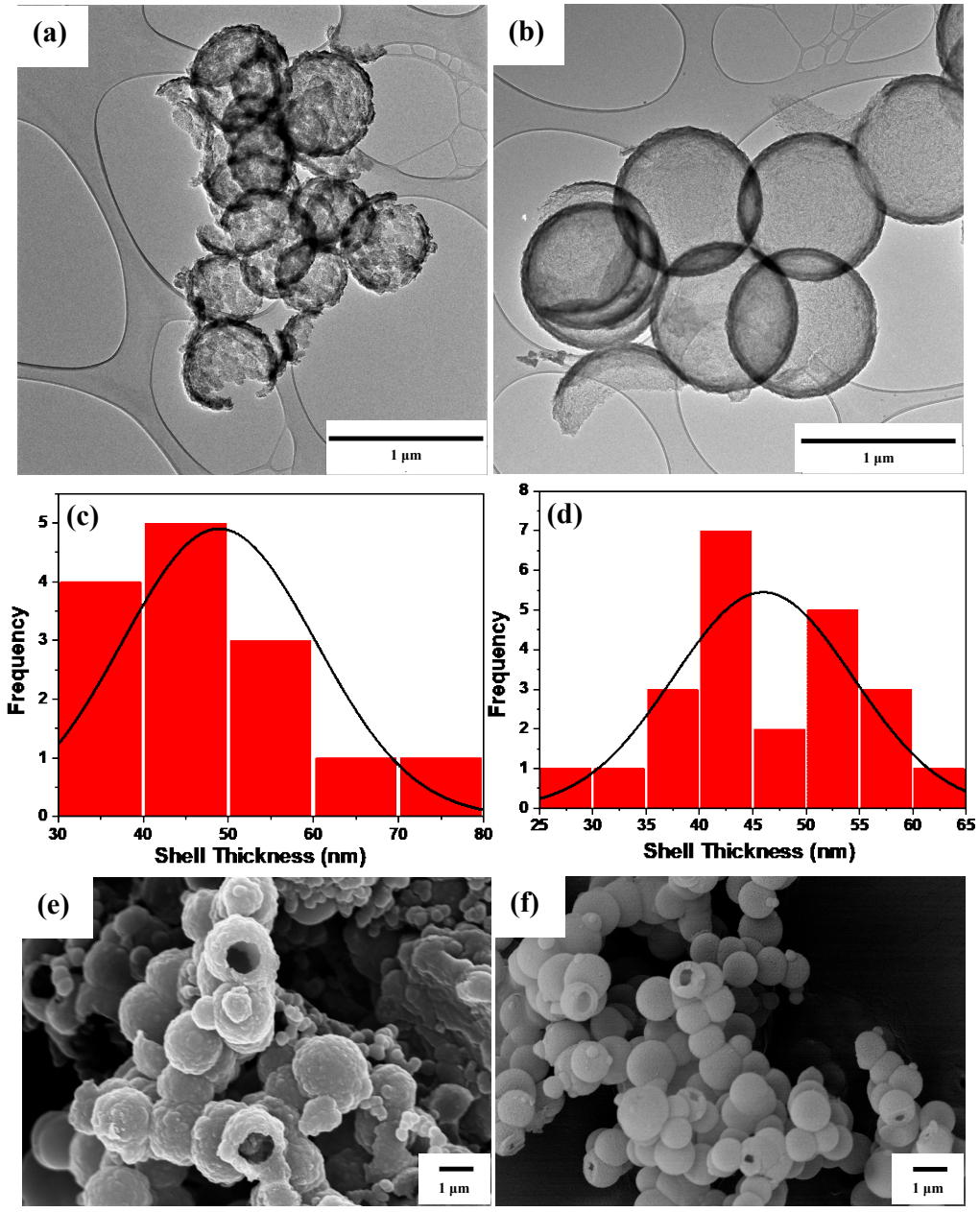


Figure 3.9: TEM micrographs of hollow carbon spheres synthesized from pristine silica with different carbon sources (a) acetylene, (b) toluene, their respective particle size distributions (c) and (d) and SEM micrographs (e) acetylene, (f) toluene.

N_2 adsorption-desorption isotherm data obtained shows that mesoporous silica carbonized with acetylene has a type (III) adsorption isotherm whereas toluene mesoporous HCSs showed a type (I) adsorption isotherm suggesting that they possess better mesoporous characteristics this is corroborated by the BET data shown in **Table 3.2**, therefore, toluene penetrates better

through the mesochannels. Furthermore, acetylene gas is thermodynamically less stable compared to other carbon sources therefore toluene carbon source was chosen to be the better carbonizing source in this research.

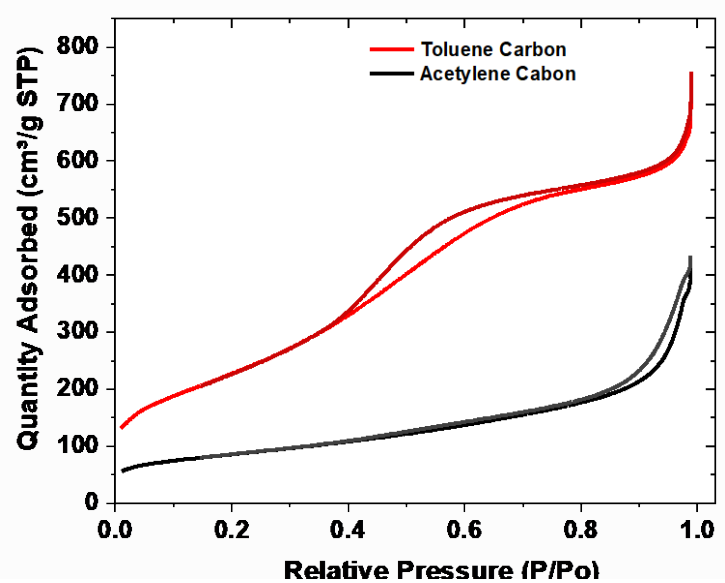


Figure 3.10: BET surface area analysis of mesoporous hollow carbon spheres carbonized by toluene (red) and acetylene (black).

Table 3.2: Pore volumes, BET surface areas, and pore sizes of mesoporous hollow carbon spheres.

Sample	BET surface area (m^2g^{-1})	Pore Volume (cm^3/g)	Pore Size (nm)
Toluene Carbon	823	0.89	0.4
Acetylene Carbon	106	0.21	8.6

3.3.2 Double-shelled mesoporous silica and its hollow carbon spheres in comparison with single-shelled mesoporous hollow carbon spheres

3.3.2.1 Morphology analysis of double-shelled silica templates and their respective hollow carbon spheres

The silica template was characterized using TEM. The SiO_2@m-SiO_2 particle size was found to have an average particle size of 750 nm and after selective etching, polydispersed templates were observed with an average particle size of 727 nm. The slight size reduction could be due

to etching or disintegration of surface carbon layers due to heating. In **Figure 3.11(a)** the TEM micrographs show a darker core particle and a lighter outer edge this confirms that SiO_2@m-SiO_2 was successfully synthesized. The core particle is made up of silica spheres (SiO_2) and the outer shell has a mesoporous layer (m-SiO_2). The double-sided mesoporous shells are shown in **Figure 3.11(b)** and were found to have an average shell thickness of 73 nm, their carbonization should occur on both the inside and outside of the template which when etched out with HF will result in the formation of double-shelled mesoporous hollow carbon spheres (DS-mHCS).

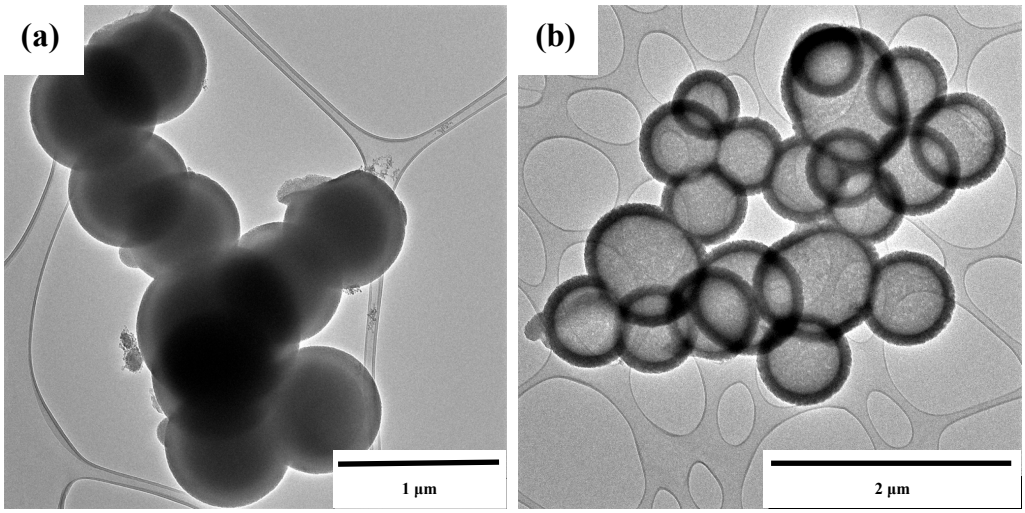


Figure 3.11: TEM micrographs of (a) SiO_2@m- SiO_2, (b) double-shelled m-SiO_2.

The resulting double-shelled mesoporous hollow carbon spheres **Figure 3.12(a-e)** were found to have an average inner particle size of 545 nm and outer particle size of 726 nm, the average spacing between the two shells was found to be an average of 72 nm similar to the silica template shell thickness shown in **Figure 3.11(b)**. The SEM micrograph in **Figure 3.12(f)** shows a definition between the inner and outer shell, and, the bubbled surface morphology and this can be attributed to the mesoporous nature of the hollow carbon spheres. Complete, broken, and partially formed carbon shells are observed in the TEM and SEM micrographs. The broken, and partially formed carbon shells can be ascribed to an incomplete coating of the silica spheres due to the short carbonization time. The resulting thin or incomplete shells could have been broken during the etching process.

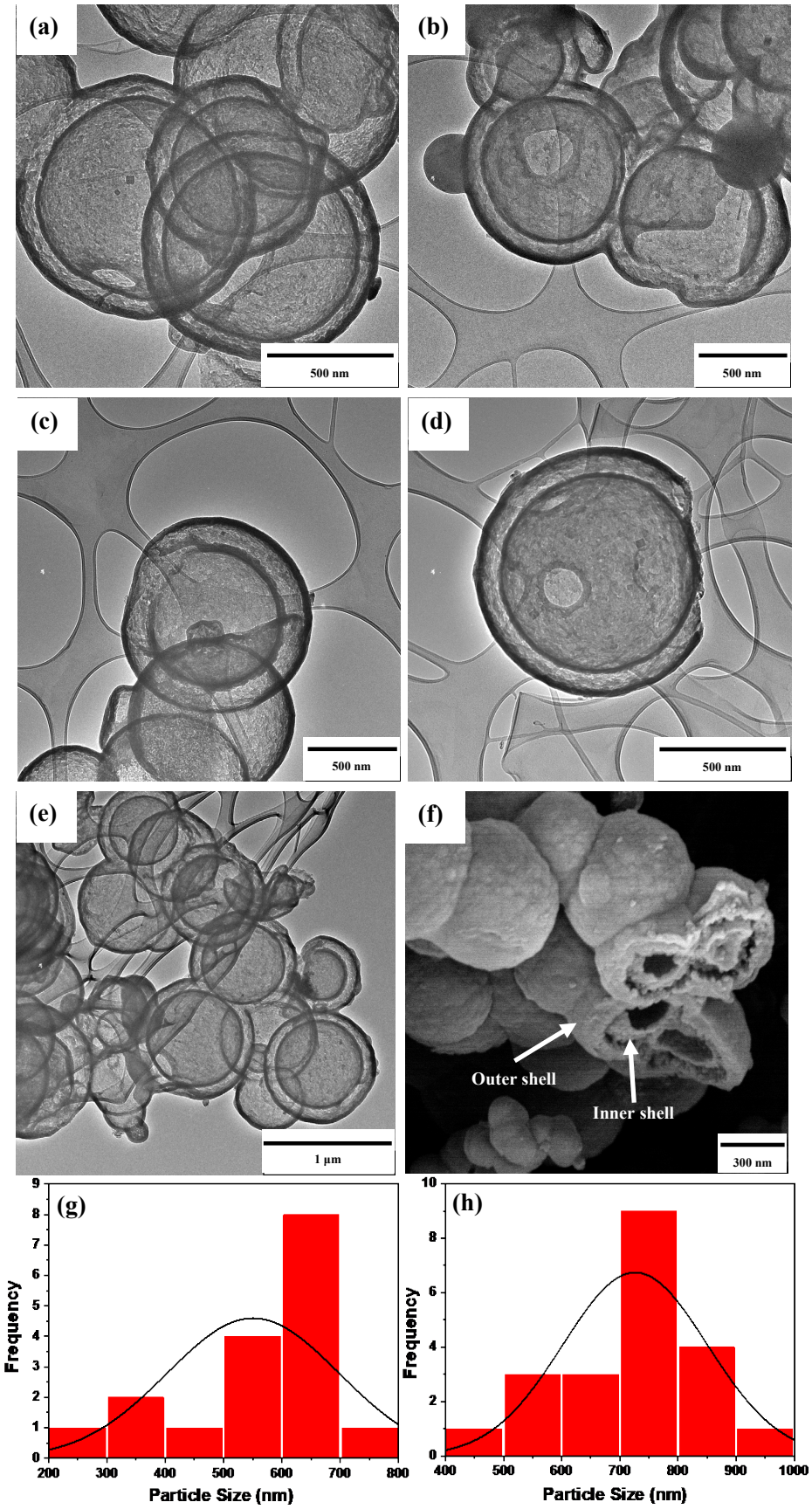


Figure 3.12: Double-shell mesoporous hollow carbon spheres micrographs (a-e) TEM, (f) SEM, and (g-h) the particle size.

3.3.2.2 Structural analysis of double-shelled and single-shelled hollow carbon spheres

The powder X-ray diffraction (PXRD) patterns both show a strong (002) plane peak at 2θ = 25° indicating that a well-ordered structure was formed. The (002) peaks are found to be broad, this can be ascribed to their small crystallite sizes. The difference in peak intensities suggests that the single-shelled carbon is more crystalline whereas the double-shelled is disordered and therefore has low crystallinity. The (101) plane peak at 2θ = 43° also corresponds to the graphitic nature of the hollow carbon spheres [38].

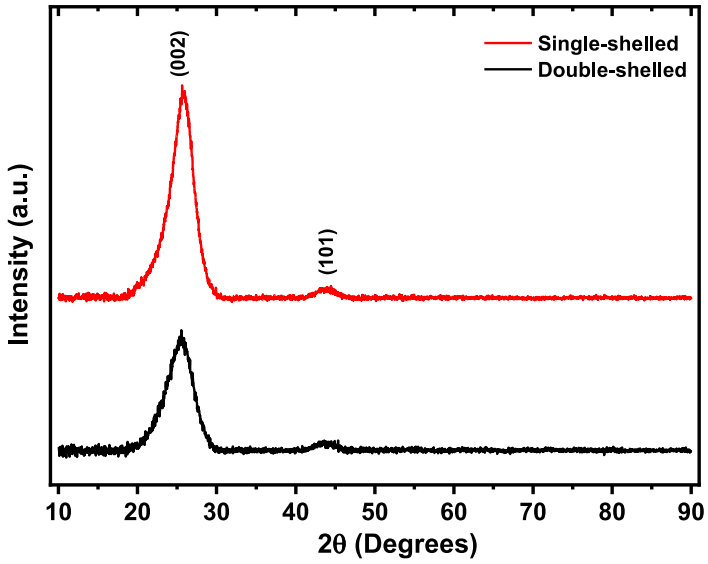


Figure 3.13: Powder X-ray diffraction patterns of single and double-shelled mesoporous hollow carbon spheres.

3.3.2.3 Raman analysis of single-shelled and double-shelled hollow carbon spheres

Bonding order and the structural characteristics of the synthesized materials were studied using Raman spectroscopy, the peaks located at 1342 cm $^{-1}$ and 1334 cm^{-1} are related to the D band which is associated with the sp^3 vibrations of carbon atoms with dangling bonds in the plane of disordered carbon. The G band peaks at 1593 cm $^{-1}$ and 1601 cm^{-1} are due to the plane vibrations of sp^2 bonded carbon atoms and the E_{2g} mode of the graphitic material, the positions of these band peaks suggest that the synthesized hollow carbon spheres have some graphitic nature [39]. The intensity ratios of the D and G peaks relate to the sp^3/sp^2 carbon ratio, and these are used to measure the degree of disorder that is present in different materials. The presence of the D band indicates that the material is defective, the G band represents the level of graphitization and both the D and G represent sp^2 vibrations of bonded carbon atoms.

The lower the ratio, the higher the degree of graphitization suggesting that there are more sp^2 bonds present, and the higher the ratio the more defective the material is therefore there are more sp^3 bonds [40]. Both I_D/I_G ratios in **Table 3.3** are above 1 therefore defect densities are present in both carbon materials and can likely be attributed to their high porous nature [19]. Since the single-shelled HCSs have a lower ratio this suggests that they are slightly more graphitic in comparison to the double-shelled HCSs which were found to be more disordered, this is consistent with the PXRD data **Figure 3.13**.

Table 3.3: The I_D/I_G ratios of single and double-shelled mesoporous hollow carbon spheres.

Sample	D-band position (cm^{-1})	G-band position (cm^{-1})	I_D/I_G ratio
Single-shelled	1342	1593	1.34
Double-shelled	1334	1601	1.36

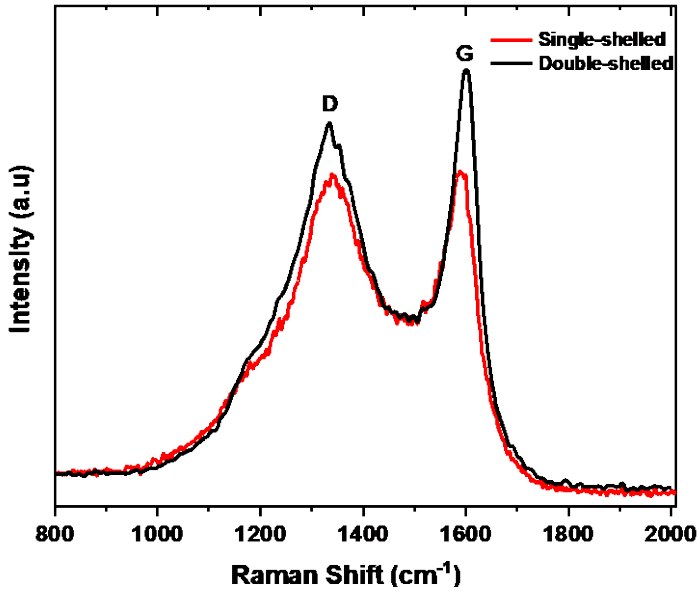


Figure 3.14: Raman spectra of single and double-shelled mesoporous hollow carbon spheres.

3.3.2.4 Thermal stability and purity analysis of single and double-shelled mesoporous hollow carbon spheres

Analysis of the thermal stability of annealed and un-annealed hollow carbon spheres was carried out using thermal gravimetric analysis (TGA). The TGA profiles of the crude single

and double-shelled HCSs showed a three-step process. The single-shelled (SS) carbon started decomposing at 67 ºC but steadily maintained its percentage weight above 90 %, then a more rapid weight loss began at 489 ºC until most of the carbon is burnt off to 0.8 % at 819 ºC. A similar pattern occurred with the double-shelled (DS) carbon with an initial decomposition at 185 ºC and a moderate weight loss beginning at 513 ºC until a 6 % residual is left at 900 ºC, the residual could be due to some of the SiO_2 template not being etched out completely or the presence of unburnt carbon. From the differential temperature gradient (DTG) profiles of both materials, the degree of graphitization and presence of defects can be studied. The onset weight losses are observed on each of the DTG profiles with the first small decomposition peaks of 103 ºC (single-shelled) and 203 ºC (double-shelled) which can be attributed to the burning of amorphous carbon or oxidation of carbon-to-carbon dioxide. The second trough for the DS is seen at 714 ºC which could be due to the decomposition of graphitic carbon, due to the burning of the graphitic layer of the first shell and the amorphous layer of the second shell, the third trough was observed at 837 ºC which could be due to the graphitic flakes of the second shell. The second trough observed for the SS carbon and is due to the graphitic carbon [41].

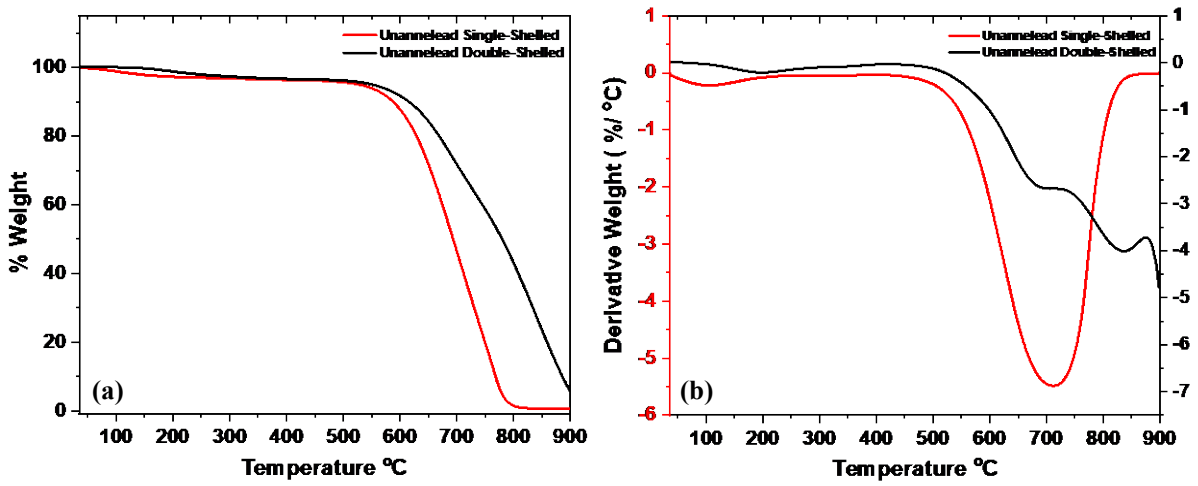


Figure 3.15: (a) Thermograms and (b) corresponding derivative profiles of unannealed single and double-shelled mesoporous hollow carbon spheres.

The TGA profiles of the annealed SS and DS carbon both showed weight maintenance at 100 % until the onset combustion at 528 ºC (SS) and 520 ºC (DS). Complete decomposition to 0 % occurred at 795 ºC for the single-shelled carbon and its DTG profile showed a sharper single decomposition trough at 670 ºC which corresponds to a more pure and uniform carbon material [26]. Gradual decomposition occurred for the DS carbon until 900 ºC was reached and a 3 % residual was left, the DS DTG profile showed two decomposition troughs with the first being

attributed to the amorphous nature of the carbon owing to the sp^3 hybridized carbons and the second due to the combustion of graphitic carbon. Another reason for the two decomposition troughs present could be attributed to the multi-layer nature of the material as the outer layer combusts first followed by the inner layer. Thermal stability of single-shelled carbon increased from 489 ºC to 528 ºC, this was due to the annealing of the carbon material which was done to produce purer HCSs. For the double-shelled carbon, a slight decrease in thermal stability was noted which could be due to the introduction of more defects in the carbon framework [42]. This was further corroborated by the Raman data as the DS carbon material was also found to contain more defects compared to the SS carbon. Given that both the TGA and DTG profiles of the DS carbon materials did not reach endset temperatures it can be proposed that the complete combustion temperatures were not reached due to the parameters used therefore a final temperature greater than 900 ºC could be implemented to give a broader overview.

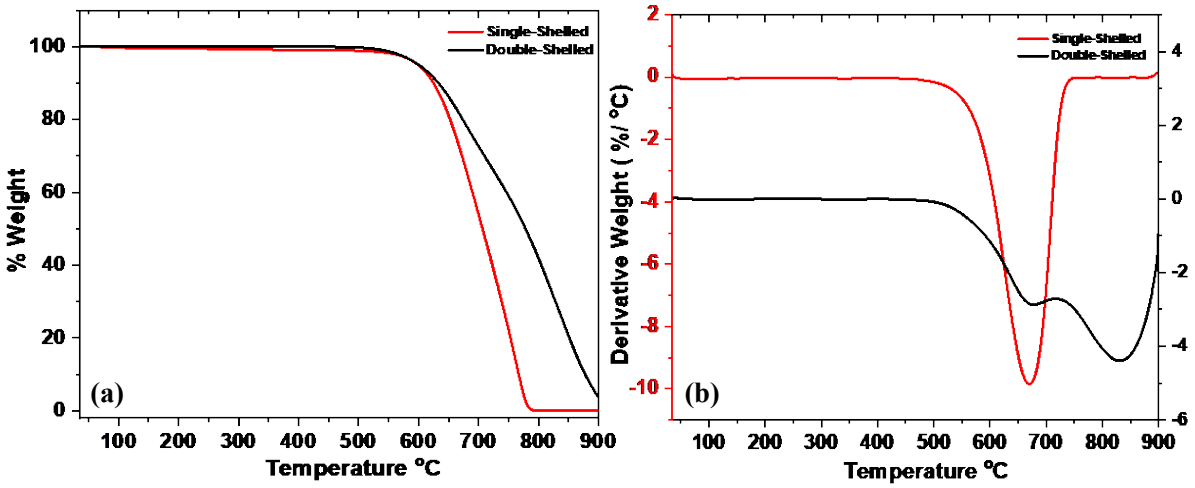


Figure 3.16: a) Thermograms and (b) corresponding derivative profiles of annealed single and double-shelled mesoporous hollow carbon spheres.

3.3.3 Properties of double-shelled and single-shelled mesoporous hollow carbon spheres after nitrogen doping.

3.3.3.1 BET surface area analysis of N-doped doped single and double-shelled mesoporous hollow carbon spheres

The main aim of annealing and doping the as-synthesized hollow carbon spheres was to improve the materials' surface area and electrocatalytic activity. The data in **Table 3.4** shows that improvements on the surface area were made after annealing and doping. There was an

increase in surface area for each of the materials after annealing, the single-shelled HCSs surface area increased from 822 m^2g^{-1} to 832 m^2g^{-1}, and the double-shelled HCSs from 4.6 m^2g^{-1} to 17 m^2g^{-1}. Doping the materials also resulted in surface area increases. This observation has been made by other researchers such as Ganesan *et al*. who found that post doping by heat treatment of ordered carbon materials with nitrogen increased the specific surface area of the porous carbon [43].

Using ammonia as a nitrogen source resulted in an increase of the surface area for both the carbon materials. When acetonitrile was used as the nitrogen source the surface areas increased but not as significantly as when ammonia was used and this suggests that ammonia is the better nitrogen dopant. The reason for this could be attributed to the pyrolysis of acetonitrile at high temperatures during the post doping reaction. Acetonitrile breaks down to give hydrogen cyanide (HCN) and other free radicals. Hydrogen cyanide then further decomposes to give nitrogen that is incorporated in the carbon framework [44], [45]. This long process could have resulted in less doping, therefore, resulting in less nitrogen incorporation and a lower surface area [26]. Metcalfe *et al.* also found that at temperatures lower than 1000 ºC, a reduced yield of HCN is produced due to nitrogen-containing polymeric residue also being produced [46]. From the N_2 adsorption-desorption isotherm shown in **Figure 3.17**, only the single-shelled ammonia doped hollow carbon spheres exhibited a type (I) adsorption isotherm suggesting that it possessed mesoporous characteristics. This is confirmed further with the data in **Table 3.4** which shows that the material has the highest surface area among the nitrogen doped materials.

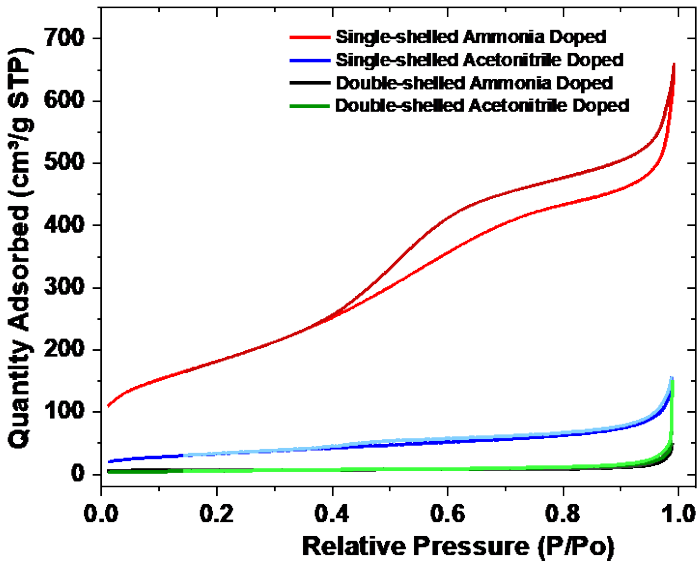


Figure 3.17: BET surface area analysis of nitrogen-doped mesoporous hollow carbon spheres.

Table 3.4: Pore volumes, BET surface areas, and pore sizes of single and double-shelled mesoporous hollow carbon spheres.

Sample	BET surface area (m^2g^{-1})	Pore Volume (cm^3/g)	Pore Size (nm)
Single-shelled unannealed	823	0.89	0.4
Single-shelled	832	1.12	4.3
Single-shelled ammonia doped	656	0.31	6.3
Single-shelled acetonitrile doped	117	0.23	7.7
Double-shelled unannealed	4.6	0.11	90.8
Double-Shelled	17	0.17	39.1
Double-shelled ammonia doped	23	0.07	11.7
Double-shelled acetonitrile doped	21	0.18	35.5

3.3.3.2 Elemental analysis of doped single and double-shelled mesoporous hollow carbon spheres

To quantify the total carbon and nitrogen content of the doped carbon materials, CHNS elemental analysis was used. From the data in **Table 3.5**, all the nitrogen-doped materials showed that nitrogen is present; however, the single-shelled hollow carbon spheres were found to have higher nitrogen content. The low nitrogen content in double-shelled hollow carbon spheres might be due to the lower surface area found in the DS materials (**Table 3.4**) given the lower number of active sites for carbon to react with nitrogen.

Table 3.5: Elemental nitrogen content of doped single and double-shelled mesoporous hollow carbon spheres.

Sample	Elemental Analysis (wt%)		
	Carbon	**Hydrogen**	**Nitrogen**
Single-shelled	93.42	0.36	-
Single-shelled Ammonia Doped	90.31	0.45	1.78
Single-shelled Acetonitrile Doped	90.83	0.27	1.36
Double-Shelled	95.37	1.16	-
Double-Shelled Ammonia Doped	95.52	0.18	0.56
Double-Shelled Acetonitrile Doped	95.18	0.19	0.82

3.3.3.3 Elemental composition analysis of doped single-shelled mesoporous hollow carbon spheres

To analyze the chemical states and surface elements of the as-synthesized mesoporous hollow carbon spheres, XPS was used. The introduction of N atoms into the synthesized material led to a variety of surface N groups that are bonded to the carbon network by either three or two bonds. The N configurations were divided into two peaks located at 398.2 eV and 400.9 eV these were denoted pyrrolic N and pyridinic N species. Pyrrolic N is present where the N atom is connected to two carbons and one hydrogen (H) in a five-membered ring whereas the pyridinic N is denoted when a nitrogen atom has sp^2 hybridization with two carbon atoms [46]. The process of incorporating nitrogen species into carbon materials entails the substitution of some carbon atoms located on the reactive edge with nitrogen atoms from the NH_3 (or CH_3CN) used as the nitrogen precursor. These reactions result in the elimination of some carbon atoms, therefore, increase the surface area and porosity of the material as is corroborated by the BET results (**Table 3.4**) that show an increase in surface area after doping. The higher percentage of N is attributed to the pyridinic N and since good electrocatalytic properties are observed when there is a high atomic concentration of pyridinic and pyrrolic N [47] the presence of these nitrogen atoms in the synthesized material suggests that it would be a useful counter electrode (CE) material.

From the results obtained its appears that the SS mesoporous hollow carbon spheres mainly consisted of carbon (C) at 89.9 %, oxygen (O) at 4 %, and nitrogen (N) at 6 %. Carbon XPS spectra (C1s) was curve-fitted into five individual peaks: C-O at 285.8 eV, C=O at 288 eV, O-C=O at 289.5 eV, and graphitic carbons C-C with sp^2 hybridization at 284.2 eV and; sp^3 hybridized at 285 eV. The O 1s was deconvoluted into two peaks at 531.8 eV (C-O) and 533.2 eV (C=O). These results show that graphitic carbon is present on the surface of the mesoporous SS HCS's with relatively small amounts of CO and COO^- present which could be due to the chemically oxidized carbon materials [48]. Furthermore post doping of carbon materials alters the sp^3/sp^2 ratios and in the doped synthesized material, a higher percentage of sp^2 hybridization is noted which can be attributed to the formation of CN bonds [42].

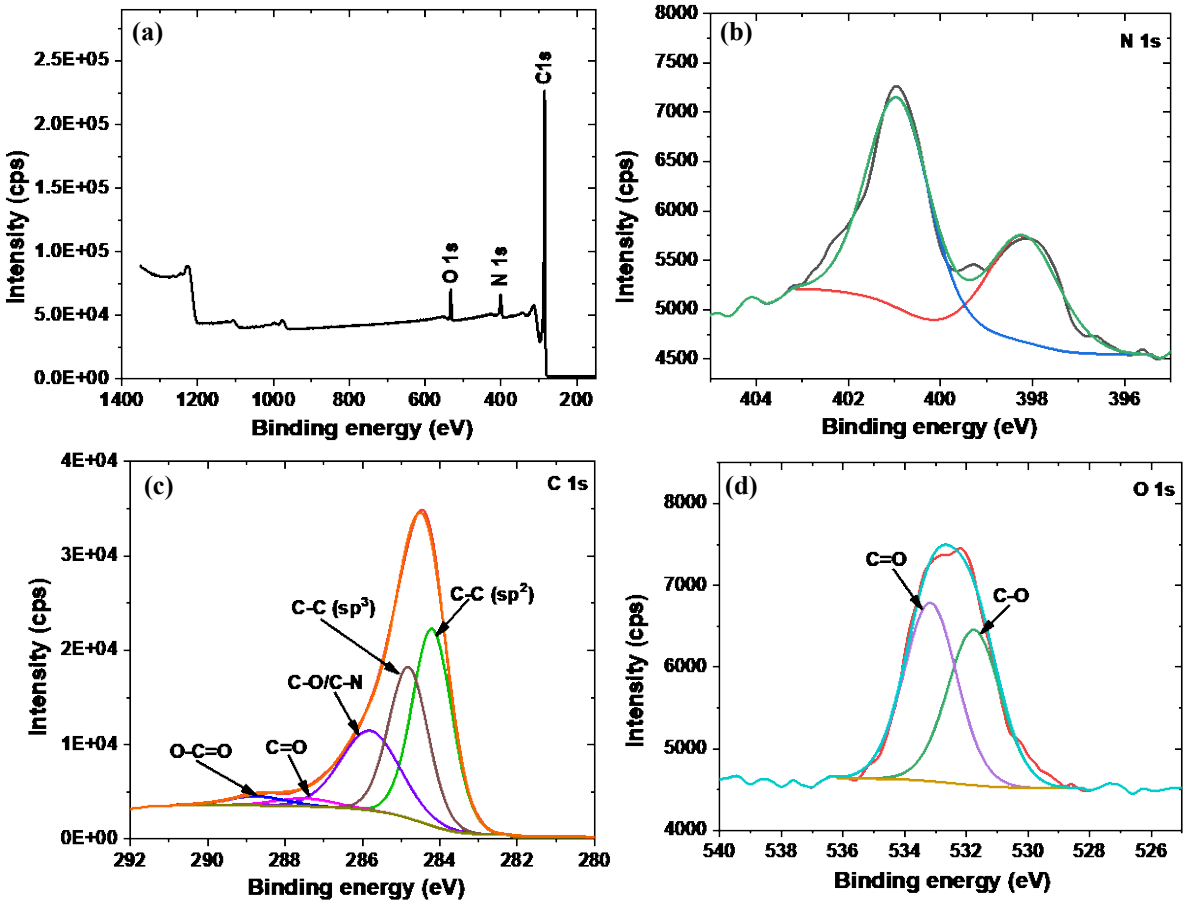


Figure 3.18: (a) XPS survey spectrum of N-doped single-shelled HCS and (b)-(d) high-resolution spectra of nitrogen, carbon, and oxygen, respectively.

Table 3.6: XPS data of N-doped single-shelled mesoporous hollow carbon spheres.

Elements	Atomic %	Peak Binding Energy (eV)	Assignments	Assignment %
C	89.9	284.2	C-C (sp^2)	36.2
		284.8	C-C (sp^3)	27.8
		285.8	C-O	22
		287.5	C=O	2.2
		288.8	O-C=O	2.6
N	6	398.2	Pyrrolic N	1.7
		400.9	Pyridinic N	3.1
O	4	531.8	C-O	2.1
		533.2	C=O	2.4

3.4 Conclusion

From this study, we can conclude that the hard templating method is ideal for the synthesis of hollow carbon spheres as the spherical shape was maintained even when the silica spheres were altered to create a mesoporous layer for the synthesis of mesoporous hollow carbon spheres. The porous nature for the SS carbon was more than that of the DS carbon and this could be due to the pore-forming agent used, suggesting that the C_{18} TMS produces materials with a higher surface area compared to CTAB. The very low surface area of the DS carbon can also be ascribed to the incomplete removal of SiO_2, therefore etching could be carried out for more than 24 h. The presence of SiO_2 in DS is also noted in the TGA data obtained. Toluene was found to be a better carbon source as it was able to better penetrate the mesochannels of the silica templates and produce carbon that had a higher surface area. Given that both the single and double-shelled mesoporous hollow carbon spheres were both carbonized with toluene, it was concluded that the single-shelled carbon exhibited better characteristics such as their graphitic nature and high surface area for the occurrence of the electrocatalytic activity. Annealing and post-synthesis nitrogen doping of the synthesized materials enhanced their thermal stability and electrochemical properties. Moreover, the annealed, toluene carbonized single-shelled mesoporous hollow carbon spheres were found to have the best characteristics of a counter electrode material.

References

[1] B. K. Mutuma *et al.*, "Hollow carbon spheres and a hollow carbon sphere/polyvinylpyrrolidone composite as ammonia sensors," *J. Mater. Chem. A*, vol. 5, no. 6, pp. 2539–2549, 2017.

[2] S. Li, A. Pasc, V. Fierro, and A. Celzard, "Hollow carbon spheres, synthesis and applications-a review," *J. Mater. Chem. A*, vol. 4, no. 33, pp. 12686–12713, 2016.

[3] H. Zhang, H. Xu, M. Wu, Y. Zhong, D. Wang, and Z. Jiao, "A soft-hard template approach towards hollow mesoporous silica nanoparticles with rough surfaces for controlled drug delivery and protein adsorption," *J. Mater. Chem. B*, vol. 3, no. 31, pp. 6480–6489, 2015.

[4] Y. Bao, C. Shi, T. Wang, X. Li, and J. Ma, "Recent progress in hollow silica : Template synthesis , morphologies and applications," *Microporous Mesoporous Mater.*, vol. 227, pp. 121–136, 2016.

[5] L. Zhang, L. Jin, B. Liu, and J. He, “Templated growth of crystalline mesoporous materials: From soft/hard templates to colloidal templates,” *Front. Chem.*, vol. 7, no. JAN, pp. 1–13, 2019.

[6] H. Sun, Y. Zhu, B. Yang, Y. Wang, Y. Wu, and J. Du, “Template-free fabrication of nitrogen-doped hollow carbon spheres for high-performance supercapacitors based on a scalable homopolymer vesicle,” *J. Mater. Chem. A*, vol. 4, no. 31, pp. 12088–12097, 2016.

[7] H. Zhang, H. Xu, M. Wu, Y. Zhong, D. Wang, and Z. Jiao, “A soft-hard template approach towards hollow mesoporous silica nanoparticles with rough surfaces for controlled drug delivery and protein adsorption,” *J. Mater. Chem. B*, vol. 3, no. 31, pp. 6480–6489, 2015.

[8] L. P. Singh *et al.*, “Sol-Gel processing of silica nanoparticles and their applications,” *Adv. Colloid Interface Sci.*, vol. 214, pp. 17–37, 2014.

[9] I. A. Rahman and V. Padavettan, “Synthesis of Silica nanoparticles by Sol-Gel: Size-dependent properties, surface modification, and applications in silica-polymer nanocompositesa review,” *J. Nanomater.*, vol. 2012, 2012.

[10] Y. Castro, N. I. Vazquez, and Z. Gonzalez, “Synthesis of mesoporous silica nanoparticles by sol – gel as nanocontainer for future drug delivery applications,” vol. 6, pp. 139–145, 2017.

[11] I. a. M. Ibrahim, a. a. F. Zikry, and M. a. Sharaf, “Preparation of spherical silica nanoparticles: Stober silica,” *J. Am. Sci.*, vol. 6, no. 11, pp. 985–989, 2010.

[12] S. L. Greasley *et al.*, “Controlling particle size in the Stöber process and incorporation of calcium,” *J. Colloid Interface Sci.*, vol. 469, pp. 213–223, 2016.

[13] S. Savic, K. Vojisavljevic, M. Počuča-Nešić, K. Zivojevic, M. Mladenovic, and N. Knezevic, “Hard Template Synthesis of Nanomaterials Based on Mesoporous Silica,” *Metall. Mater. Eng.*, vol. 24, no. 4, 2018.

[14] X. Deng, K. Chen, and H. Tüysüz, “Protocol for the Nanocasting Method: Preparation of Ordered Mesoporous Metal Oxides,” *Chem. Mater.*, vol. 29, no. 1, pp. 40–52, 2017.

[15] Q. Yue, J. Sun, Y. Kang, and Y. Deng, “Advances in the Interfacial Assembly of Mesoporous Silica on Magnetite Particles,” *Angew. Chemie - Int. Ed.*, vol. 59, no. 37, pp. 15804–15817, 2020.

[16] W. Stöber, A. Fink, and E. Bohn, “Controlled growth of monodisperse silica spheres in the micron size range,” *J. Colloid Interface Sci.*, vol. 26, no. 1, pp. 62–69, 1968.

[17] G. Wang, W. Xing, and S. Zhuo, “Application of mesoporous carbon to counter

electrode for dye-sensitized solar cells," *J. Power Sources*, vol. 194, no. 1, pp. 568–573, 2009.

[18] Y. Xie, D. Kocaefe, C. Chen, and Y. Kocaefe, "Review of Research on Template Methods in Preparation of Nanomaterials," *J. Nanomater.*, vol. 2016, pp. 1–10, 2016.

[19] X. Chen *et al.*, "CVD generated mesoporous hollow carbon spheres as supercapacitors," *Colloids Surfaces A Physicochem. Eng. Asp.*, vol. 396, pp. 246–250, 2012.

[20] J. B. Xu and T. S. Zhao, "Mesoporous carbon with uniquely combined electrochemical and mass transport characteristics for polymer electrolyte membrane fuel cells," *RSC Adv.*, vol. 3, no. 1, pp. 16–24, 2013.

[21] G. Wang, W. Xing, and S. Zhuo, "Application of mesoporous carbon to counter electrode for dye-sensitized solar cells," vol. 194, pp. 568–573, 2009.

[22] E. Ramasamy, J. Chun, and J. Lee, "Soft-template synthesized ordered mesoporous carbon counter electrodes for dye-sensitized solar cells," *Carbon N. Y.*, vol. 48, no. 15, pp. 4563–4565, 2010.

[23] X. Chen *et al.*, "Synthesis , Growth Mechanism , and Electrochemical Properties of Hollow Mesoporous Carbon Spheres with Controlled Diameter," pp. 17717–17724, 2011.

[24] R. Andrews, D. Jacques, D. Qian, and E. C. Dickey, "Purification and structural annealing of multiwalled carbon nanotubes at graphitization temperatures," *Carbon N. Y.*, vol. 39, no. 11, pp. 1681–1687, 2001.

[25] X. Xing, G. Zhang, M. Dell'Amico, G. Ciezki, Q. Meng, and O. Ostrovski, "Effect of annealing on properties of carbonaceous materials. Part II: Porosity and pore geometry," *Metall. Mater. Trans. B Process Metall. Mater. Process. Sci.*, vol. 44, no. 4, pp. 862–869, 2013.

[26] B. K. Mutuma, B. J. Matsoso, K. Ranganathan, J. M. Keartland, D. Wamwangi, and N. J. Coville, "Generation of radical species in CVD grown pristine and N-doped solid carbon spheres using H2 and Ar as carrier gases," *RSC Adv.*, vol. 7, no. 34, pp. 21187–21195, 2017.

[27] B. K. Mutuma, C. I. Garcia-Martinez, R. C. Dias, B. J. Matsoso, N. J. Coville, and I. A. Hümmelgen, "Nitrogen-doped hollow carbon spheres as chemical vapour sensors," *New J. Chem.*, vol. 43, no. 22, pp. 8418–8427, 2019.

[28] M. Scardamaglia *et al.*, "Spectroscopic observation of oxygen dissociation on nitrogen-doped graphene," *Sci. Rep.*, vol. 7, no. 1, pp. 1–11, 2017.

[29] R. Shibuya, T. Kondo, and J. Nakamura, “Active sites in nitrogen-doped carbon materials for oxygen reduction reaction,” *Carbon-Based Met. Catal. Des. Appl.*, vol. 1–2, no. 6271, pp. 227–249, 2018.

[30] B. J. Matsoso, T. Lerotholi, N. J. Coville, and G. Jones, “Designing Parameters of Surfactant-Free Electrochemical Sensors for Dopamine and Uric Acid on Nitrogen Doped Graphene Films,” *Johnson Matthey Technol. Rev.*, vol. 63, no. 2, pp. 76–88, 2019.

[31] J. Han, G. Xu, B. Ding, J. Pan, H. Dou, and D. R. MacFarlane, “Porous nitrogen-doped hollow carbon spheres derived from polyaniline for high performance supercapacitors,” *J. Mater. Chem. A*, vol. 2, no. 15, pp. 5352–5357, 2014.

[32] J. Xu, F. He, S. Gai, S. Zhang, L. Li, and P. Yang, “Nitrogen-enriched, double-shelled carbon/layered double hydroxide hollow microspheres for excellent electrochemical performance,” *Nanoscale*, vol. 6, no. 18, pp. 10887–10895, 2014.

[33] J. Wang *et al.*, “Double-Shelled Phosphorus and Nitrogen Codoped Carbon Nanospheres as Efficient Polysulfide Mediator for High- Performance Lithium – Sulfur Batteries,” vol. c, 2018.

[34] Y. Han *et al.*, “Unraveling the Growth Mechanism of Silica Particles in the Stöber Method: In Situ Seeded Growth Model,” *Langmuir*, vol. 33, no. 23, pp. 5879–5890, Jun. 2017.

[35] C. K. Dixit, S. Bhakta, A. Kumar, S. L. Suib, and J. F. Rusling, “Fast nucleation for silica nanoparticle synthesis using a sol-gel method,” *Nanoscale*, vol. 8, no. 47, pp. 19662–19667, Dec. 2016.

[36] M. Thommes *et al.*, “Physisorption of gases, with special reference to the evaluation of surface area and pore size distribution (IUPAC Technical Report),” *Pure Appl. Chem.*, vol. 87, no. 9–10, pp. 1051–1069, 2015.

[37] W. Kukułka, K. Wenelska, M. Baca, X. Chen, and E. Mijowska, “From Hollow to Solid Carbon Spheres: Time-Dependent Facile Synthesis,” *Nanomaterials*, vol. 8, no. 10, p. 861, 2018.

[38] X. Chen *et al.*, “Synthesis, growth mechanism, and electrochemical properties of hollow mesoporous carbon spheres with controlled diameter,” *J. Phys. Chem. C*, vol. 115, no. 36, pp. 17717–17724, 2011.

[39] M. Li, Q. Wu, M. Wen, and J. Shi, “A novel route for preparation of hollow carbon nanospheres without introducing template,” *Nanoscale Res. Lett.*, vol. 4, no. 11, pp. 1365–1370, 2009.

[40] M. Noël, “Physical Properties and Structural Stability of Carbon Nanotubes Under Extreme Conditions,” 2014.

[41] J. Toit, “Hollow Carbon Nanospheres : A Structural Integrity Investigation,” 2018.

[42] M. W. Dlamini, T. N. Phaahlamohlaka, D. O. Kumi, R. Forbes, L. L. Jewell, and N. J. Coville, “Post doped nitrogen-decorated hollow carbon spheres as a support for Co Fischer-Tropsch catalysts,” *Catal. Today*, no. December 2018, pp. 0–1, 2019.

[43] G. Liu, X. Li, P. Ganesan, and B. N. Popov, “Development of non-precious metal oxygen-reduction catalysts for PEM fuel cells based on N-doped ordered porous carbon,” *Appl. Catal. B Environ.*, vol. 93, no. 1–2, pp. 156–165, 2009.

[44] A. Lifshitz, A. Moran, and S. Bidani, “Thermal Reactions of Acetonitrile at High Temperatures pyrolysis behind Reflected Shocks,” vol. 19, pp. 61–79, 1987.

[45] P. F. Britt, “Pyrolysis and Combustion of Acetonitrile (CH3CN),” *Energy*, 2002.

[46] E. Metcalfe, D. Booth, H. McAndrew, and W. D. Wooley, “The pyrolysis of organic nitriles,” *Fire Mater.*, vol. 7, no. 4, pp. 185–192, Dec. 1983.

[47] H. Kiuchi *et al.*, “Characterization of nitrogen species incorporated into graphite using low energy nitrogen ion sputtering,” *Phys. Chem. Chem. Phys.*, vol. 18, no. 1, pp. 458–465, 2016.

[48] S. N. Faisal *et al.*, “Pyridinic and graphitic nitrogen-rich graphene for high-performance supercapacitors and metal-free bifunctional electrocatalysts for ORR and OER,” *RSC Adv.*, vol. 7, no. 29, pp. 17950–17958, 2017.

[49] S. Majeed, J. Zhao, L. Zhang, S. Anjum, Z. Liu, and G. Xu, “Synthesis and electrochemical applications of nitrogen-doped carbon nanomaterials,” *Nanotechnol. Rev.*, vol. 2, no. 6, pp. 615–635, 2013.

Chapter 4

Colloidal synthesis and characterization of copper sulfide nanoparticles

4.1 Introduction

Materials with exceptional properties have constantly attracted attention as possible replacements for platinum-group metals (PGM's) and other expensive materials that are currently being used in renewable energy sources. Transition metal chalcogenides (TMCs) and their infinite number of configurations are a part of these materials as they exhibit unique chemical, optical and electronic properties [1], [2] making them great candidates for usage in solar cells, supercapacitors as well as in hydrogen evolution reactions [3]–[5]. Bulk and nanostructured TMCs have been researched due to their stability, indirect bandgaps, and optoelectronic behaviour. However, nanostructures (NSs) have shown stronger edge effects and this is due to the quantum confinement effect which enables their use under solar simulated light beams [6] an example of such nanostructures are metal sulfides. Given that some metal sulfides such as pyrite (FeS_2) and chalcocite (Cu_2S) are cheap and abundant as they can exist as minerals in nature [7], [8] makes them viable substitutes for platinum in solar-harvesting devices. The versatility of copper sulfides ($Cu_{2-x}S$) and their tuneable thermal, optical and electric properties make them important p-type semiconductors [9]. Copper sulfides exist in different forms, from sulfur-rich (CuS) to copper-rich (Cu_2S), however, Cu_2S has a mixture of ionic and electronic copper making it a great candidate for optical materials [7].

Different synthesis pathways can be employed to obtain this group of nanostructured metal chalcogenides, these include the vapour-phase approach, solid phase, liquid phase, and the two-phase approach [10]. Generally, when synthesis aims to produce high-quality nanostructures and have the ability to fine-tune their properties, then the liquid-phase approach is used [10], [11]. The liquid phase approach is branched down into two further categories, the top-down and bottom-up synthetic methods [12] **Figure 4.1**. Top-down synthesis involves the breaking down of bulk material into nanostructures [13]. Bottom-up synthesis on the other hand involves

the decomposition of precursors into monomers and as their concentrations reach supersaturation levels, the monomers are consumed, and the growth of nanostructures begins [14]. Between the two strategies, the bottom-up synthesis shows more promising results as it allows for the synthesis of high-quality semiconducting nanostructures. Organic surfactants enable surface stabilization of the nanostructures to obtain different shapes and sizes [14]. To control the shapes and sizes of the products, different reaction parameters such as the chosen precursors, temperature, reaction time, or surfactant choice and concentrations can be adjusted.

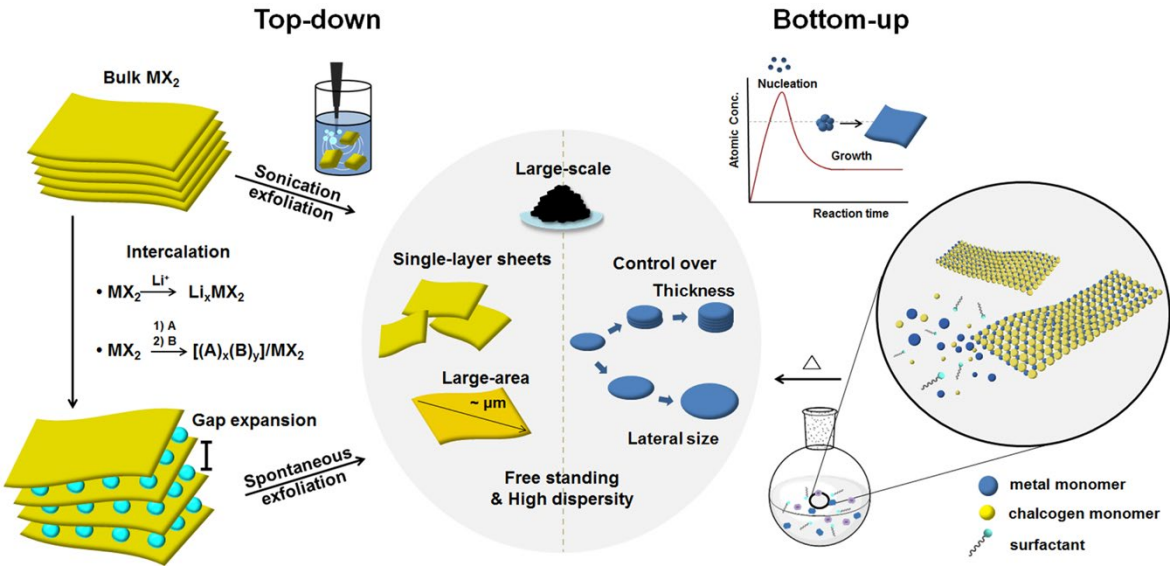


Figure 4.1: Schematic diagram showing the synthesis sequences of the top-down and bottom-up approaches [14].

The bottom-up, one-pot heat-up method can be used in the synthesis of copper sulfide nanoparticles (NPs), this entails mixing the molecular precursors at low temperatures and then heating them to the desired reaction temperature to assist with the nucleation reactions and growth of NPs [15]. Metal chlorides and elemental sulfur are typically used in this method as they are both cost-effective however the use of elemental sulfur produces poor quality metal sulfides [16]. On the other hand 1-dodecanethiol (1-DDT) is a better sulfur precursor due to its controlled decomposition throughout the reaction process [14]. Due to its low toxicity and physicochemical properties 1-dodecanethiol (1-DDT) is one of the preferred sulfur sources, it is made up of a linear hydrocarbon chain and a proton-containing -SH group [17]. The sulfur element in 1-DDT is classified as a soft base S^{2-} and according to the hard, soft acid-base (HSAB) theory, soft bases prefer binding to soft acids resulting in covalent bonding [18].

Depending on the copper precursor used, different shapes and copper sulfide phases are synthesized resulting in alteration of some of the properties of the material [19].
Given that the Cu^{+} cation is classified as a soft acid, then according to the HSAB principle, it will have a strong affinity towards the sulfur anion S^{2-} to produce copper sulfide. One of the many used organic solvents in metal sulfide synthesis is oleylamine ($C_{18}H_{37}N$), this is due to its long linear carbon chain with C=C bonding in the center and an $-NH_3$ group at one end. This allows oleylamine (OLA) to behave as a surfactant, reducing solvent or capping agent during synthesis. The role of oleylamine in this study is to act as a capping agent for colloidal stability [20], [21].

In this research, the copper source was varied to study the changes in morphology and properties of the resulting copper sulfide ($Cu_{2-x}S$) materials. To evaluate the growth mechanism of the synthesized particles a time study was carried out. The particle size of the synthesized nanostructures is also important and this attributes to some of the materials' characteristics and possible uses. For the enhancement of composite reactions and light-harvesting properties, it would be ideal for the particle sizes to be small as this would result in increased surface area for increased interactions and reactivity [22]. Copper chloride (CuCl) and copper acetylacetonate ($Cu(C_5H_7O_2)_2$) were used as copper sources.

4.2 Experimental

4.2.1 Starting materials

Copper(I) chloride (CuCl, ≥98%), copper(II)acetylacetonate ($Cu(acac)_2$, ≥ 99.9%), oleylamine (OLA, 70%), 1-dodecanethiol ($CH_3(CH_2)_{11}SH$, ≥98%), chloroform ($CHCl_3$) and ethanol (EtOH, 96%) were purchase from were purchased from Sigma-Aldrich and there was no further purification.

4.2.2 Colloidal synthesis of Cu_2S

For the synthesis of $Cu_{2-x}S$ nanostructures, 2 mmol of CuCl or 1 mmol of $Cu(acac)_2$ was added to a three-neck round bottom flask, 15 mL of OLA and 5 ml of 1-DDT were added. The flask was connected to a Schleck line, degassed using N_2 for 10 min, and heated under reflux to the reaction temperature of 230 °C whilst stirring for 1 h. During heating, similar changes were observed for both reactions. A colour change was observed, from a clear (CuCl) or a blue

($Cu(acac)_2$) solution to a yellow solution at 120-130 °C. The solution gradually darkened to brown and then black at 210-230 °C this demonstrated the formation of $Cu_{2-x}S$ nanostructures. To give a detailed analysis of the progressing reaction aliquots were taken at the early points in the reaction (10 min). At the middle point of the overall reaction time (30 min) and the end of the reaction (60 min). After the reaction time was reached the solution was naturally cooled and chloroform was added to precipitate the particles. The samples were centrifuged at 8000 rpm for 10 min, washed with ethanol to remove any unreacted precursors, and dried at room temperature.

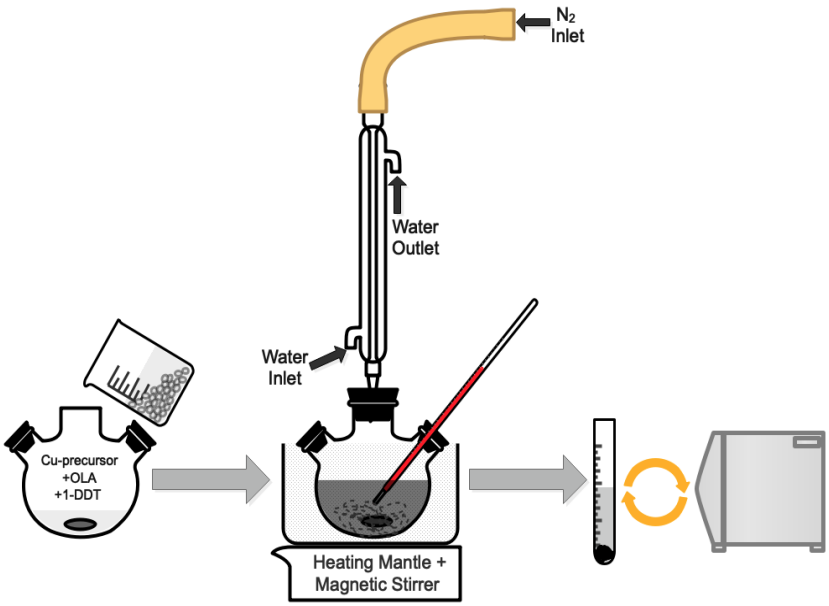


Figure 4.2: Simplified schematic diagram showing the synthesis sequence for $Cu_{2-x}S$ nanoparticles.

4.2.3 Characterization techniques

Morphology of the nanoparticles was analyzed using transition electron microscopy (TEM) performed on FEI Technai T12 TEM microscope carried out at 120 kV acceleration voltage beam spot size of 20-100 nm in TEM mode. Samples dispersed in ethanol, dropped onto the aluminium stubs, and coated twice with gold-palladium were analyzed using scanning electron microscope (SEM) and Energy-dispersive X-ray spectroscopy (EDX) by a FEI Nova Nanolab 600 FIB/SEM equipped with an EDX detector. The structure and phases of the copper sulfide particles were determined using the Bruker (D2-205530) diffractometer using secondary graphite monochromated CuKα radiation (λ 1.54184 Å) at 30 kV/30 mA giving the powder x-ray diffraction (PXRD) pattern of the material. For the absorption measurements, the

synthesized nanoparticles were dissolved in ethanol, poured into quartz cuvettes, and analyzed using the specord 50 AnalytikJena UV-vis spectrophotometer.

4.3 Results and discussion

4.3.1 Nanostructures resulting from Copper (I) chloride Cu-precursor

To study the morphology of the synthesized materials, TEM was used. The changes were observed at different reaction times as depicted in the micrographs below, **Figure 4.3**. At 10 min amorphous cloud-like patches were observed with asymmetrically shaped particles within them **Figure 4.3(c)**. Layered sheets with sharp edges lined with small particles are observed at 30 min exhibiting a change in morphology from the amorphous material at 10 min **Figure 4.3(d)**. When the reaction time was reached the synthesized materials change their shape from semi-defined sheets to thin hexagonal plates with an average particle size of 478.5 nm. The average sizes of the particles were obtained using the TEM micrographs. From the 10 min and 30 min reaction times, the averages sizes could not be obtained due to the aggregation and amorphous qualities of the materials. At 60 min distinct morphology was shown, allowing for the average size to be determined.

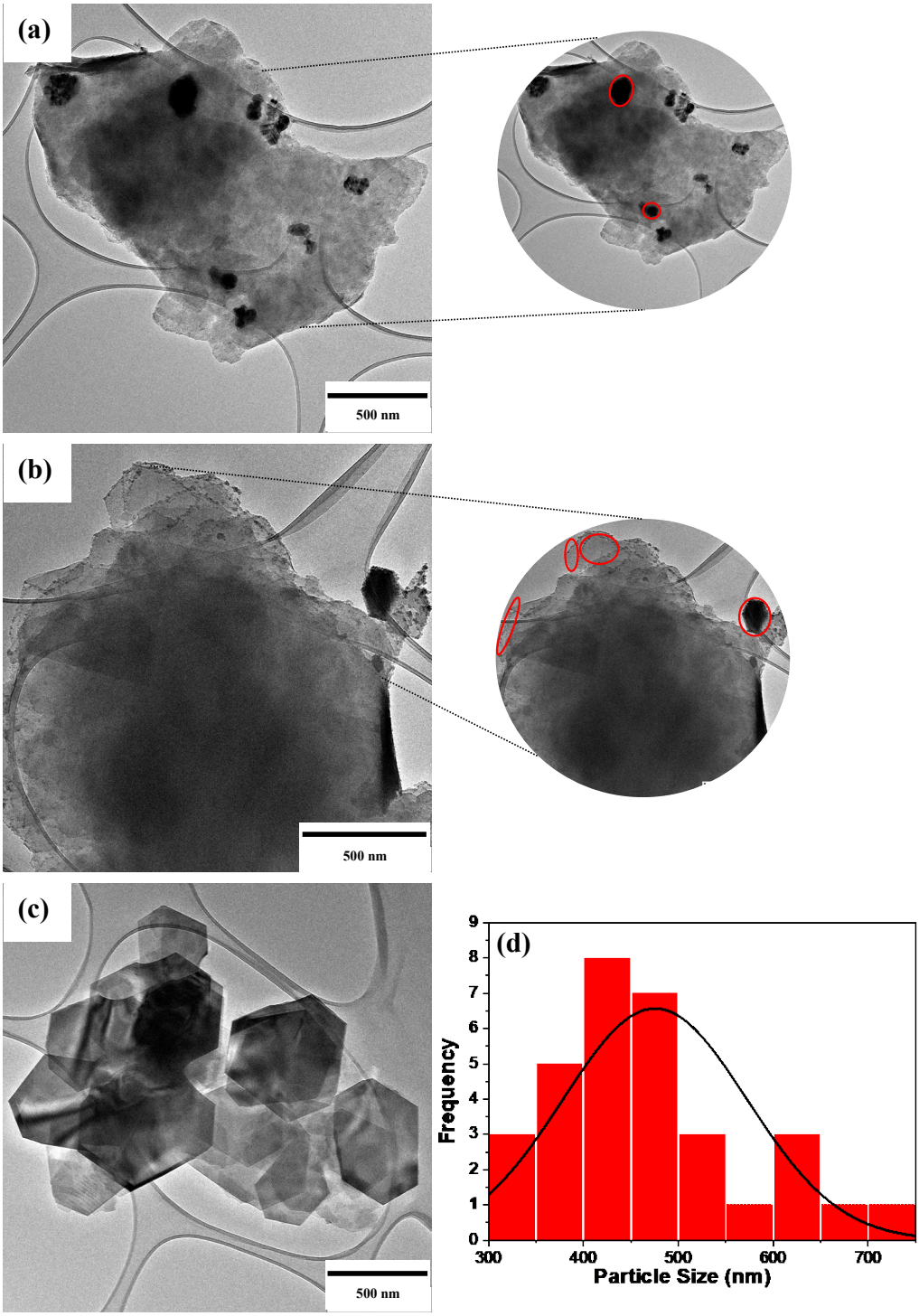


Figure 4.3: Synthesized $Cu_{2-x}S$ TEM micrographs at different reaction times (a) 10 min (b) 30 min, and (c) 60 min. The particle size distribution for the synthesized particles at 60 min reaction time.

The determination of the $Cu_{2-x}S$ phase that was synthesized using CuCl as a copper precursor was done using PXRD. The progression of the experiment, the phase changes, and the formation of the final products were analyzed using the X-ray diffraction obtained at the different reaction times as shown in **Figure 4.3**. At the beginning of the reaction (10 min) multiple peaks can be observed in the 2θ region of 10° - 20° this can be attributed to the crystal planes (040), (050), (060), (070), and (080) which represent the copper-(1-DDT) intermediate. The successive order (0*k*0) where (*k* = 4-8) of the diffraction peaks represents the formation of copper thiolate, $[Cu(SC_{12}H_{25})]$, this intermediate exhibits a layered structure of the Cu and S atoms separated by dodecane chains [17], [23], [24] **Figure 4.4**.

An increase in the relative intensities of the PXRD diffraction peaks suggests a change in crystal morphology [25]. This increase is observed in the 30 min diffraction pattern and can be seen in more detail in Supplementary Fig. S4.1. The peak at 47° increases indicating that there has been preferential growth of some crystal planes during synthesis. At this reaction time, the (060) and (070) peaks are reduced suggesting that some of the copper thiolate intermediates have decomposed. As the reaction progresses and temperature increases, the C-S bonds are cleaved [26] leading to the formation of copper sulfide molecules. This is exhibited by the reduction of the intermediate peaks in both the 30 min and 60min reaction time. At the end of the reaction, the diffraction pattern at 60 min was indexed to cubic digenite (JCPDS 622980) for the $Cu_{1.8}S$ phase of copper sulfide. Peaks denoted (*) in both the 30 min and 60 min reaction time were indexed to the orthorhombic djurleite $Cu_{1.97}S$ (PDF 00-020-0365). Although the peaks at 30 min are less defined suggesting that as the reaction occurred and the intermediate bonds were cleaved, the material became more copper-rich as the crystal grew from a cubic phase to orthorhombic. This is corroborated in the TEM micrographs as edges are formed on the amorphous material and some hexagonal material is also observed. At 60 min the djurleite peaks are more pronounced as there is more crystal growth resulting in a mixed phase material. This is also observed in the TEM micrographs as both thinly shaped hexagonal plates with irregular sides are observed as well as some amorphous material.

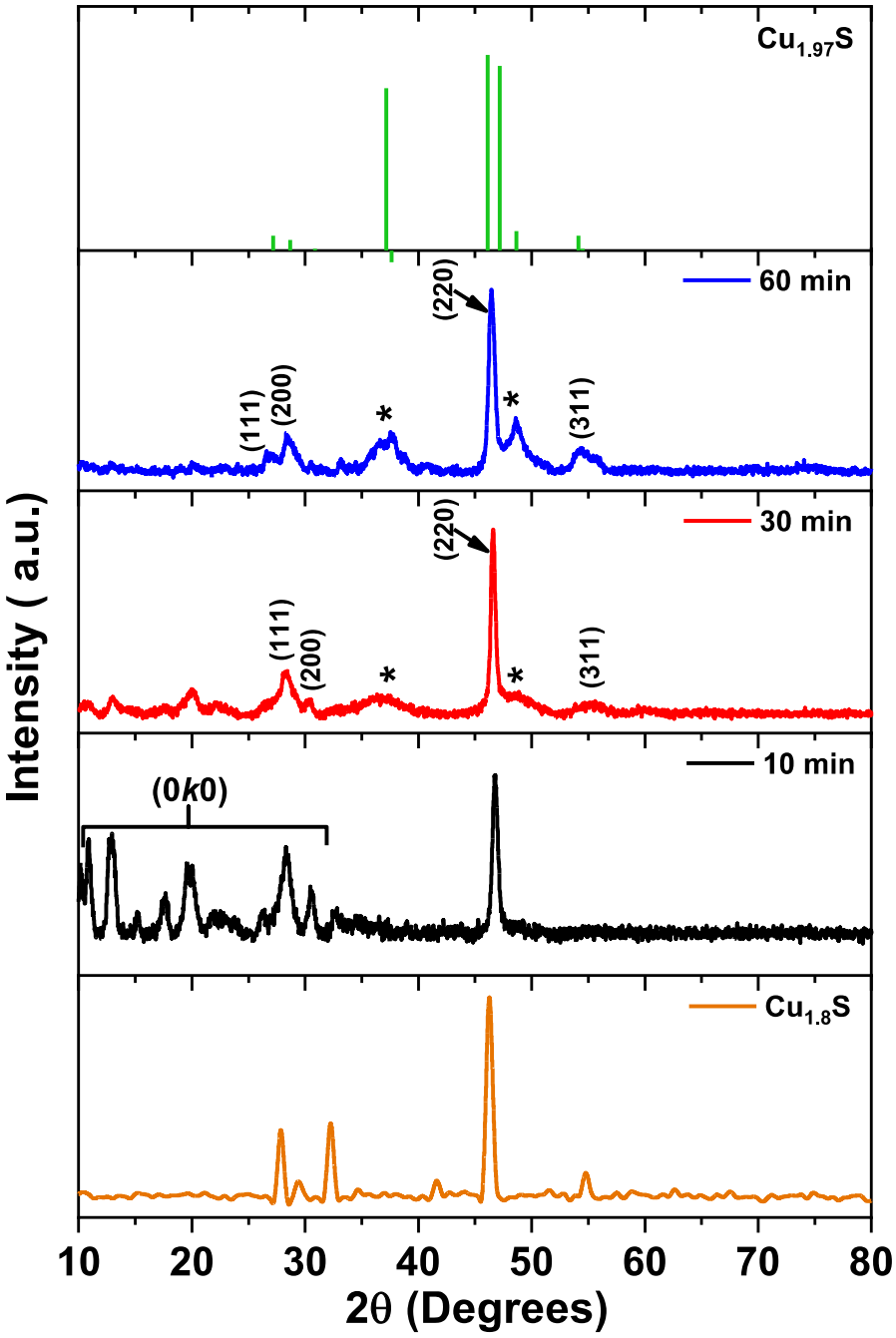


Figure 4.4: Powder X-ray diffractogram patterns for synthesized $Cu_{2-x}S$ particles at different reactions times (10, 30, and 60 min) with the corresponding peak matching PXRD spectra for $Cu_{1.97}S$ and from the XRD database, $Cu_{1.8}S$ (JCPDS 622980).

To study the optical properties of the copper sulfide particles suspended in ethanol, UV-vis absorption spectroscopy was used. From the absorption spectra obtained for the 10 min and 30 min reaction times, there are broad shoulders observed at 430 nm – 641 nm and 375 nm – 734 nm respectively. An increase in absorbance from 0.185 to 0.200 for the 30 min reaction can be attributed to monomer formation and crystal growth. Particles form as the large aggregated intermediate concentration is consumed to produce copper sulfide nuclei. There are large surface interactions and defects due to particle formation at 10 and 30 min. This will effectively lead to the concentration of free holes reducing and a red shift is induced and slight peak broadening [27], [28]. This is noted as the peaks broadened and shifted from 641 nm to 734 nm. From 30 min to 60 min the spectra show a reduced absorption shoulder of 400 nm – 539 nm, this could be explained using the plasmonic resonance effect. Plasmonic resonance is generated when the incident light interacts with the electrons in the conduction band of the metal nanoparticles [29]. Since the plasmon frequency is influenced by the size, shape, and composition of nanomaterials [30], the different phases of $Cu_{2-x}S$ will result in different absorbance spectra. A high concentration of free holes due to Cu-deficiency will produce a high plasmon frequency and increase the absorption band (**Figure 4.6**) [31] as observed in the 30 min and 60 min spectra. Digenite phase $Cu_{1.8}S$ is mostly present at 30 min therefore the absorption is higher compared to the 60 min spectrum which shows reduced absorption as the copper concentration increases and some of the copper-rich $Cu_{1.97}S$ phases are identified.

To find the bandgaps of the synthesized materials Tauc plots were used. Copper sulfides are classed as p-type semiconductors due to the cationic vacancies present in the lattice [29]. These free holes determine the energy needed to excite an electron from the valence band to the conduction band, this is defined as band energy [24]. From the Tauc plots **Figure 4.5(b)**, the band energies were 1.77 eV (10 min), 1.70 eV (30 min) and 1.50 eV (60 min). Bandgap is also dependent on particle size and Cu-deficiency this can be observed in the obtained bandgaps. Progressive growth of the nanostructures as more Cu monomers are deposited onto the surface of the copper sulfide nuclei resulted in the bandgaps decreasing. An increase in size and a decrease in Cu-deficiency results in a decreased band energy [17], [32].

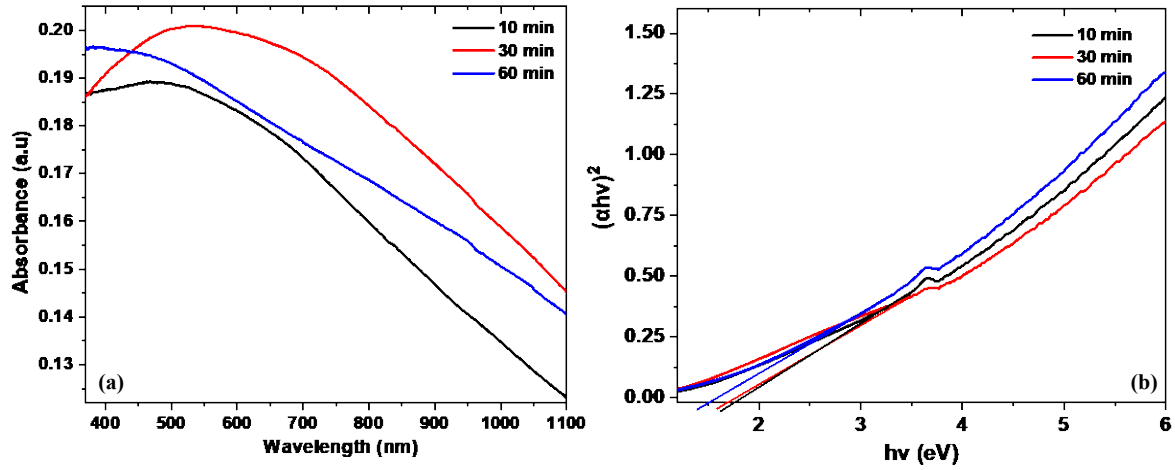


Figure 4.5: (a) UV-vis absorption spectra of synthesized $Cu_{2-x}S$ particles at different reaction times, using CuCl as a Cu precursor and (b) their corresponding Tauc plots.

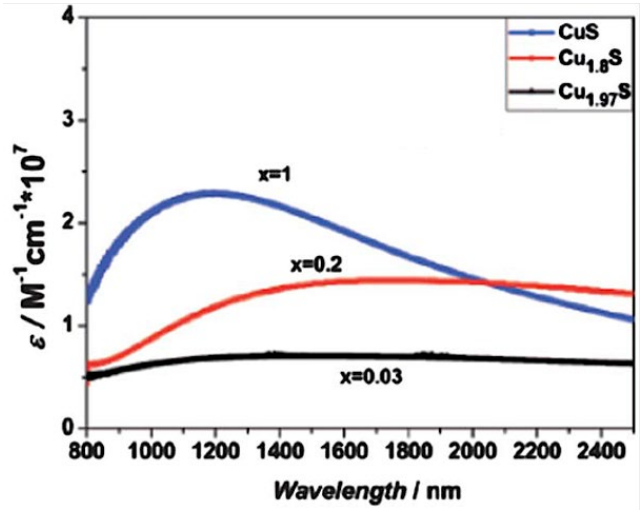


Figure 4.6: Near-infrared spectra of $Cu_{2-x}S$ nanostructures, showing absorption energy with relation to increasing copper deficiency [31].

Further analysis of the synthesized material was done using EDX to determine the elemental composition of the material at 60 min and the corresponding SEM micrograph gave additional information on morphology. SEM signal at around 1.5 keV represents a background signal due to the aluminium (Al) sample stub, as a sample was dispersed in ethanol and deposited directly onto the sample stub. From the SEM micrograph, cloud-like and flaky materials are observed, this corroborates the TEM micrograph and PXRD pattern, as both showed the presence of two different phases of copper sulfide materials. The flaky materials can be allocated to upright thin hexagonal plates shown in **Figure 4.3(c)**.

Elemental analysis from the EDX spectrum displayed Cu, S, and Cl element peaks. The presence of halide ions such as chloride ions (Cl^-) during nanoparticle synthesis can alter the shape of the material [33], [27]. In this synthesis, CuCl was used as a copper source and its dissociation resulted in Cl^- ions. An increase in Cl^- ions can reduce the structural quality of the material as their presence affects the nucleation and growth mechanisms [34], [35].

Despite the weak binding energy between Cu and Cl, the chloride anions still have a strong affinity for the copper ions. According to the reactivity trend of non-metals Cl^- ions are more reactive than S^{2-} since they have higher electronegativity. The weak repulsion between the two ions (Cl and Cu) leads to the Cl^- ions being adsorbed onto the nanoparticles, but they gradually dissociate as the reaction progresses [36]. An increased concentration of the Cl^- ions leading to their surface adsorption does not hinder the lateral growth of the particles [34]. This explains the prolonged crystal formation and the thin nanosheets observed in the TEM micrographs at 30 mins. This is also denoted by Himstedt *et al.* as they observed large amorphous crystalline areas when the Cl^- concertation was high and the formation of crystalline particles when the Cl^- concentration decreased to 9 % during the formation of nickel sulfide nanoparticles [33]. Since the Cl^- ions eventually dissociate the thin hexagonal nanoplates are then observed later on in the reaction. The formation of nanoplates in the presence of Cl^- was also observed by Tang *et al.* in the formation of $CuInS_2$ [37].

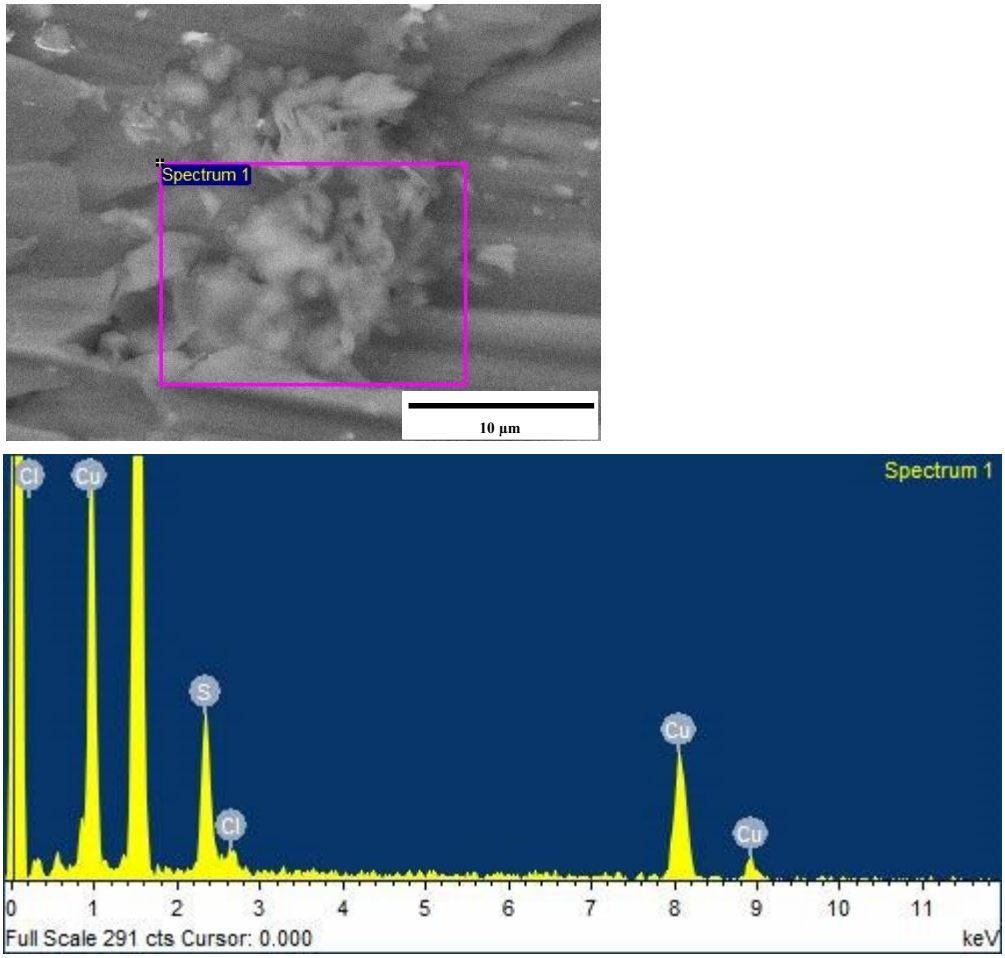


Figure 4.7: EDX spectrum and corresponding SEM micrograph of synthesized $Cu_{2-x}S$ at 60 min.

4.3.2 Nanostructures resulting from Copper (II) acetylacetonate

Heating $Cu(acac)_2$ in a mixture of DDT and OLA resulted in the formation of nanohexagons as shown in TEM micrographs obtained (**Figure 4.8**). The observed morphology at 10 min exhibits a crystalline area with small circular particles embedded on it. At 30 min both circular and hexagonal nanoparticles are observed with an average size of 8.6 nm. When the reaction time of 60 min was reached hexagonal nanoplates of different sizes are observed with an average size of 30.4 nm. From the TEM micrograph in **Figure 4.8**, there are no different morphologies of the as-synthesized $Cu_{2-x}S$ at the final reaction time.

The different shapes can be attributed to the nanoplates being arranged in different orientations on the grid, as some slide beside others creating a layered stack. Whilst some nanoplates are arranged in an upright manner or at an angle on the grid. The growth pattern of the nanoplates follows the expected nucleation and growth order. The dissociation of the $Cu(acac)_2$ is a gradual and constant process leading to small concentrations of copper being released regularly for immediate intermediate reactions to occur. At high reaction temperatures, the copper thiolate intermediates dissociate to produce monomers at high concentrations, encouraging a burst of nucleation and fast growth. The relatively small concentration of monomers is depleted due to the formation of nuclei. Leading to the small, monodispersed nanoparticles which are observed at 30 min. At 10 min, the same is observed at smaller concentrations since the reactions are beginning. As the reaction continues and $Cu(acac)_2$ goes through further thermolysis, in situ intermediates are formed leading to a lower nucleation rate whilst the monomer formation is constant. This results in the sizes of the previously produced $Cu_{2-x}S$ nanoparticles increasing in size as fewer nuclei are formed under constant monomer supply [38], this is observed with the increase in particle size from 8.6 nm in the 30 min sample to 30.4 nm in the 60 min sample.

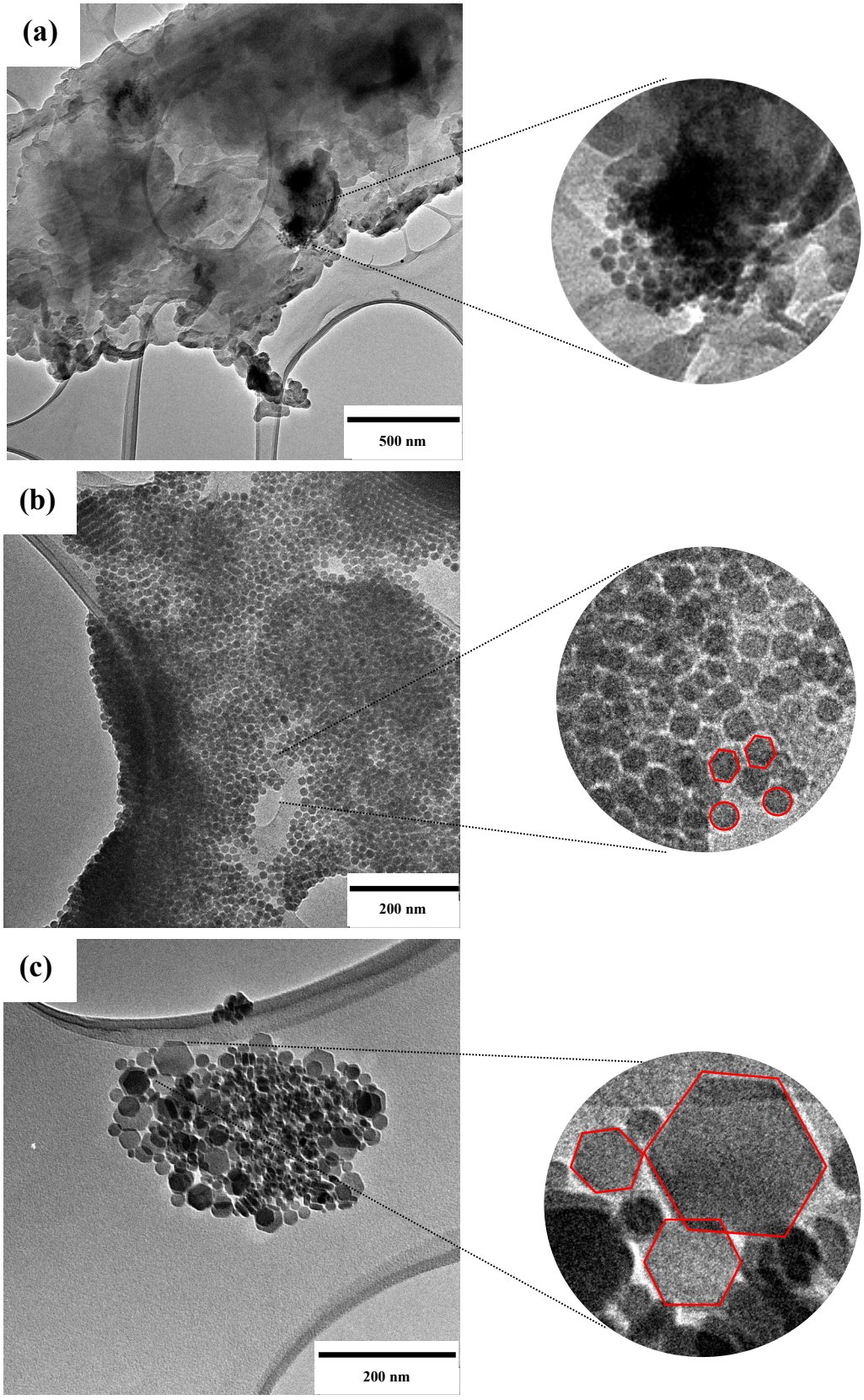


Figure 4.8: Synthesized $Cu_{2-x}S$ TEM micrographs (a)-(c) and (d)-(e) particle size distribution for particles at 30 and 60 min reaction time using $Cu(acac)_2$ as a precursor.

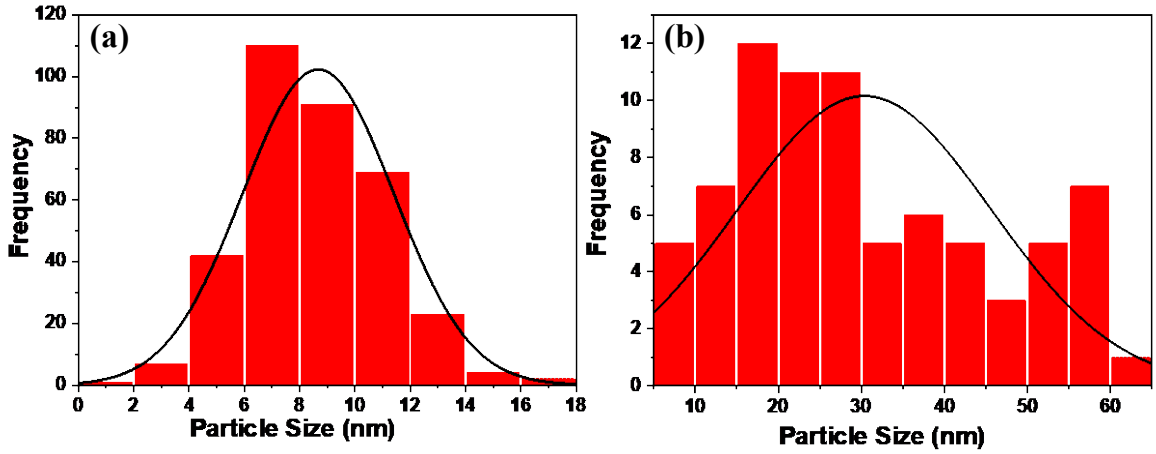


Figure 4.9: Particle size distribution for synthesized $Cu_{2-x}S$ particles at 30 and 60 min reaction time using $Cu(acac)_2$ as a precursor.

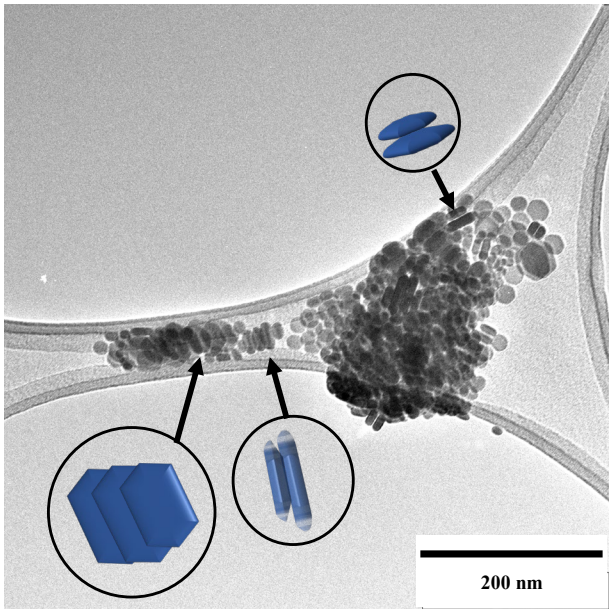


Figure 4.10: TEM micrograph of different orientations for synthesized $Cu_{2-x}S$ at 60 min reaction time.

From the PXRD pattern obtained at different reaction times of the synthesized $Cu_{2-x}S$ using copper (II) acetylacetonate. At the beginning of the reaction (10 min), the copper sulfide was indexed to the orthorhombic α-Cu_2S (PDF 00-002-1286). The chalcocite phase of $Cu_{2-x}S$ has two polymorphs, α-Cu_2S which has low stability and poor crystallinity, this phase is low chalcocite and can easily degrade to djurleite $Cu_{1.97}S$ [39], [40]. At 30 min, a small (211) peak is observed, indicating the formation of β-Cu_2S and at 60 min the synthesized copper sulfide is indexed to hexagonal chalcocite β-Cu_2S (PDF 00-026-1116). This corroborates the nanoparticle formation and growth stated for the change in morphology and particle size

observed in the TEM micrographs **Figure 4.8** and **Figure 4.9** as the reaction progresses the synthesized particles grow and change phases. The (102), (110), (103) and (004) peaks in the 2θ region of 37° – 55 ° are observed at each reaction time indicating the formation of Cu_2S. More details are in Supplementary Fig. S4.2.

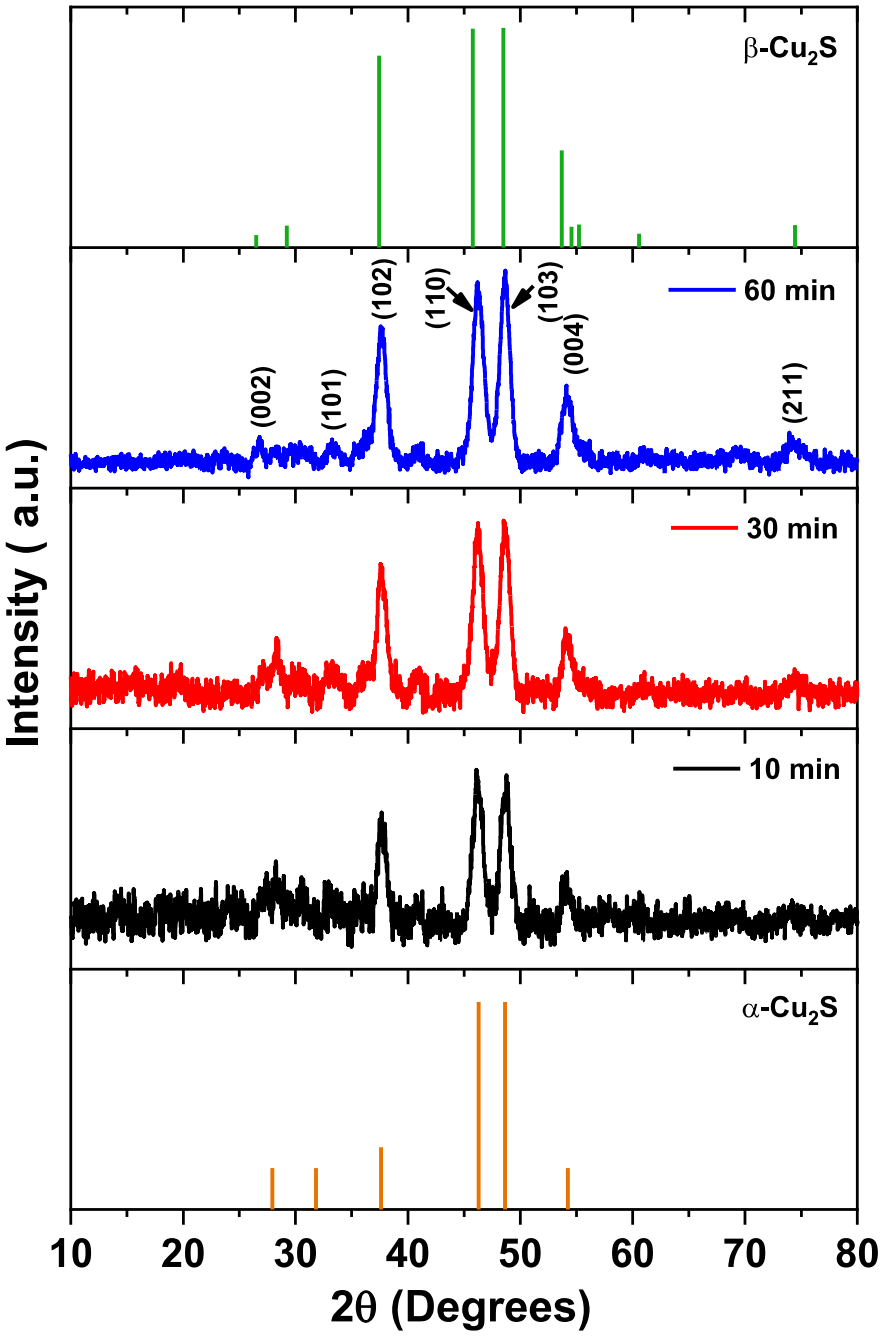


Figure 4.11: Powder X-ray diffraction patterns for as-synthesized $Cu_{2-x}S$ particles at different reactions times and the corresponding peak matching PXRD spectra for *α* and *β* Cu_2S.

To study the optical properties of the synthesized copper sulfide material, UV-vis was used. The spectrum obtained for the 10 min sample lacks a sharp maximum, this could be attributed to the different morphologies that are present due to intermediates, monomers, and some copper sulfide nuclei as seen in the TEM micrographs. As the reaction continues weak and broad shoulders are observed due to the formation and growth of the copper sulfide nanoparticles. According to Goh *et al.* particle sizes affect the absorption spectrum, an increase in size results in an increase in absorbance [41], this is seen in the absorption spectra obtained for the different reaction times. At 10 min large crystalline areas are observed, at 30 min and 60 min the particle sizes increase from 8.6 nm to 30.4 nm and the absorbance also increases from 0.165 to 0.184. A broad shoulder in the region 404 nm – 552 nm is observed for the 30 min reaction and 304 nm – 467 nm for the 60 min sample. The Mie theory states that the shape and size of particles can influence the surface plasmonic resonance to give different peaks [29], [42].

This also influences the bandgaps of the materials as shown in the Tauc plots **Figure 4.12(b)**. An inverse relationship exists between particle size and bandgap energy, an increase in energy results from a decrease in size [43]. This is in agreement with the observations made from the UV and Tauc plots **Figure 4.12**. At 30 min (8.6 nm) the energy is 1.98 eV and at 60 min (30.4 nm) the energy decreases to 1.70 eV. Semiconducting copper sulfide particles at 30 min exhibit quantum size effect as the bandgap energy is high and the particle radius is small [44]. The bandgap for Cu_2S is also dependent on stoichiometry as the material becomes less degenerate due to increased copper concentration as the Cu_2S particles grow from α-Cu_2S to β-Cu_2S the bandgap reduces.

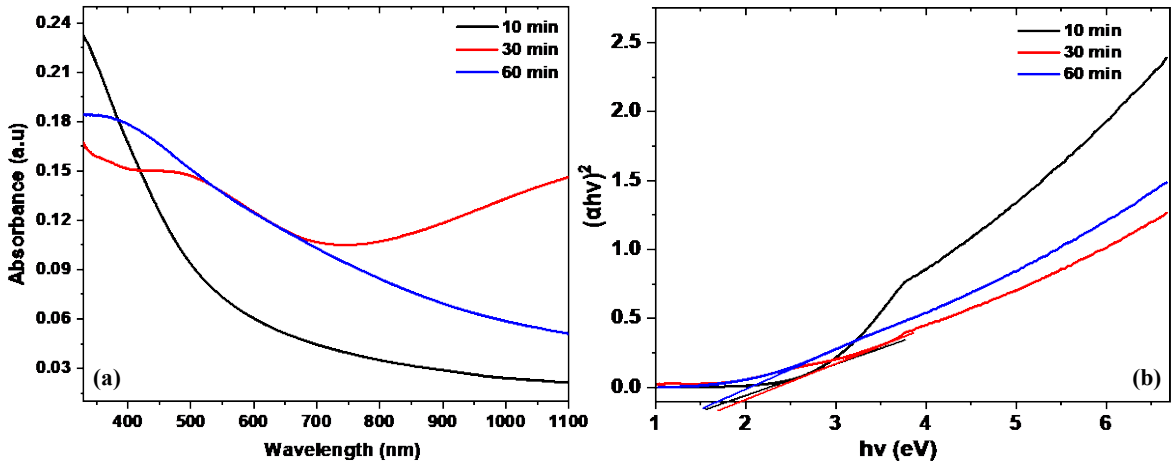


Figure 4.12: a) UV-Vis absorption spectra of synthesized $Cu_{2-x}S$ particles at different reaction times, using $Cu(acac)_2$ as a Cu precursor and (b) their corresponding Tauc plots.

To determine the elements present in the material and further analyze the morphology of the synthesized particles, both SEM and EDX were used. The signal at around 1.5 keV represents aluminium (Al) as a result of the sample holder used and because the synthesized samples were dispersed in ethanol and deposited directly onto the sample stub. From the SEM micrograph, small flaky-like materials are observed which could be a combination of the different orientations of hexagonal nanoparticles such as the upright orientation observed in the TEM micrographs **Figure 4.8(c)** and **Figure 4.10.** The EDX spectrum shows the presence of Cu and S elements.

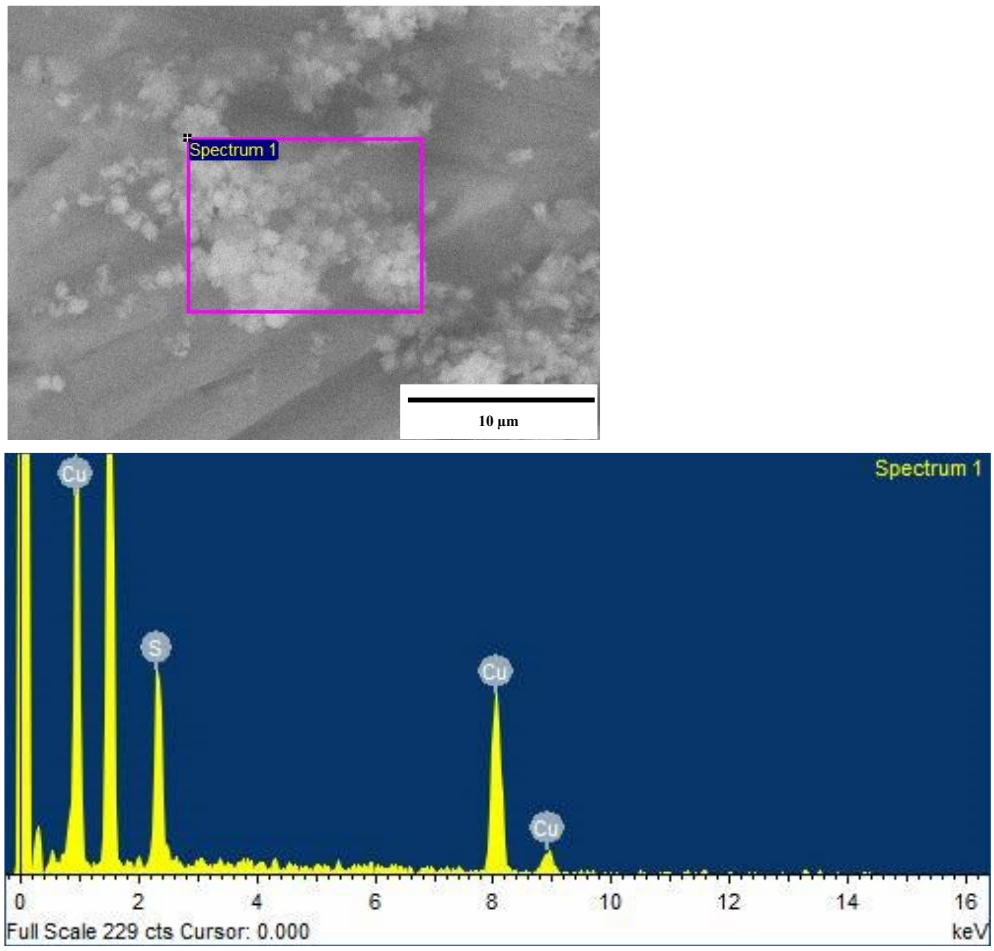


Figure 4.13: EDX spectrum and corresponding SEM micrograph of synthesized $Cu_{2-x}S$ at 60 min.

4.4 Comparison of the resulting $Cu_{2-x}S$ nanostructures

The rate of reaction and morphology of the synthesized particles is dependent on the rate of decomposition of the precursors and the intermediates but mostly the precursor atom to ligand interaction. The energy required for the thermal decomposition of the copper sources is dependent on their bond strength, CuCl is monodentate, and $Cu(acac)_2$ is a chelating ligand with formation enthalpies (ΔH_f) of -138 KJ/mol [45] and -1323 KJ/mol [46] respectively. Therefore, the decomposition of CuCl into Cu^+ and Cl^- has a single-step process and requires less energy compared to the three-step decomposition of $Cu(acac)_2$ [$Cu(acac)_2 \longrightarrow Cu(acac) \longrightarrow Cu^{2+} \longrightarrow Cu^+$] [47]. The rate of Cu^+ release will affect the concentration of the monomers present in the reaction which will then influence the rate of nucleation and growth of the nanoparticles. The higher the concentration of monomers the faster the nucleation process and the rate of growth for the nanoparticles, a slow continuous release of monomers will result in a moderate growth rate [38], [48].

From the use of CuCl as the copper precursor we found that although the dissociation of the CuCl bonding is faster and takes less energy, the presence of the halide ion (Cl^-) in the reaction solution inhibited the fast dissociation of the intermediate. This delayed the change in the morphology and the formation of Cu_2S particles due to the presence of the intermediates observed at 10 min and 30 min reaction times. The affinity of Cl ions for Cu^+ and their deposition on the copper sulfide nuclei resulted in only lateral growth of the nanoparticles therefore thin and large particles were formed. Djurleite $Cu_{1.97}S$ and digenite $Cu_{1.8}S$ phases were found to be present at the final reaction time of 60 min. This might have been due to the hindered growth resulting in fewer Cu monomers reacting with copper sulfide nuclei leading to Cu deficiency. The stability of a reactant influences its reactivity since the $acac^-$ ligand is more stable it is less reactive compared to S^{2-}. The reaction between the Cu^+ and S^{2-} ions is more favourable and has a lower ΔH_f of -79.5 KJ/mol [49] in comparison to ΔH_f of $Cu(acac)_2$ which is -1323 KJ/mol.

Therefore, there is less hindrance to the formation of copper sulfide particles when $Cu(acac)_2$ is used as a copper source compared to when there is a halide ion (Cl) present. This is corroborated by the PXRD patterns and TEM micrographs as the formation of Cu_2S is accomplished at lower reaction times and distinctive morphologies are observed when $Cu(acac)_2$ is used. The copper sulfide nanostructures synthesized using $Cu(acac)_2$ did not exhibit the intermediate peaks in the PXRD spectrums obtained and because there was no hindrance from the presence of halide ions, the chalcocite phase Cu_2S was formed at the beginning of the reaction (10 min). However due to the energy required to break the $Cu(acac)_2$ bonds and decompose to give Cu^+ there is a slow and continued release of monomers that then produce in-situ intermediates and results in the growth of some nuclei. The $Cu_{2-x}S$ particles synthesized followed different growth patterns, CuCl followed **Figure 4.14(a)** and $Cu(acac)_2$ followed **Figure 4.14(b)**.

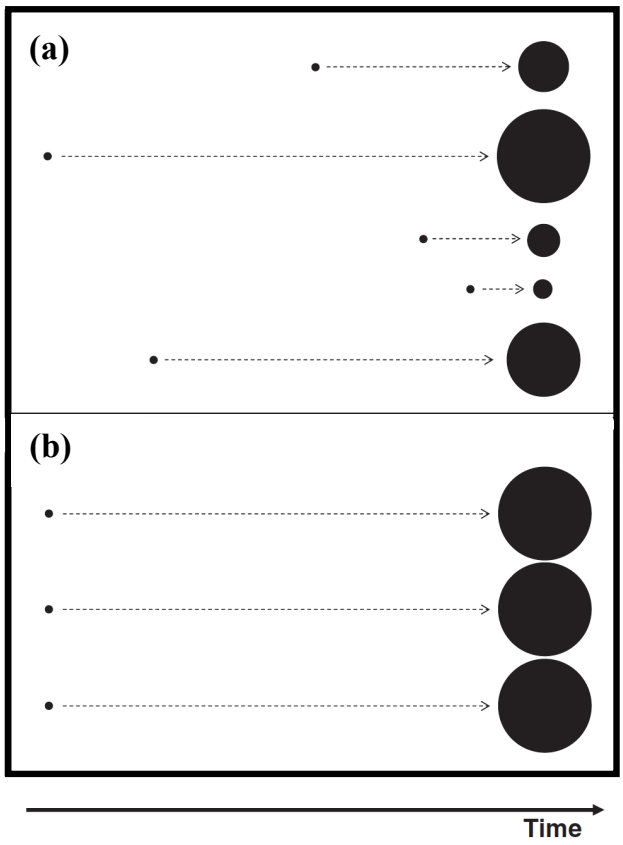


Figure 4.14: Diagram illustrating different reaction systems when nucleation occurs (a) at random and (b) all at once, and how the nuclei (•) grows with increased reaction time [48].

Both reactions exhibited plasmonic resonance and the copper deficiencies affected the bandgap energy. Copper-rich materials showed lower bandgap energies which increase when free carriers are present due to copper deficiency Figure **4.15**. According to literature, the bandgap energy (E_g) of $Cu_{2-x}S$ varies from 1.2 eV to 2.53 eV depending on the copper vacancies [32]. The bandgap of Cu_2S is 1.2 eV [50] and $Cu_{1.8}S$ is 1.5 eV [51], other studies such as Quintana-Ramirez *et al.* reported $Cu_{1.8}S$ to be 1.6 eV and chalcocite (Cu_2S) as 1.87 eV. The nanoparticles that were obtained at 60 min had bandgaps of 1.50 and 1.70 eV for CuCl and $Cu(acac)_2$ respectively. Both energies are in the expected bandgap range of 1.2 eV to 2.5 eV [32] for $Cu_{2-x}S$. There are slight differences between the values reported by Quintana-Ramirez and those obtained in this research for $Cu_{1.8}S$ and Cu_2S. This might be due to differences in sizes of the particles synthesized and the presence of different $Cu_{2-x}S$ phases. Smaller particles, 30.4 nm from the $Cu(acac)_2$ precursor have a large reactive surface area for reactions to occur [52] compared to the large particles (478.5 nm) obtained from the CuCl copper precursor.

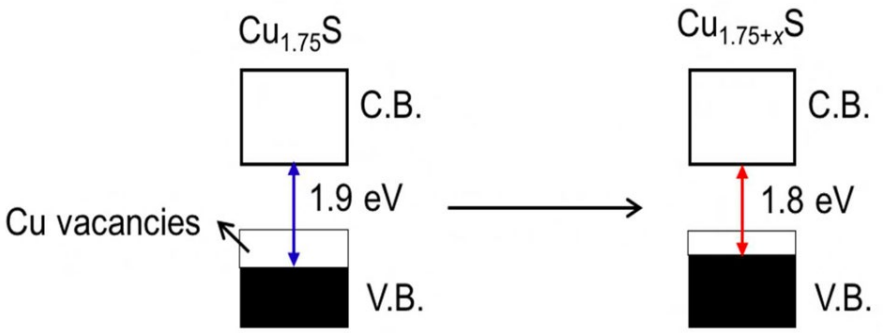


Figure 4.15: Diagram showing the change in bandgap due to copper vacancies [17].

4.5 Conclusion

In summary, copper sulfide particles were synthesized using one-pot synthesis, and differences in morphology and optical properties were observed when reaction parameters such as time and precursors were changed. The copper precursor parameter that was changed in this study affected the nucleation and growth process of the copper sulfide particles. This resulted in different phases, morphologies, and particle sizes of $Cu_{2-x}S$ being present at the end of the reaction. The presence of the halide ion in CuCl affected the growth of the copper sulfide particles by delaying the intermediate dissolution. Slow decomposition of $Cu(acac)_2$ to Cu^+ resulted in random nucleation and growth occurring as the reaction time progressed. The different precursors both gave phase variations close to Cu_2S. The β-Cu_2S nanoparticles synthesized using $Cu(acac)_2$ as the copper precursor exhibited better characteristics, their small particle size allows for better reactivity with other materials due to the larger surface area to volume ratio. As such, they make good candidates in applications such as light-harvesting devices.

References

[1] W. Tremel, H. Kleinke, V. Derstroff, and C. Reisner, "Transition metal chalcogenides: new views on an old topic," *J. Alloys Compd.*, vol. 219, no. 1–2, pp. 73–82, 1995.

[2] R. S. and R. N. Tang W, "Electronic & Optical properties of transition- metal dichalcogenides," *J. Nanotechnol. Nanosci.*, vol. 2, no. July, pp. 59–65, 2017.

[3] C.-A. Tseng and C.-P. Lee, "Transition Metal Chalcogenides for the Electrocatalysis of Water," *Adv. Funct. Mater.*, pp. 1–15, 2020.

[4] T. Heine, "Transition metal chalcogenides: Ultrathin inorganic materials with tunable

electronic properties," *Acc. Chem. Res.*, vol. 48, no. 1, pp. 65–72, 2015.

[5] G. Kakavelakis, L. Gouda, Y. Tischler, I. Kaliakatsos, and K. Petridis, *Two Dimensional Transition Metal Dichalcogenides for Solution-Processed Organicand Perovskite Solar Cells*. Springer Singapore, 2019.

[6] S. Shanmugaratnam and S. Rasalingam, "Transition Metal Chalcogenide (TMC) Nanocomposites for Environmental Remediation Application over Extended Solar Irradiation," *Nanocatalysts*, pp. 1–22, 2019.

[7] C. H. Lai, M. Y. Lu, and L. J. Chen, "Metal sulfide nanostructures: Synthesis, properties and applications in energy conversion and storage," *J. Mater. Chem.*, vol. 22, no. 1, pp. 19–30, 2012.

[8] P. D. Matthews, P. D. McNaughter, D. J. Lewis, and P. O'Brien, "Shining a light on transition metal chalcogenides for sustainable photovoltaics," *Chem. Sci.*, vol. 8, no. 6, pp. 4177–4187, 2017.

[9] P. Roy and S. K. Srivastava, "Nanostructured copper sulfides: Synthesis, properties and applications," *CrystEngComm*, vol. 17, no. 41, pp. 7801–7815, 2015.

[10] J. Chang and E. R. Waclawik, "Colloidal semiconductor nanocrystals: Controlled synthesis and surface chemistry in organic media," *RSC Adv.*, vol. 4, no. 45, pp. 23505–23527, 2014.

[11] M. R. Gao, Y. F. Xu, J. Jiang, and S. H. Yu, "Nanostructured metal chalcogenides: Synthesis, modification, and applications in energy conversion and storage devices," *Chem. Soc. Rev.*, vol. 42, no. 7, pp. 2986–3017, 2013.

[12] H. Cai, Y. Gu, Y. C. Lin, Y. Yu, D. B. Geohegan, and K. Xiao, "Synthesis and emerging properties of 2D layered III-VI metal chalcogenides," *Appl. Phys. Rev.*, vol. 6, no. 4, 2019.

[13] M. A. Airo, S. Gqoba, M. P. Kalenga, S. Govindraju, M. J. Moloto, and N. Moloto, "Synthesis and characterization of indium monoselenide nanosheets: A proposed pseudo top-down mechanism," *J. Cryst. Growth*, vol. 406, pp. 1–7, 2014.

[14] J. H. Han, M. Kwak, Y. Kim, and J. Cheon, "Recent Advances in the Solution-Based Preparation of Two-Dimensional Layered Transition Metal Chalcogenide Nanostructures," *Chem. Rev.*, vol. 118, no. 13, pp. 6151–6188, 2018.

[15] C. B. Murray, S. Sun, W. Gaschler, H. Doyle, T. A. Betley, and C. R. Kagan, "Colloidal synthesis of nanocrystals and nanocrystal superlattices," *IBM J. Res. Dev.*, vol. 45, no. 1, pp. 47–56, 2001.

[16] S. Jeong, D. Yoo, J. T. Jang, M. Kim, and J. Cheon, "Well-defined colloidal 2-D

layered transition-metal chalcogenide nanocrystals via generalized synthetic protocols," *J. Am. Chem. Soc.*, vol. 134, no. 44, pp. 18233–18236, 2012.

[17] L. Chen and G. Li, "Functions of 1-Dodecanethiol in the Synthesis and Post-Treatment of Copper Sulfide Nanoparticles Relevant to Their Photocatalytic Applications," *ACS Appl. Nano Mater.*, vol. 1, no. 9, pp. 4587–4593, 2018.

[18] P. W. Ayers, "An elementary derivation of the hard/soft-acid/base principle," *J. Chem. Phys.*, vol. 122, no. 14, 2005.

[19] Y. Zhai and M. Shim, "Effects of Copper Precursor Reactivity on the Shape and Phase of Copper Sulfide Nanocrystals," *Chem. Mater.*, vol. 29, no. 5, pp. 2390–2397, 2017.

[20] Y. Zheng, N. Chen, C. Wang, X. Zhang, and Z. Liu, "Oleylamine-mediated hydrothermal growth of millimeter-long cu nanowires and their electrocatalytic activity for reduction of nitrate," *Nanomaterials*, vol. 8, no. 4, 2018.

[21] S. Mourdikoudis and L. M. Liz-Marzán, "Oleylamine in nanoparticle synthesis," *Chem. Mater.*, vol. 25, no. 9, pp. 1465–1476, 2013.

[22] I. C. Maurya, S. Senapati, S. Singh, P. Srivastava, P. Maiti, and L. Bahadur, "Effect of Particle Size on the Performance of TiO2 Based Dye-Sensitized Solar Cells," *ChemistrySelect*, vol. 3, no. 34, pp. 9872–9880, 2018.

[23] N. Sandhyarani and T. Pradeep, "An investigation of the structure and properties of layered copper thiolates," *J. Mater. Chem.*, vol. 11, no. 4, pp. 1294–1299, 2001.

[24] Y. Wang *et al.*, "One-pot synthesis and optical property of copper(I) sulfide nanodisks," *Inorg. Chem.*, vol. 49, no. 14, pp. 6601–6608, 2010.

[25] M. Inoue and I. Hirasawa, "The relationship between crystal morphology and XRD peak intensity on CaSO4·2H2O," *J. Cryst. Growth*, vol. 380, pp. 169–175, 2013.

[26] C. Rohner, A. Pekkari, H. Härelind, and K. Moth-Poulsen, "Synthesis of Cu Nanoparticles: Stability and Conversion into Cu2S Nanoparticles by Decomposition of Alkanethiolate," *Langmuir*, vol. 33, no. 46, pp. 13272–13276, 2017.

[27] R. Lesyuk, E. Klein, I. Yaremchuk, and C. Klinke, "Copper sulfide nanosheets with shape-tunable plasmonic properties in the NIR region," *Nanoscale*, vol. 10, no. 44, pp. 20640–20651, 2018.

[28] P. A. Ajibade and N. L. Botha, "Synthesis, optical and structural properties of copper sulfide nanocrystals from single molecule precursors," *Nanomaterials*, vol. 7, no. 2, 2017.

[29] J. Jana, M. Ganguly, and T. Pal, "Enlightening surface plasmon resonance effect of metal nanoparticles for practical spectroscopic application," *RSC Adv.*, vol. 6, no. 89,

pp. 86174–86211, 2016.

[30] R. M. S. Pereira, J. Borges, G. V. Smirnov, F. Vaz, and M. I. Vasilevskiy, “Surface Plasmon Resonance in a Metallic Nanoparticle Embedded in a Semiconductor Matrix: Exciton-Plasmon Coupling,” *ACS Photonics*, vol. 6, no. 1, pp. 204–210, 2019.

[31] Y. Zhao and C. Burda, “Development of plasmonic semiconductor nanomaterials with copper chalcogenides for a future with sustainable energy materials,” *Energy Environ. Sci.*, vol. 5, no. 2, pp. 5564–5576, 2012.

[32] L. Isac, I. Popovici, A. Enesca, and A. Duta, “Copper sulfide (CuxS) thin films as possible p-type absorbers in 3D solar cells,” *Energy Procedia*, vol. 2, no. 1, pp. 71–78, 2010.

[33] R. Himstedt, D. Hinrichs, J. Sann, A. Weller, G. Steinhauser, and D. Dorfs, “Halide ion influence on the formation of nickel nanoparticles and their conversion into hollow nickel phosphide and sulphide nanocrystals,” *Nanoscale*, vol. 11, no. 32, pp. 15104–15111, 2019.

[34] G. Riveros, M. León, and D. Ramírez, “Effect of chloride ions on the structural, optical, morphological, and electrochemical properties of Cu2O films electrodeposited on fluorine-doped tin oxide substrate from a DMSO solution,” *J. Chil. Chem. Soc.*, vol. 61, no. 4, pp. 3219–3223, 2016.

[35] S. Olsen, “Synthesis of Copper Sulphides: A Green Chemistry Microwave Approach,” 2020.

[36] Y. Xiong *et al.*, “Crucial role of anions on arrangement of Cu2S nanocrystal superstructures,” *Small*, vol. 10, no. 8, pp. 1523–1528, 2014.

[37] A. Tang, Z. Hu, Z. Yin, H. Ye, C. Yang, and F. Teng, “One-pot synthesis of CuInS2 nanocrystals using different anions to engineer their morphology and crystal phase,” *Dalt. Trans.*, vol. 44, no. 19, pp. 9251–9259, 2015.

[38] W. Van Der Stam *et al.*, “Shape control of colloidal Cu2-xS polyhedral nanocrystals by tuning the nucleation rates,” *Chem. Mater.*, vol. 28, no. 18, pp. 6705–6715, 2016.

[39] M. Lotfipour, T. MacHani, D. P. Rossi, and K. E. Plass, “α-Chalcocite nanoparticle synthesis and stability,” *Chem. Mater.*, vol. 23, no. 12, pp. 3032–3038, 2011.

[40] H. T. Evans, “Djurleite (Cu1.94S) and Low Chalcocite (Cu2S): New Crystal Structure Studies,” *Science*, vol. 203, no. 4378, pp. 356–358, 1979.

[41] E. G. Goh, X. Xu, and P. G. McCormick, “Effect of particle size on the UV absorbance of zinc oxide nanoparticles,” *Scr. Mater.*, vol. 78–79, pp. 49–52, 2014.

[42] L. Liu *et al.*, “Controllable transformation from rhombohedral Cu1.8S nanocrystals to

hexagonal CuS clusters: Phase- and composition-dependent plasmonic properties," *Chem. Mater.*, vol. 25, no. 23, pp. 4828–4834, 2013.

[43] M. Singh, M. Goyal, and K. Devlal, "Size and shape effects on the band gap of semiconductor compound nanomaterials," *J. Taibah Univ. Sci.*, vol. 12, no. 4, pp. 470–475, 2018.

[44] G. Ramalingam *et al.*, "Quantum Confinement Effect of 2D Nanomaterials," *Quantum Dots - Fundam. Appl.*, pp. 1–12, 2020.

[45] M. W. Chase Jr., "NIST-JANAF Themochemical Tables. 4th Edition," *J. Phys. Chem. Ref. Data, Monogr.*, vol. 9, pp. 1–1951, 1998.

[46] W. Kąkołowicz and E. Giera, "Standard enthalpies of formation of the chelate complexes of some 3d-electron elements with pentane-2,4-dione metal-oxygen bond energies and ligand-field stabilization energies," *J. Chem. Thermodyn.*, vol. 15, no. 3, pp. 203–210, 1983.

[47] S. Yoda, Y. Takebayashi, K. Sue, T. Furuya, and K. Otake, "Thermal decomposition of copper (II) acetylacetonate in supercritical carbon dioxide: In situ observation via UV–vis spectroscopy," *J. Supercrit. Fluids*, vol. 123, pp. 82–91, 2017.

[48] S. G. Kwon and T. Hyeon, "Formation mechanisms of uniform nanocrystals via hot-injection and heat-up methods," *Small*, vol. 7, no. 19, pp. 2685–2702, 2011.

[49] J. A. Dean, "Lange's Handbook of Chemistry (Standard Thermodynamic Values)," *Mater. Manuf. Process.*, vol. 5, no. 4, pp. 687–688, 1990.

[50] I. Kriegel, J. Rodríguez-Fernández, E. Da Como, A. A. Lutich, J. M. Szeifert, and J. Feldmann, "Tuning the light absorption of Cu1.97S nanocrystals in supercrystal structures," *Chem. Mater.*, vol. 23, no. 7, pp. 1830–1834, 2011.

[51] K. Itoh, T. Kuzuya, and K. Sumiyama, "Morphology and composition-controls of CuxS nanocrystals using alkyl-amine ligands," *Mater. Trans.*, vol. 47, no. 8, pp. 1953–1956, 2006.

[52] A. Singh, R. Manivannan, and S. Noyel Victoria, "Simple one-pot sonochemical synthesis of copper sulphide nanoparticles for solar cell applications," *Arab. J. Chem.*, vol. 12, no. 8, pp. 2439–2447, 2019.

Chapter 5

Preparation, characterization, and analysis of the electrocatalytic activity of N- HCS /Cu2S composites as CE material in DSSCs

5.1 Introduction

Cost-effectiveness, stability, and excellent application properties are some of the main qualities that researchers and industries search for when developing materials for specific functions. Composite materials involve the bridging of two or more materials with different or complementary properties to enhance their functionality, making them a compelling area of research for certain applications. To fine-tune the optoelectronic and catalytic properties of materials for photovoltaic (PV) devices, composites exploring the interactions between inorganic and organic components have been explored [1]. Inorganic materials such as colloidal particles of minerals, metal ion/clusters, oxides, and sulfides can enhance the mechanical, and thermal stability of a material, contribute to electrochemical properties or provide an interconnected network for catalysis [2], [3]. Carbon allotropes offer low-cost production, modification of mechanical strength, high surface areas, and improved conductivity [4], [5]. The combination of these two material groups can be considered as new material that exhibits different or a combination of both properties [6].

Carbon materials with inorganic semiconductors have shown an improvement in the overall performance [4], optical and electrical properties [7] as well as good catalytic activity towards the iodide/triiodide redox couple at the counter electrode (CE) in dye-sensitized solar cells [8], [9]. Since the CE is one of the most significant components of the DSSC, given that the reactions occurring at the CE determine the overall efficiency of the solar cell, the material used has to show great electrocatalytic activity and high conductivity [10]. The CE catalyst in a DSSC is used to regenerate I^- from I_3^- and to collect electrons from the external circuit to the electrolyte that is made up of I^- / I_3^- redox species dissolved in an organic liquid [11]. Platinum (Pt) has been used as the CE material due to its good chemical stability, high catalytic reduction, and great conductivity [12], [13] however, it is an expensive noble material. *Kay et al*. found that Pt is easily oxidized to PtI_4 by the I_3^- / I^- electrolyte [14]. Therefore, researchers

aim to find a viable alternative material that is easily available, low cost, and with better stability, electrocatalytic, and conductivity properties.

The use of carbon materials will tremendously reduce the manufacturing costs of DSSCs as carbon is cheaper to make compared to the cost of platinum. The great qualities that carbon materials possess such as good catalytic activity, electrical conductivity, and high thermal stability they are seen as possible alternatives [11], [15], [16]. Metal sulfides have also been explored as CE materials as they are also low cost and earthly abundant, with corrosive resistance, good catalytic behaviour, and stability [17]–[19]. In this work, we explore the preparation of Pt-free composites of binary metal sulfide (Cu_2S) and nitrogen-doped hollow carbon spheres. The composite materials are expected to have corrosion resistance towards the electrolyte and high reactivity for triiodide reaction from the carbon material [20]. The strong resistivity to oxidation from the copper sulfide material will add to the durability and stability of the composite materials [21]. The electrochemical reduction process of the synthesized materials was analyzed using cyclic voltammetry (CV) [22]. For electrochemical reduction, the material used is reduced via heterogeneous electron transfer from the electrically conductive counter electrode. Using the potentiostat as a power source, voltage is applied to the electrode to regulate the energy of the electrons. When the electrons are at a higher energy compared to the lowest unoccupied molecular orbital (LUMO) of the material, an electron is transferred [22]. In a three-electrode that consists of the working electrode (WE), counter electrode (CE), and reference electrode (RE), the CV curves show the reduction and oxidation peaks that correspond to the redox reaction equations of the electrolyte (**Figure 5.1**) [23], [24].

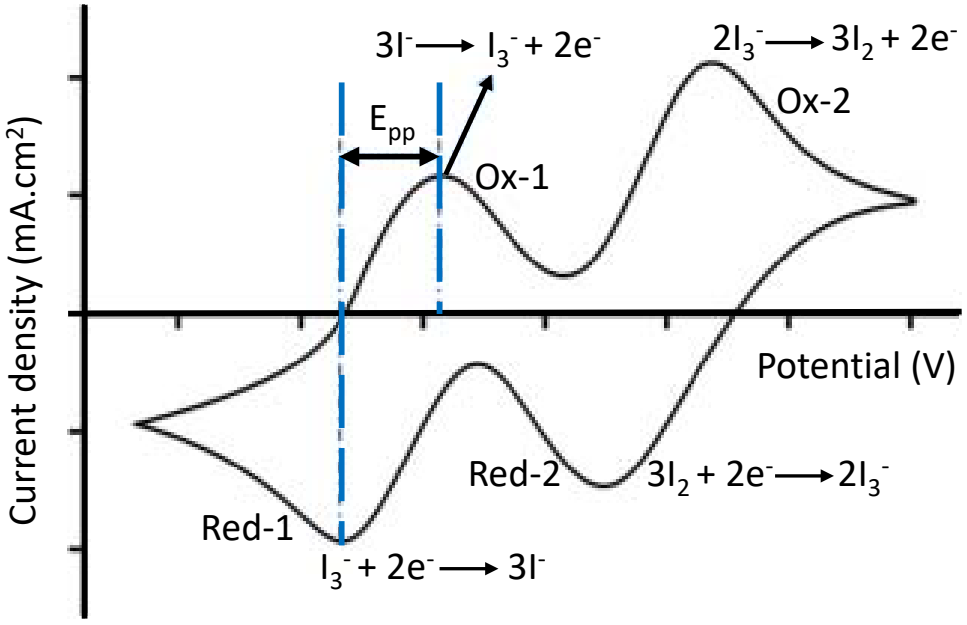


Figure 5.1 Diagram of a cyclic voltammetry plot, showing the redox reaction of the triiodide/iodide electrolyte.

The working electrode will comprise of a spin-coated composite material on a thin film of fluorine-doped tin oxide (FTO) coated glass substrate. Spin-coating was used as it uniformly deposits the material on the conductive FTO glass through the use of centrifugal force [25], the material ink is added to the center of the substrate and then spun at high speed. The ink spreads evenly on the surface of the substrate whilst the solvent evaporates resulting in a film with the desired thickness [26], [27]. In this study, the catalytic performances of the synthesized counter electrode materials will be analyzed using the different electrochemical analysis techniques. Electrochemical impedance spectroscopy (EIS) will be used to evaluate the kinetics of the electrochemical processes and depict the ionic and electronic processes occurring at the CE/electrolyte interface. The Tafel polarization measurement will be used to analyze the interfacial charge-transfer properties of the counter electrode surfaces and the triiodide/iodide electrolyte. Photocurrent-voltage measurements will be used to analyze the photovoltaic properties of the fabricated DSSC devices.

5.2 Experimental

5.2.1 Materials

Ethanol (C_2H_5OH, 96%, Merck), Nafion^{TM} ($C_7HF_{13}O_5S.C_2F_4$, 5 wt%), lithium perchlorate ($LiClO_4$, ≥ 95.0%), lithium iodide (LiI, 99.9%), iodine (I_2, ≥ 99%), acetonitrile (C_2H_3N, ≥ 99.9%), and oleylamine (OLA, 70%) were purchased from Merk© and used without further purification.

5.2.2 Preparation of N-HCS/Cu_2S composites

Different stoichiometric amounts of nitrogen-doped hollow carbon spheres (N-HCS) and copper sulfide (Cu_2S) nanoparticles were used to synthesize the composites. For the 75 wt % N-HCS: 25 wt % Cu_2S, 25 mg of Cu_2S was sonicated in 5 ml of OLA for 30 min. The solution was then transferred to a three-neck round bottom flask containing 10 ml of OLA and 75 mg of N-HCS was added, the mixture was stirred whilst degassing under nitrogen gas for 30 min and heated at 100 °C for 30 min. The resulting particles were precipitated by centrifuging at 8000 rpm and washed with ethanol for 10 min. The same procedure was repeated for 50 wt% N-HCS and 25 wt% N-HCS.

5.2.3 Thin-film fabrication

For ink preparation, each of the composite materials were dispersed in a mixture of ethanol and Nafion^{TM} then sonicated for 30 min. The FTO glass substrates on which the ink was to be deposited were cleaned by sonication first in a diluted detergent solution followed by rinsing with deionized water and then with ethanol for 30 min. After drying, the substrate was fixed onto the spinning plate of the Chemat Technology spin-coater KW-4A Coater. The ink was spread evenly on the substrate by allowing it to disperse at low speed and then homogenizing the coated ink at high speed. This evaporated the solvent and the films were left overnight in an enclosed fumehood to dry thoroughly so that the ink adhered to the substrate.

5.2.4 Electrocatalytic activity

To prepare the triiodide/ iodide electrolyte; 0.05 g of I_2, 0.14 g of LiI, and 1.06 g of $LiClO_4$ were added to 20 mL of acetonitrile. The mixture was stirred until all the salts were dissolved and stored in an amber bottle. The cell comprised of the electrolyte, the prepared CE thin film as the working electrode, Ag/AgCl electrode was used as the reference electrode and for the counter electrode, a platinum wire electrode was used as shown in **Figure 5.2**. To determine the electrocatalytic activity of the materials, cyclic voltammetry curves were obtained using the BASi Epsilon-E2 (1231) potentiostat software.

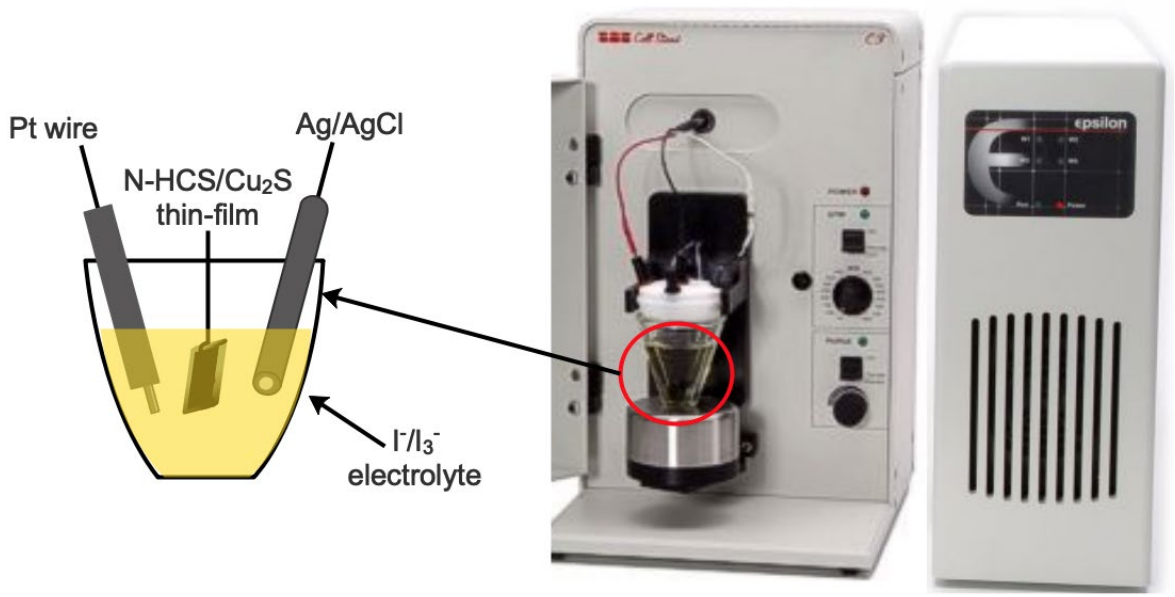


Figure 5.2: Diagram illustrating the cell set-up for cyclic voltammetry analysis.

5.2.5 Dye-sensitized solar cell fabrication

A Pt counter electrode was sputter-coated onto a clean FTO glass substrate and used to compare with the counter electrodes of the synthesized materials. The CEs of the synthesized materials were prepared as stated in **section 5.2.3**.

5.2.5.1 Photoanode fabrication

The doctor-blade technique was employed to print TiO_2 on a clean FTO glass. The films were then annealed at 350 °C for 30 min. The heat treatment was used to remove any residual organic components and to increase adhesion between the TiO_2 and the N-719 dye. For TiO_2 film sensitization, the dye was dispersed in methanol (3×10^{-4} M). The films were immersed in the dye solution for 10 s and then left overnight to dry under dark, ambient conditions.

5.2.5.2 Device assembly

The photoanode was placed on a clean flat surface, with the active layer facing upwards. The counter electrode was then placed on top of the photoanode with the active layer facing down. The two opposing FTO glass substrates were offset from one another and the Whatman filter paper was placed in-between to define the active area. The redox electrolyte solution is composed of 0.1 M lithium iodide, 0.05 M iodine, 0.1 M sodium iodide, 0.1 M potassium iodide, and 0.5 M 4-tert-butylpyridine, was dropped on the Whatman filter paper. The electrolyte was absorbed by the filter paper and drawn into the active area between the electrodes *via* capillary action. The assembled device was held together using foldback clips on either side of the device to create an even distribution A schematic illustration of the assembled device is depicted in **Figure 5.3**.

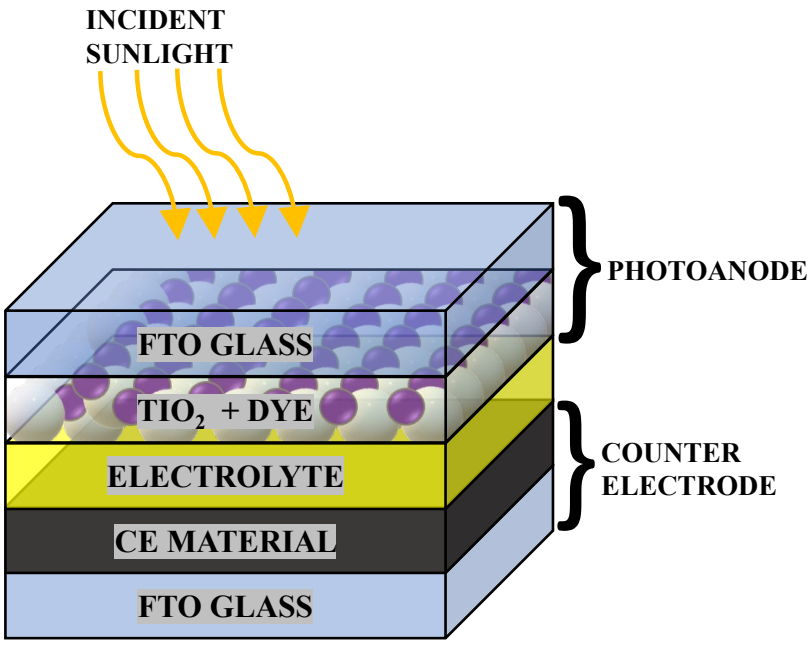


Figure 5.3: Structure of an assembled DSSC for current-voltage analysis of solar cell.

5.2.5 Characterization techniques

The morphology of the N-HCS/Cu_2S composites was evaluated using TEM and SEM performed on FEI Technai T12 TEM and using FEI Nova Nanolab 600 SEM respectively. Bonding modes of the composites were evaluated using XPS (X-ray photoelectron spectroscopy) analysis. Cyclic voltammetry curves for the electrocatalysis of the composites were carried out on the BASi epsilon E2 (1231) potentiostat at scan rates ranging from 25 mV/s to 100 mV/s. Electrochemical impedance spectroscopy (EIS) analysis was carried out in the dark and the measurements were obtained using a symmetrical cell 7 with two identical electrodes in the redox electrolyte used for DSSCs. Different open-circuit potentials for each CE material were used and the electrodes were analyzed between 100 kHz and 100 MHz. Tafel polarization analysis was conducted at a potential window of -1.5 to 1.5 V with a scan rate of 100 mVs^{-1}. To evaluate the fabricated DSSC devices, current-voltage (I-V) characteristic curves of the DSCCs were measured in ambient conditions using the HP 4141B source measure unit (SMU) under controlled illumination of 100 $mW.cm^{-2}$ (AM 1.5G).

5.3 Results and discussion

5.3.1 Morphology and structural properties of the composites

From the TEM and SEM micrographs obtained (**Figure 5.4**) for the 25 wt%, 50 wt%, and 75 wt% N-HCS, the morphology of the composite materials was analyzed. For the 25 wt% N-

HCS, cloud-like layers of the Cu_2S nanoparticles were observed covering the surface of the doped hollow carbon spheres as shown in **Figure 5.4(a)**. At 50:50 (50 wt%) more copper sulfide particles were observed on the carbon shells compared to the 75 wt% N-HCS composite. The Cu_2S nanoparticles were distributed on the surfaces of the carbon shells and the inside of the broken hollow carbon shells.

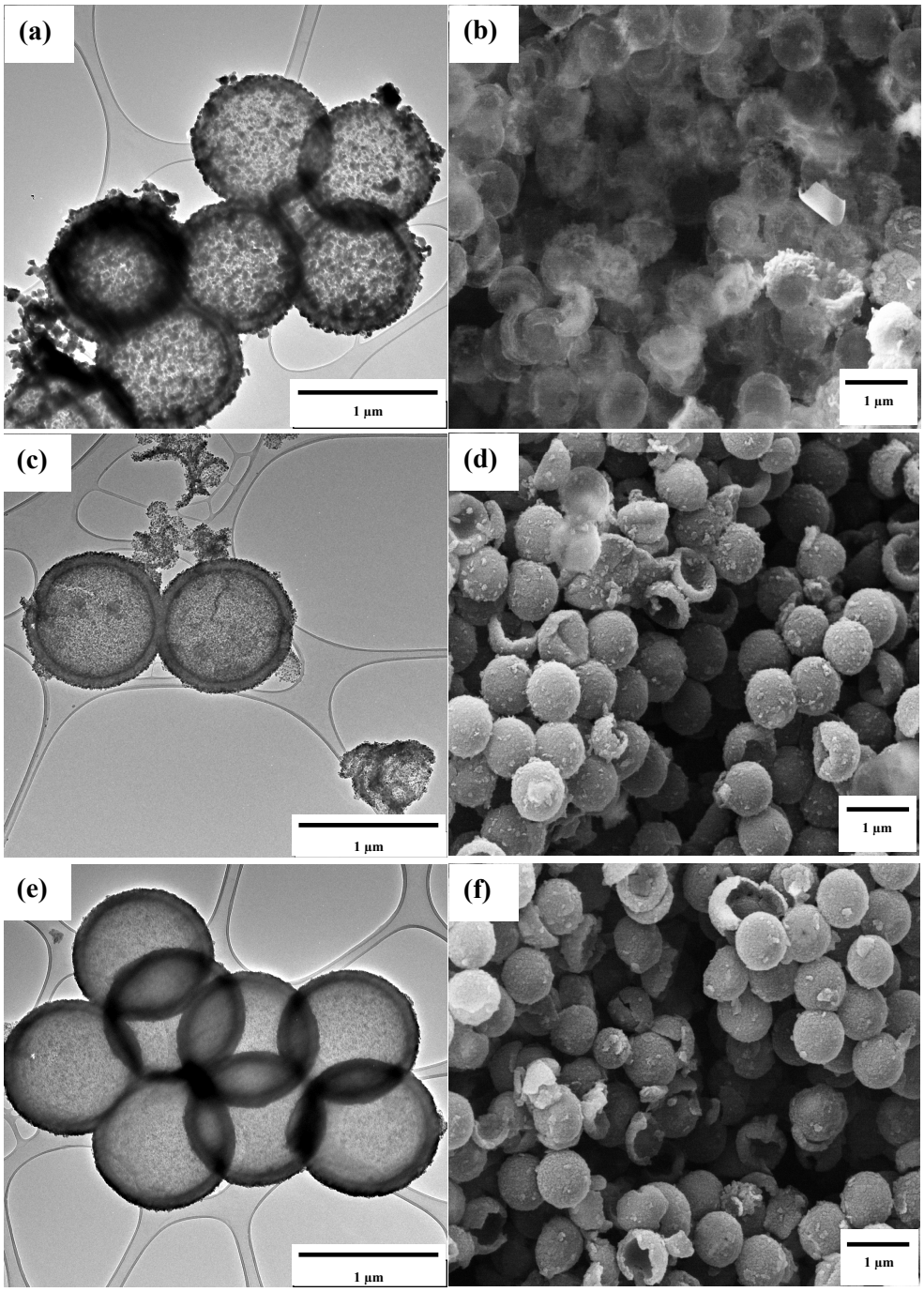


Figure 5.4: TEM micrographs of (a) 25 wt% N-HCS, (c) 50 wt% N-HCS and (e) 75 wt% N-HCS with their corresponding SEM micrographs (b, d, and f).

To analyze the composition of the synthesized composite materials, XPS was used. The spectra obtained for all the varied compositions of carbon and copper sulfide nanoparticles showed the presence of Cu, S, C, and O. The composite materials were synthesized with nitrogen-doped hollow carbon spheres and copper sulfide nanoparticles. However, the N 1s XPS spectrum was not obtained when analyzing the surface composition of the catalyst, this could be due to several factors. The presence of nitrogen defect sites increases the implantation of the transition metal sulfide particles [28], since Cu^{+} has strong cation -π bonding capabilities [29] an interaction occurs between the positively charged cation (Cu^{+}) and the negatively charged cloud of π systems from the closest pyrrolic or pyridinic nitrogen defects [30], [31]. Bulushev *et al.* found that nitrogen doping of mesoporous carbon led to strong interaction with copper species, stabilizing them to form nanoclusters [32], [33]. The Cu atoms coordinated more strongly to the pyrrolic and pyridinic nitrogen atoms present on the edge sites of carbon compared to graphitic-N and given that the N-HCS (**Chapter 3**) exhibited only pyrrolic-N and pyridinic-N in the carbon framework it would suggest that all the nitrogen sites are coordinated to the Cu species. A decrease in the nitrogen XPS signal due to the absorption of copper species through the cation -π bonding mechanism was also observed by Yu *et al.* [34].

XPS is a surface-sensitive technique that has an average analysis depth of 5 nm. The average thickness of the synthesized copper sulfide nanoparticles was found to be 5.98 nm. An oxidation layer is present on the surface of the material; this is confirmed by the O 1s spectrum. Therefore, nitrogen sites coordinated to the Cu_2S species are present in the deeper layers of the material resulting in the absence of the nitrogen XPS signal (**Figure 5.5**). The increase in surface concentrations of other elements such Cu, S, and O decreases the concentration of the nitrogen signal. This is due to the material having a layered structure as more elements are added (**Figure 5.6**). Another factor could be due to the high temperature used during composite preparations, the copper sulfide particles could merge into larger particles forming nanoclusters [35]. The Cu-Cu bonds and polysulfide species observed in the Cu 2p and S 2p XPS spectra suggests the formation of copper sulfide clusters [36], [37], this is also observed in the TEM micrographs obtained as a cloud-like layer is observed on the surface of the N-HCS (**Figure 5.4(b)**).

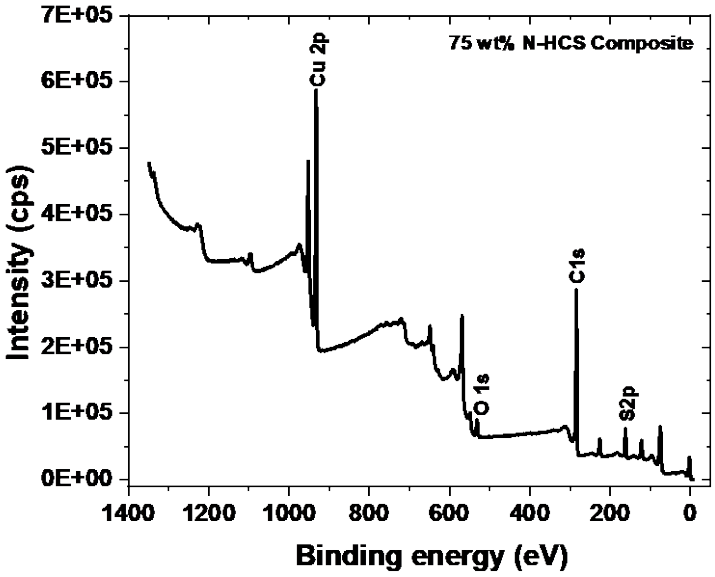


Figure 5.5: XPS survey spectrum for the 75 wt% N- HCS composite.

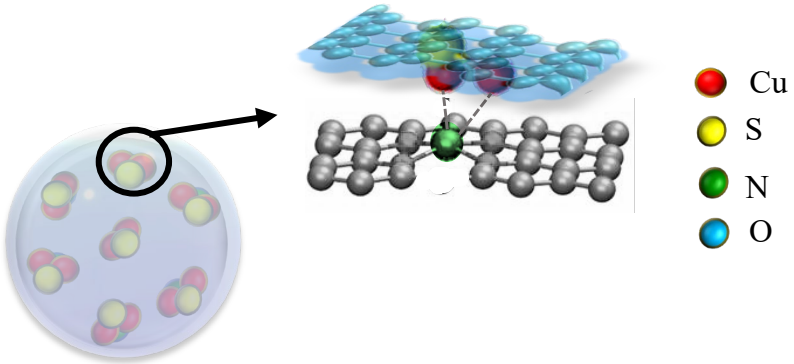


Figure 5.6: Schematic diagram showing the layering of elements in the composite material.

The C 1s, O 1s, Cu 2p, and S 2p XPS spectra are shown in **Figure 5.7**. The Cu 2p core level splits into 2 peaks, with the Cu $2p_{3/2}$ peak at 932.2 eV and the Cu $2p_{1/2}$ peak at 951.8 eV. The Cu $2p_{1/2}$ peak corresponds to Cu^{+} and Cu^{0} [38] and the peak at 932.2 eV is associated with Cu(I) in Cu_2S, Cu_2O, and Cu-Cu [39], [40]. There is no satellite peak present in between the two Cu 2p peaks indicating the absence of Cu^{2+} [41]. The S 2p spectra shows S $2p_{3/2}$ (161.3 eV) and S $2p_{1/2}$ (162.4 eV) peaks indicating the chemical binding state of Cu_2S [42], [43], with the 161.3 eV peak ascribed to S^{2-} species [44]. Each of the S $2p_{3/2}$ and S $2p_{1/2}$ peaks splits into doublets, the low binding energy (BE) peaks are due to sulfide atoms that are present in the bulk of the Cu_2S material and the high energy BE is due to surface sulfide atoms and polysulfide species which can be attributed to Cu_2S clusters [45]. The C 1s spectrum shows the C-C peak at 284.3 eV which corresponds to the carbon bonds present in the framework of the

hollow carbon spheres, the C-O and O-C=O peaks at 286.1 eV and 288.4 eV respectively can be assigned to the carboxylic groups of oleylamine or the oxidation layer present on the surface of the carbon [46]. The O 1s spectrum was deconvoluted into three peaks, C-O, C=O, and the metal oxide (Cu_2O) peaks which were observed at 531.5 eV, 533.2 eV, and 529.5 eV respectively. These groups represent the oxygen atoms present in hydroxyl and carboxylate groups which are present on the edges of carbon frameworks [47]. From the C1s spectra obtained there are no C-S or C=S bonds present suggesting that the sulfide atoms are not bonded to carbon to form the composite materials.

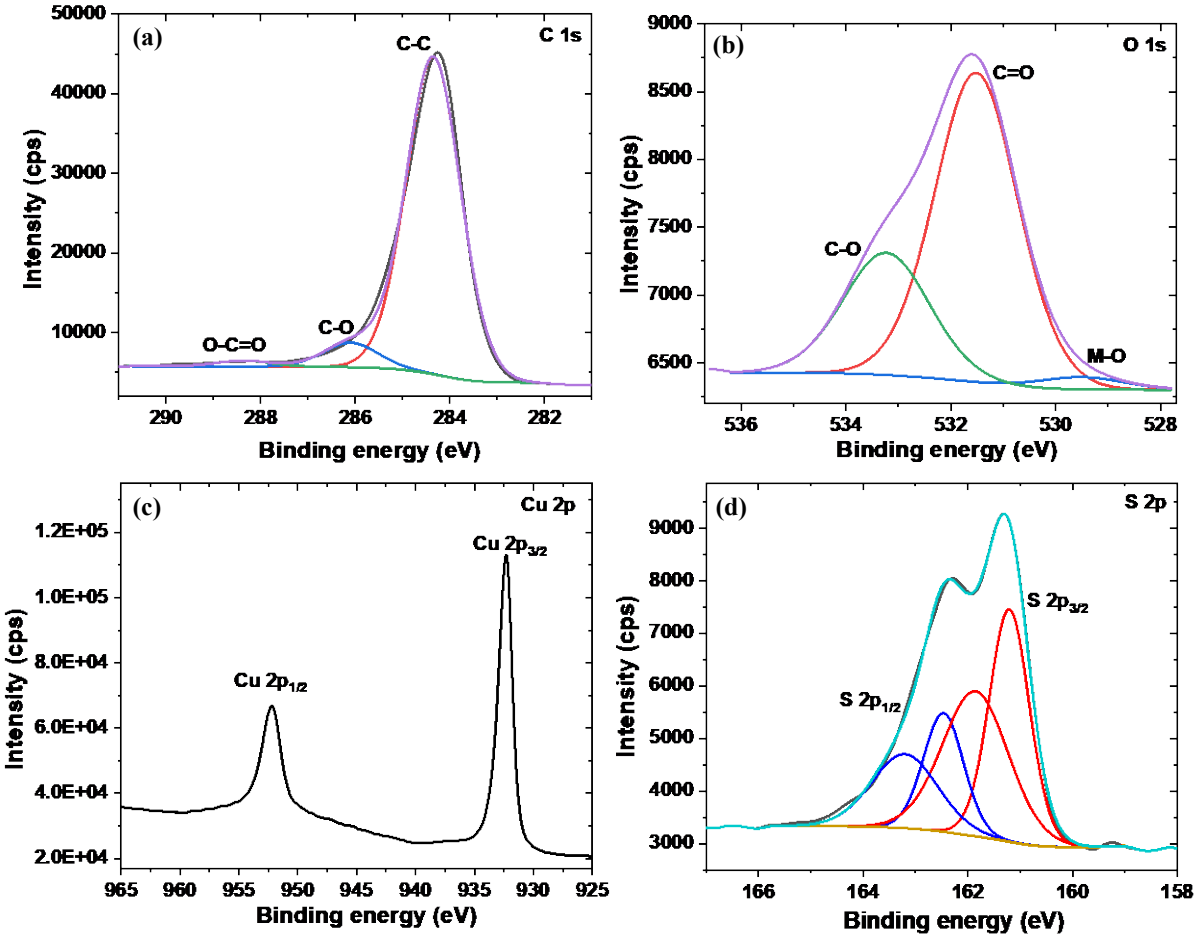


Figure 5.7: High resolution XPS spectra of (a) C 1s, (b) O 1s, (c) Cu 2p and (d) S 2p for the 75 wt% N-HCS composite.

The presence of each element varied according to the percentage compositions of each composite (**Table 5.1**). C was be attributed to carbon from the hollow carbon spheres, O was due to the oxidation of carbon and copper (Cu_2O) as well as the layer of oxygen present on the surface of the composite. The Cu and S spectra were attributed to the copper sulfide nanoparticles.

Table 5.1: Summary of the atomic composition stoichiometric assignments obtained from the fitting of the XPS spectra reported in Fig. 5.3 for the 75 wt%, 50 wt%, and 25 wt% N-HCS composites.

Sample	Elements	Atomic %	Peak Binding Energy (eV)	Assignments	Assignment %
75 wt% N-HCS	C	75.5	284.3	C-C	69.8
			286.1	C-O	4.4
			288.4	O-C=O	1.3
	Cu	14	932.3	(CuS, Cu_2S, Cu_2O, Cu-Cu)	12.3
			956.3	Cu 2p	1.7
	O	3.3	531.5	C-O	2.1
			533.2	C=O	0.8
			529.5	M-O	0.1
	S	7.3	161.2	S $2p_{3/2}$ (Sulfide)	4
			161.9	S $2p_{1/2}$ (Sulfide)	4.2
50 wt% N-HCS	C	58.5	284,5	C-C	56
			286,1	C-O	3,4
			288,7	O-C=O	1,1
	Cu	23.7	932,3	(CuS, Cu_2S, Cu_2O, Cu-Cu)	20.3
	O	3.2	533	C-O	5,3
			529,5	C=O	1
			161,3	M-O	0,2
	S	14.6	161,9	S $2p_{3/2}$ (Sulfide)	6.5
			284,5	S $2p_{1/2}$ (Sulfide)	6.2
25 wt% N-HCS	C	27.3	284,4	C-C	28.6
			286,1	C-O	3.3
			288,4	O-C=O	1.1
	Cu		932,3		
		42.4		(CuS, Cu_2S, Cu_2O, Cu-Cu)	37.2
	O	3.1	531,4	C-O	6,1
			532,8	C=O	1,1
			529,9	M-O	0,6
	S	27.2	161,2	S $2p_{3/2}$ (Sulfide)	5,7
			161,8	S $2p_{3/2}$ (Sulfide)	5,3
			162,5	S $2p_{1/2}$ (Sulfide)	5,7
			163	S $2p_{1/2}$ (Sulfide)	5,3

5.3.2 Electrocatalytic activity of the Counter electrode composite materials

5.3.2.1 Cyclic voltammetry and capacitive current

To investigate the stability and electrochemical catalytic properties of the synthesized materials and different composites, cyclic voltammetry (CV) was used. The reduction of the I_3^- / I^- redox couple was measured using different scan rates of 100, 75, 50, and 25 mV/s. The stability of prepared composites, Cu_2S, N-HCS, and Pt as counter electrodes in the iodide/triiodide electrolyte was analyzed by performing ten scans for each material. Pt was used as the control sample and two pairs of the oxidation and reduction peaks were observed. The top and bottom left-hand side peaks of the CV plots represent the redox reaction of I_3^- / I^- which influences the photovoltaic performance of DSSCs as the reduction of the electrolyte correlates to the catalytic ability of the CE materials [5], [48]. Peaks on the right-hand side represent the redox reaction of I_3^- / I_2 [49], [50], this reaction has very little effect on the performance of DSSCs therefore the left-side peaks of the CV curves of each material were studied. The Pt anodic peaks were found at 0.42 V and 0.90 V, reduction peaks at 0.18 V and 0.75 V and the peak separation between the left anodic and cathodic peaks (ΔE_p) is 240 mV (**Figure 5.8**). The Pt counter electrode showed electrochemical stability and reproducibility for the scan rates used, as the CV curves were not distorted regardless of the number of scans or scan rate used.

The current density decreases as the scan rate also decreases and the left side reduction peak shifts to the right from 0.18 V to 0.21 V as the scan rate decreases, the peaks positive shift suggests that the reduction reaction occurs at lower potentials when the scan rate is low. Scan rate is an important parameter as high scan rates lead to the reduction of the diffusion layer therefore higher currents are detected. In reversible electron transfer reactions involving the redox elements that diffuse freely, the Randles−Sevcik equation states that there is a positive correlation between the peak current (i_p) and the square root of scan rate υ (Equation. 1) [22]. The number of electrons transferred during the redox reaction is denoted by n, surface area (A) of the electrode, D_o is the diffusion coefficient of the oxidized electrolyte, and C^0 is the bulk concentration of the analyte [51].

$$i_\mathrm{p} = 0.446\, nFAC^0 \left(\frac{nFvD_o}{RT}\right)^{1/2} \qquad (1)$$

From the equation, we can determine if there is electrochemical reversibility of the electron transfer process if peak-to-peak separation changes with scan rate. Comparing the Cu_2S (**Figure 5.8(b)**) and N-HCS (**Figure 5.8(c)**) counter electrodes. The current densities of N-HCS increase with an increase in scan rate. At 100 mV/s N-HCS has a lower current density (J_{red} – left-side) of 0.017 A/cm^2 compared to 11.732 A/cm^2 for Cu_2S. Also, its ΔE_p is lower (275 mV) than that of N-HCS (564 mV). Peak-to-peak separation is another parameter that can be used to evaluate the catalytic activity of the CE material since ΔE_p has a negative correlation with the electrochemical rate constant for the redox reactions, this can be used to analyze the reversibility of the electrolyte redox processes [52], [53]. The electrocatalytic performance of the CE material is better at lower ΔE_p values [54], therefore an ideal material would have a high current density for reduction peak [50], [55], and a low ΔE_p value. At 100 mV/s Cu_2S CE shows great electrocatalytic activity for the reduction of I_3^-, as the scan rates decrease the CV curves degrade. Insufficient redox reactions of the electrolyte occur as the CV curves do not exhibit the oxidation-reduction peak pairs, only the oxidation peaks are observed. Therefore, N-HCS shows better reproducibility and stability as the CV curves do not distort. Chung *et al.* found that compared to Cu-deficient CEs, the Cu-rich CEs are unstable as they are easily oxidized due to the oxygen layer present on the surface [56], [57]. The stability of N-HCS-CE and the good electrocatalytic properties found at 100 mV/s for Cu_2S, validates that the preparation of a composite with these two materials could produce an ideal CE material.

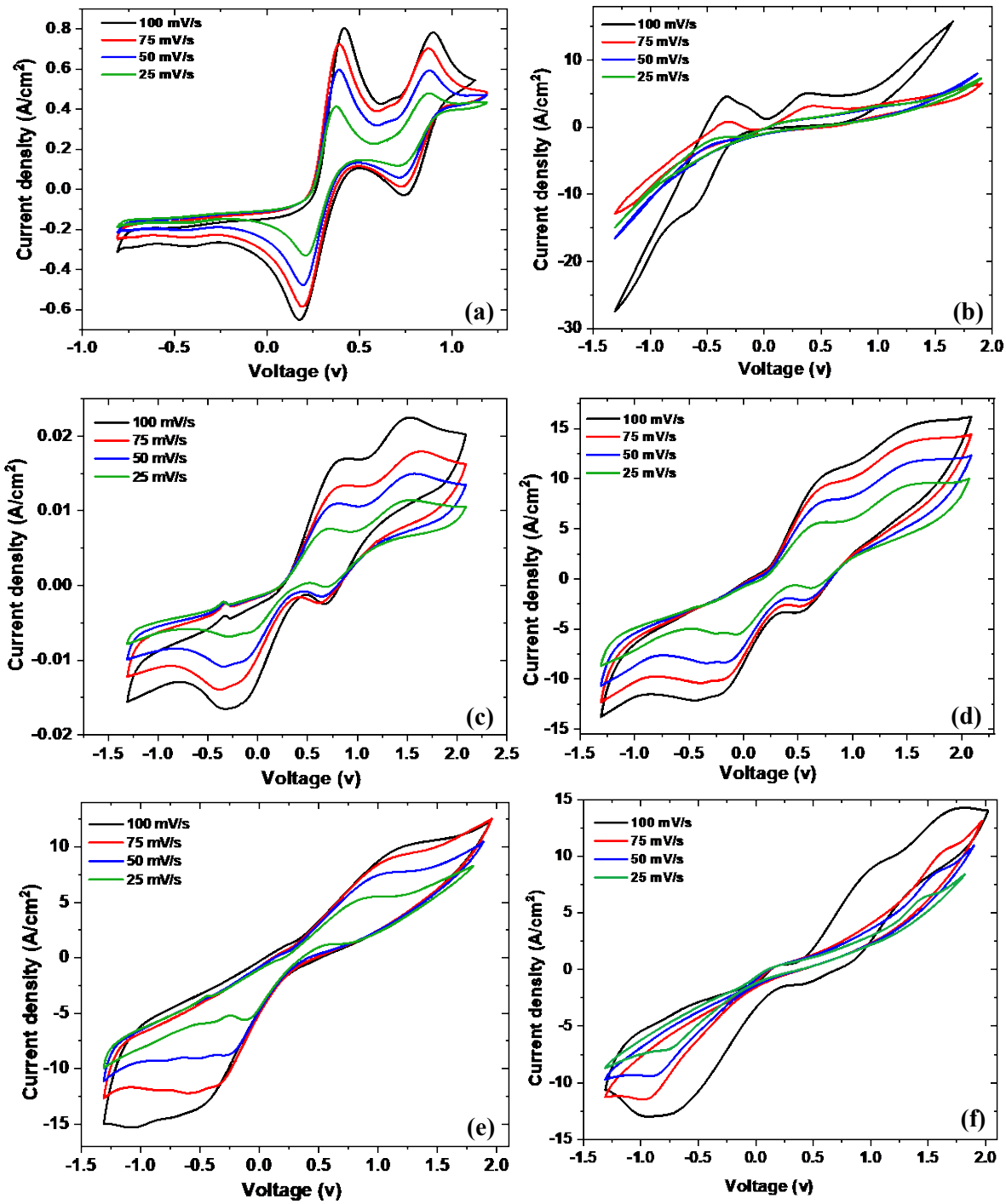


Figure 5.8: Cyclic voltammograms for (a) Pt-CE, (b) Cu2S (c) N-HCS, (d) 75wt% N-HCS, (e) 50wt% N-HCS and (f) 25 wt% N-HCS counter electrode at various scan rate after 10 scans.

This research aimed to prepare a N-HCS/Cu_2S composite that could substitute the Pt-CE in DSSCs. From the CV curves obtained 75 wt% N-HCS composite has a peak current density J_{red} (left-side) that was found to be 11.850 A/cm^2 with a ΔE_p value of 418 mV, 50 wt% N-HCS

composite has 13.816 A/cm^2 with a ΔE_p value of 617 mV and 25 wt% N-HCS composite has 12.903 A/cm^2 with ΔE_p 186 mV (**Table 5.2**). All composites (**Figure 5.8**) exhibited high peak current densities J_{red} (left-side) compared to Pt-CE (2.310 A/cm^2) and N-HCS (0.017 A/cm^2). Suggesting that the incorporation of Cu_2S to N-HCS enhanced the electrocatalytic activity of the CE material producing material that has a better ability to reduce the triiodide/iodide electrolyte compared to Pt-CE. Analyzing the ΔE_p and CV curves of the composites, 25 wt% N-HCS composite showed a lower ΔE_p value than Pt (240 mV) suggesting that it has a better electrocatalytic ability between the composites. Since it has a high current peak density and low ΔE_p value, it is a suitable candidate to substitute Pt as a CE in DSSC, this is due to the properties of both N-HCS and Cu_2S (**Chapter 3 and 4**).

The doped hollow carbon spheres incorporation produced CV plots with defined redox peaks at different scan rates, Cu_2S nanoparticles reduced the peak-to-peak separation and increased the peak density of N-HCS. However, the CV curves show that the material is unstable after 10 scans, at low scan rates. Some of the peaks diminish at lower scan rates, therefore, reducing the redox ability of the material. Using the CV data obtained, the capacitive current densities for the composites, Pt, Cu_2S, and N-HCS were plotted against the square root of scan rate to determine their relationships. As the scan rate increased the current densities increased, with 75 wt% N-HCS exhibiting the highest capacitive current and Pt had the lowest. The synthesized CE materials (N-HCS and Cu_2S) and their composites all exhibit high electrochemical double layer capacitive current (**Figure 5.9**) suggesting that they have high electrocatalytic surface active. The incorporation of Cu_2S nanoparticles with N-HCS increased its capacitive current making it a better CE material. Given that 25 wt% N-HCS has a high current peak density, low ΔE_p value, and high electrochemical double layer capacitive current compared to Pt suggests that it is the better performing composite.

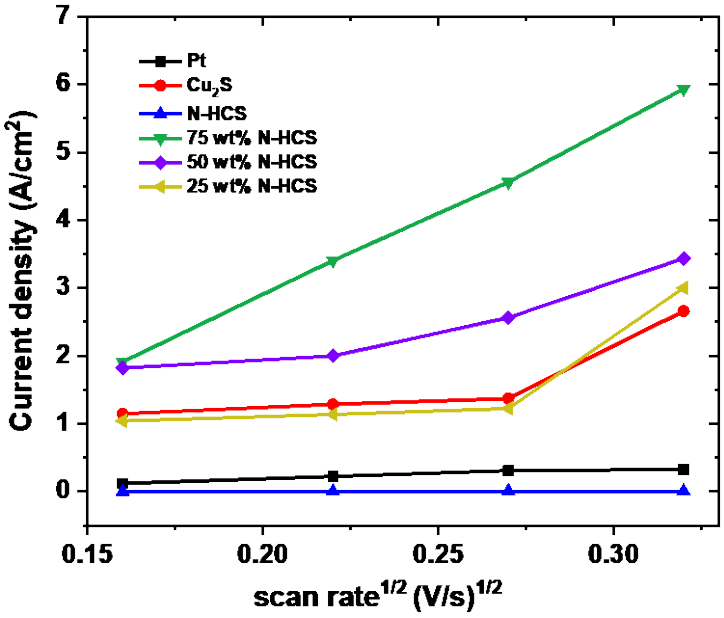


Figure 5.9: Capacitive current versus scan rate for the prepared composites, Pt, Cu_2S, and N-HCS electrocatalysts.

Table 5.2: Summary of composites and Pt CE current densities and their peak-to-peak separations.

Sample	Current Density (J_{red}) (A/cm^2)	Peak to Peak separation (ΔE_p) (mV)
Pt	2.310	240
75 wt % N-HCS Composite	11.850	418
50 wt% N-HCS Composite	13.816	617
25 wt % N-HCS Composite	12.903	186

Electrochemical impedance spectroscopy was used to assess the ability of the CE materials to transfer charge to the triiodide electrolyte. The Nyquist plots of Pt, N-HCS, Cu_2S, 75 wt% N-HCS, 50 wt% N-HCS, and 25 wt% N-HCS and their equivalent circuit is shown in **Figure 5.10**. The circuit shows four main components, series resistance R_s, charge transfer resistance R_{ct} at the electrolyte/CE interface, Warburg impedance Z_w which is used to assess the impedance of the triiodide/iodide couple in the electrolyte, and the double layer capacitance C_{dl} which represents the charge storage capacities of the CE materials. Warburg impedance is found in the low-frequency region and represented by the line that is at a 45° to the Nyquist

semicircle. The crucial parameters that represent the electrocatalytic activity of the CE materials are R_s and R_{ct}. From the data shown in **Table 5.3** 75 wt% N-HCS has the lowest R_s therefore, it adheres better to the conductive fluorine-doped tin oxide (FTO) substrate compared to the other materials. The lower the R_{ct} the better the electrocatalytic activity, from the data obtained 75 wt % N-HCS composite (29 Ω) has better catalytic activity and Cu_2S (6007Ω) has the lowest catalytic activity (181 Ω). The electrocatalytic activity trend obtained from the results is 75 wt% N-HCS > N-HCS > 50 wt% N-HCS > Pt > 25 wt% N-HCS > Cu_2S. The materials with high carbon content and therefore, higher nitrogen doping (75 wt% N-HCS, N-HCS, 50 wt% N-HCS) exhibited the lowest the R_{ct} values. This can be attributed to the nitrogen and carbon content improving the electrical conductivity [58], [59].

The N-HCS Nyquist plot shows a semicircle with a low R_{ct}, the small diameter can be ascribed to porous carbon shell and the presence of nitrogen. These characteristics improve the charge at the interfaces and enhance the electrical conductivity of the material. This is confirmed by the work done by Xu *et al*. who noted changes in Nyquist plots diameter due to the porous nature and nitrogen doping of the HCSs [59]. The 50 wt% N-HCS Nyquist plot shows a spike in the low-frequency region and a depressed semicircle, this is related to the charge transfer resistance and the double layer capacitance at the CE/electrolyte interface [58], [60]–[62]. The inclined line exhibited in the 75 wt% N-HCS Nyquist plot in the low-frequency region, can be related to the Warburg resistance (Z_w) [63].

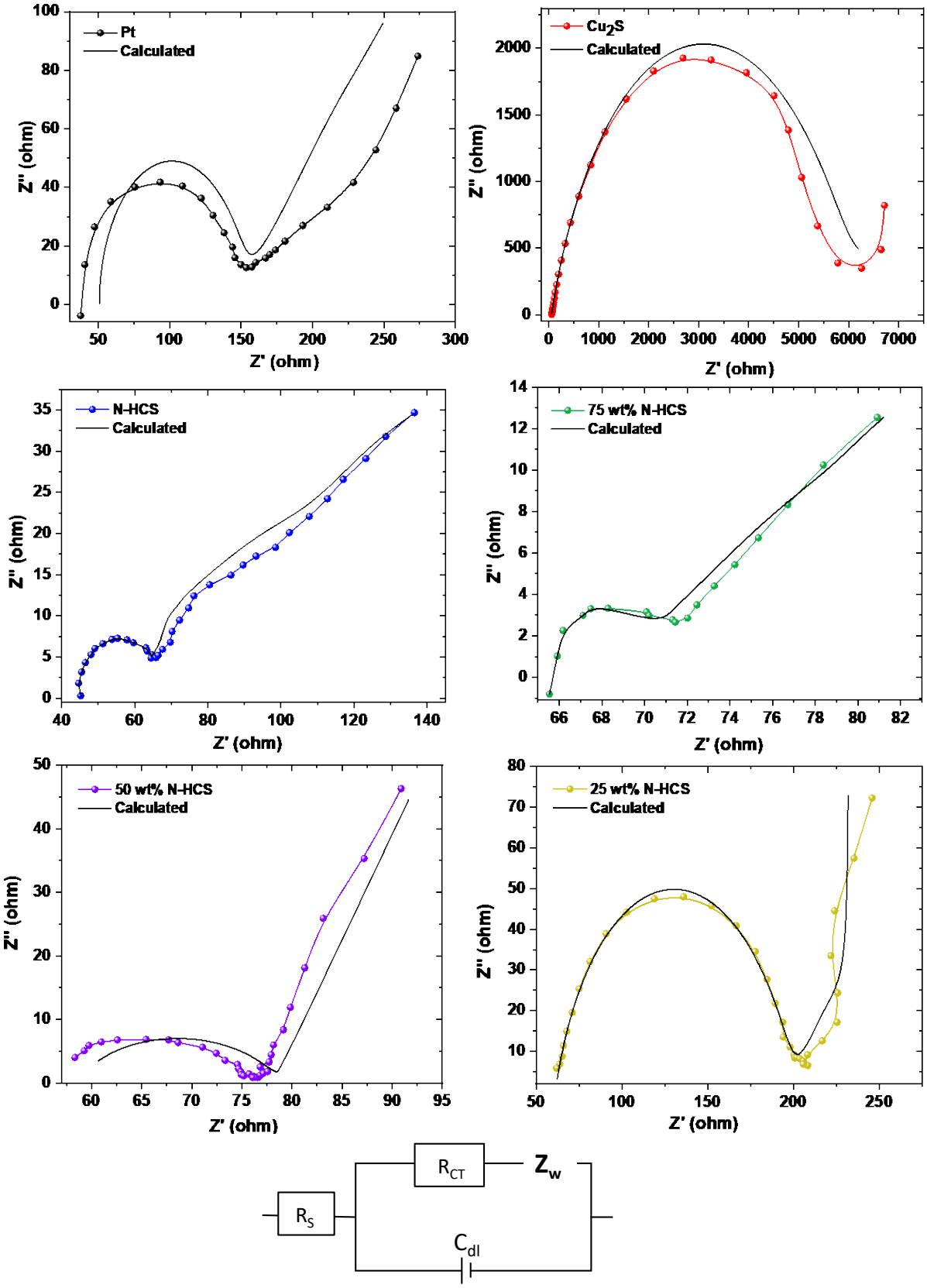


Figure 5.10: Nyquist plots of EIS for the symmetric cells with their electrochemical equivalent circuit for Pt, Cu_2S, N-HCS, 75 wt% N-HCS, 50 wt% N-HCS, and 25 wt% N-HCS.

The Tafel polarization curves (**Figure 5.11**) were analyzed to determine the ability of the CE materials to reduce I_3^- to I^-. Catalytic activities of the CEs are dependent on the exchange current density (J_0) and limiting diffusion current (J_{lim}). J_0 increases as the slope of the anodic and cathodic current increases suggesting good electrocatalytic activity at high J_0 values. A high diffusion of ions onto the CE materials suggest better catalytic ability of the materials. R_{ct} and J_0 are inversely proportional. Therefore, a CE material that has a high J_0 value, high J_{lim} and low R_{ct} exhibits better electrocatalytic performance. The 75 wt% N-HCS composite has the highest J_{lim} and the least negative J_0 therefore it has the better electrocatalytic activity. The trend for the electrocatalytic performance according to the J_0 values, follows the same trend as the EIS results. The 75 wt% N-HCS composite is the better performing electrocatalyst and Cu_2S is the lowest. However, the trend changes slight for J_{lim} as depicted in (**Table 5.3**), the order is as follows 75 wt% N-HCS > Pt > 50 wt% N-HCS > N-HCS > 25 wt% N-HCS > Cu_2S. Although 75 wt% N-HCS still exhibits better ion diffusion and Cu_2S has the lowest diffusion coefficient. The results for J_{lim} show that Pt has better ion adsorption and diffusion compared to the 50 wt% N-HCS and N-HCS. Since the 75 wt% N-HCS composite has the highest J_0 value, lowest R_{ct} and highest J_{lim}, it is the better performing CE electrocatalyst.

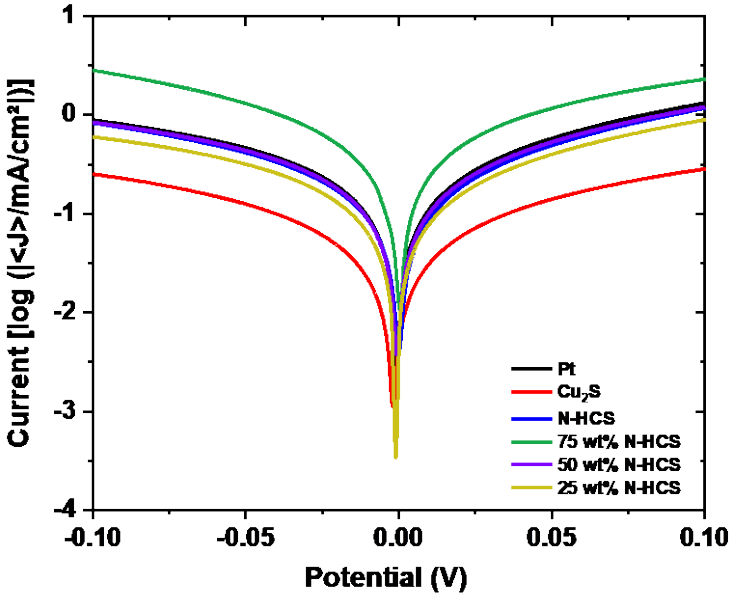


Figure 5.11: Tafel plot of the Pt and the synthesized materials: Cu_2S, N-HCS, 75 wt% N-HCS, 50 wt% N-HCS, and 25 wt% N-HCS.

Table 5.3: Electrochemical measurements obtained from EIS and Tafel polarization curves for Pt and the synthesized materials: Cu_2S, N-HCS, 75 wt% N-HCS, 50 wt% N-HCS, and 25 wt% N-HCS

Sample	R_s (ohm)	R_{ct} (ohm)	Log J_0 (mA/cm^2)	Log J_{lim} (mA/cm^2)
Pt	51	98	-3.88	0.13
Cu_2S	56	6007	-5.67	- 0.54
N-HCS	34	39	-3.48	0.07
75 wt % N-HCS Composite	29	20	-3.19	0.37
50 wt% N-HCS Composite	59	71	-3.74	0.09
25 wt % N-HCS Composite	61	135	- 4.02	- 0.04

The data obtained from the CV curves suggested that the 25 wt % N-HCS composite was a better catalyst between the composites as it has a high current peak density and low ΔE_p. However, the capacitive current linear plot suggested that the 75 wt % N-HCS composite had the highest electrochemical double layer capacitive current. From the EIS measurement, the Nyquist plots showed that the 75 wt % N-HCS composite has the better adhesion to the conductive substrate as it has the lowest R_s value. From the EIS and polarization analysis, the 75 wt% N-HCS composite has the highest J_0 value, lowest R_{ct} and highest J_{lim}, suggesting that it is the better performing CE electrocatalyst. These results suggest that both the 25 wt% N-HCS and 75 wt% N-HCS composite exhibit good electrocatalytic properties. Therefore to determine the more suitable Pt CE material substitute. A DSSC cell was fully fabricated for both materials to determine which electrocatalyst exhibited better catalytic performance. Current-voltage measurements were used to investigate the photovoltaic performances of the CE materials. The obtained data is depicted in **Figure 5.12**. From **Table 5.4** it can be concluded that the 75 wt % N-HCS composite has better photovoltaic properties as it showed the highest efficiency (0.60 %) and J_{sc} value (0.158 mA/cm^2). This can be ascribed to the combination of the two materials in the composite as the individual materials did not show the same catalytic ability. The porous nature and nitrogen doping of the hollow carbon spheres and the large surface area of the copper sulfide particles aided in the electrocatalytic reaction.

The 25 wt % N-HCS composite has the lowest conversion efficiency and short-circuit current density compared to Pt. This can be attributed to the small copper sulfide particles blocking the porous sites of N-HCS as the particles envelop the hollow carbon spheres as shown in the TEM and SEM images in **Figure 5.4**. Although the 75 wt % N-HCS composite exhibited the best adhesion to the conductive substrate, it showed the lowest FF value. This can be ascribed to the series resistance due to the FTO substrate, low shunt resistance [64], or the thickness of the TiO_2 increasing the distance between the photoanode and the counter electrode [65].

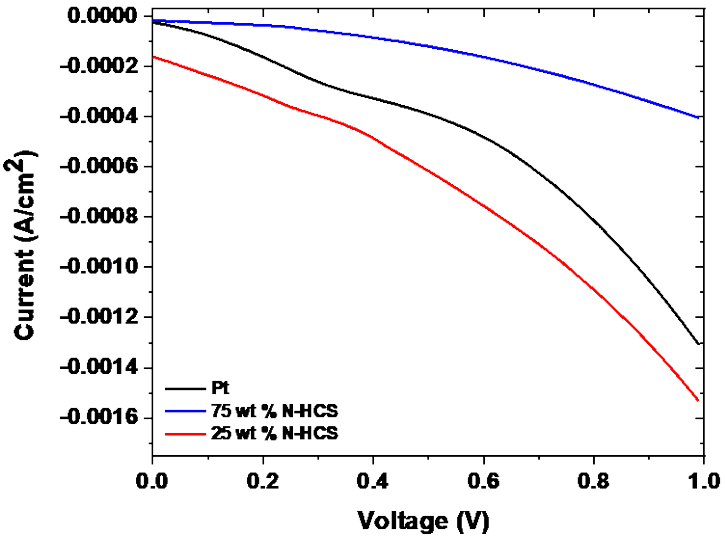


Figure 5.12: Current-voltage characteristic curves for the DSSCs of Pt, 75 wt% N-HCS, and 25 wt% N-HCS.

Table 5.4: Current-voltage measurements for the DSSCs of Pt, 75 wt% N-HCS, and 25 wt% N-HCS

Sample	DSSC J_{sc} (mA/cm^2)	V_{co} (V)	FF	PCE %
Pt	0.023	0.99	14.96	0.49
75 wt % N-HCS Composite	0.158	0.99	2.69	0.60
25 wt % N-HCS Composite	0.019	0.99	3.89	0.11

5.4 Conclusion

From the TEM and XPS results obtained, there was successful preparation of the N-HCS-Cu_2S composite as both hollow carbon spheres and the copper sulfide nanoparticles we observed. CV plots showed that each of the materials' catalytic and peak properties was improved by the incorporation of the other. The 25 wt% N-HCS composite showed that, although it was unstable at low scan rates due to oxidation, it had better electrocatalytic activity and the ability to reduce I_3^- to I^- at 100 mV/s compared to Pt-CE. The high capacitive current in comparison to Pt suggests that 25 wt% N-HCS and 75 wt% N-HCS composites have higher electrocatalytic active surface area. The catalytic ability of the 25 wt% N-HCS composite can be attributed to the surface area provided by the copper sulfide particles. However, because of the low carbon content of the material, the composite does not exhibit the stability and resistance to corrosion from the triiodide/iodide electrolyte. The 75 wt% N-HCS has a high current peak density, high electrochemical double layer capacitive current, low R_s, low R_{ct}, the highest J_0 value, the highest J_{lim}, high efficiency of 0.60 %, and high J_{sc} value of 0.158 mA/cm^2. This composite catalyst also showed good catalytic ability from the CV data obtained, as it exhibited high peak current density and good stability, given that the CV curves did not distort over time and at different scan rates. However, the presence of an oxidation layer will limit its catalytic abilities at lower scan rates over time. Compared to Pt, 75 wt% N-HCS is the better performing composite and can be used as a viable substitute for platinum. Its low FF can be rectified by using other conductive substrates. The spin coating technique or sputter coating can be used to deposit a thin layer of TiO_2 onto the conductive FTO. This would reduce the separation between the electrodes, increase the interaction and FF value. Overall the DSSCs need to be optimized, however the trend is telling.

References

[1] G. Shimoga, E. J. Shin, and S. Y. Kim, "Flexible Vibrotactile Actuator Based on Soft PVC Gel Embedded Polyaniline/Silicon Dioxide Nanoparticles," *IEEE Access*, vol. 8, pp. 122057–122064, 2020.

[2] S. H. Mir, L. A. Nagahara, T. Thundat, P. Mokarian-Tabari, H. Furukawa, and A. Khosla, "Review—Organic-Inorganic Hybrid Functional Materials: An Integrated Platform for Applied Technologies," *J. Electrochem. Soc.*, vol. 165, no. 8, pp. B3137–B3156, 2018.

[3] V. P. Ananikov, “Organic-inorganic hybrid nanomaterials,” *Nanomaterials*, vol. 9, no. 9, 2019.

[4] S. Singh *et al.*, “Hybrid Organic–Inorganic Materials and Composites for Photoelectrochemical Water Splitting,” *ACS Energy Lett.*, vol. 5, no. 5, pp. 1487–1497, 2020.

[5] X. Luo, Y. Zhang, and S. H. Kim, “Incorporation of Nanostructured Carbon Composite Materials into Counter Electrodes for Highly Efficient Dye-Sensitized Solar Cells,” *Nanoscale Res. Lett.*, vol. 13, pp. 1–10, 2018.

[6] Y. Chujo, “Organic—inorganic hybrid materials,” *Curr. Opin. Solid State Mater. Sci.*, vol. 1, no. 6, pp. 806–811, 1996.

[7] Y. Y. Yu and C. H. Yang, “Preparation and application of organic-inorganic nanocomposite materials in stretched organic thin film transistors,” *Polymers (Basel).*, vol. 12, no. 5, 2020.

[8] Y. Zhang, P. Wang, T. Zhang, and B. Gou, “High-Efficiency Dye-Sensitized Solar Cells Based on Kesterite Cu2ZnSnSe4 Inlaid on a Flexible Carbon Fabric Composite Counter Electrode,” *ACS Omega*, vol. 5, no. 38, pp. 24898–24905, 2020.

[9] W. Du *et al.*, “Biological cell template synthesis of nitrogen-doped porous hollow carbon spheres/MnO2 composites for high-performance asymmetric supercapacitors,” *Electrochim. Acta*, vol. 296, pp. 907–915, 2019.

[10] G. Yue *et al.*, “Synthesis of MoIn2S4@CNTs Composite Counter Electrode for Dye-Sensitized Solar Cells,” *Nanoscale Res. Lett.*, vol. 15, no. 1, 2020.

[11] S. Thomas, T. G. Deepak, G. S. Anjusree, T. A. Arun, S. V. Nair, and A. S. Nair, “A review on counter electrode materials in dye-sensitized solar cells,” *J. Mater. Chem. A*, vol. 2, no. 13, pp. 4474–4490, 2014.

[12] M. Aftabuzzaman and H. K. Kim, “Porous Carbon Materials as Supreme Metal-Free Counter Electrode for Dye-Sensitized Solar Cells,” *Emerg. Sol. Energy Mater.*, no. August, 2018.

[13] E. Meyer, R. Taziwa, D. Mutukwa, and N. Zingwe, “A review on the advancement of ternary alloy counter electrodes for use in dye-sensitised solar cells,” *Metals (Basel).*, vol. 8, no. 12, 2018.

[14] A. Kay and M. Grätzel, “Low cost photovoltaic modules based on dye sensitized nanocrystalline titanium dioxide and carbon powder,” *Sol. Energy Mater. Sol. Cells*, vol. 44, no. 1, pp. 99–117, 1996.

[15] M. Wu, Y. nan Lin, H. Guo, W. Li, Y. Wang, and X. Lin, “Design a novel kind of

open-ended carbon sphere for a highly effective counter electrode catalyst in dye-sensitized solar cells," *Nano Energy*, vol. 11, no. 2015, pp. 540–549, 2015.

[16] J. Wu *et al.*, "Counter electrodes in dye-sensitized solar cells," *Chem. Soc. Rev.*, vol. 46, no. 19, pp. 5975–6023, 2017.

[17] C. H. Lin, C. H. Tsai, F. G. Tseng, C. C. M. Ma, H. C. Wu, and C. K. Hsieh, "Three-dimensional vertically aligned hybrid nanoarchitecture of two-dimensional molybdenum disulfide nanosheets anchored on directly grown one-dimensional carbon nanotubes for use as a counter electrode in dye-sensitized solar cells," *J. Alloys Compd.*, vol. 692, pp. 941–949, 2017.

[18] K. Subalakshmi, K. A. Kumar, O. P. Paul, S. Saraswathy, A. Pandurangan, and J. Senthilselvan, "Platinum-free metal sulfide counter electrodes for DSSC applications: Structural, electrochemical and power conversion efficiency analyses," *Sol. Energy*, vol. 193, no. June, pp. 507–518, 2019.

[19] M. Wu and T. Ma, "Platinum-free catalysts as counter electrodes in dye-sensitized solar cells," *ChemSusChem*, vol. 5, no. 8, pp. 1343–1357, 2012.

[20] J. Theerthagiri, Senthil, M. Jagannathan, and T. Maiyalagan, "Recent Progress in Non-Platinum Counter Electrode Materials for Dye-Sensitized Solar Cells," *ChemElectroChem*, vol. 2, Apr. 2015.

[21] Y. Guo *et al.*, "Copper(I) sulfide: a two-dimensional semiconductor with superior oxidation resistance and high carrier mobility," *Nanoscale Horizons*, vol. 4, no. 1, pp. 223–230, 2019.

[22] N. Elgrishi, K. J. Rountree, B. D. McCarthy, E. S. Rountree, T. T. Eisenhart, and J. L. Dempsey, "A Practical Beginner's Guide to Cyclic Voltammetry," *J. Chem. Educ.*, vol. 95, no. 2, pp. 197–206, 2018.

[23] G. Zhuang, H. Liu, and X. Chen, "High-performance dye-sensitized solar cells using Ag-doped CoS counter electrodes," *RSC Adv.*, vol. 8, no. 34, pp. 18792–18799, 2018.

[24] L. Bay, K. West, B. Winther-Jensen, and T. Jacobsen, "Electrochemical reaction rates in a dye-sensitised solar cell - The iodide/tri-iodide redox system," *Sol. Energy Mater. Sol. Cells*, vol. 90, no. 3, pp. 341–351, 2006.

[25] J. X. J. Zhang and K. Hoshino, *Fundamentals of nano/microfabrication and scale effect*. 2019.

[26] V. Slyke, "Organic Light-emitting Diodes," 1963.

[27] M. R. Balboul and A. Abdel-Galil, "Fabrication and performance of dye sensitized solar cell based on spin coated ZnS nanoparticles," *Appl. Phys. A Mater. Sci. Process.*,

vol. 125, no. 12, pp. 1–10, 2019.

[28] W. J. Lee, U. N. Maiti, J. M. Lee, J. Lim, T. H. Han, and S. O. Kim, “Nitrogen-doped carbon nanotubes and graphene composite structures for energy and catalytic applications,” *Chem. Commun.*, vol. 50, no. 52, pp. 6818–6830, 2014.

[29] and J. H. Herbert, Bruce E, Dongqiang Zhu, Mark A. Schlautman, Elizabeth R. Carraway, “Cation-π bonding: A new perspective on the sorption of polycyclic aromatic hydrocarbons to mineral surfaces,” no. May 2014, 2004.

[30] A. S. Mahadevi and G. N. Sastry, “Cation-π interaction: Its role and relevance in chemistry, biology, and material science,” *Chem. Rev.*, vol. 113, no. 3, pp. 2100–2138, 2013.

[31] V. A. Cardozo–Mata *et al.*, “Chemical interaction between nitrogen-doped graphene defects and a copper (1 1 1) surface: Effects on water molecule adsorption,” *Appl. Surf. Sci.*, vol. 502, no. June 2019, p. 144149, 2020.

[32] D. A. Bulushev *et al.*, “Copper on carbon materials: Stabilization by nitrogen doping,” *J. Mater. Chem. A*, vol. 5, no. 21, pp. 10574–10583, 2017.

[33] H. Yorita, K. Otomo, H. Hiramatsu, A. Toyama, T. Miura, and H. Takeuchi, “Evidence for the cation-π interaction between Cu2+ and tryptophan,” *J. Am. Chem. Soc.*, vol. 130, no. 46, pp. 15266–15267, 2008.

[34] W. Yu, F. Lian, G. Cui, and Z. Liu, “N-doping effectively enhances the adsorption capacity of biochar for heavy metal ions from aqueous solution,” *Chemosphere*, vol. 193, pp. 8–16, 2018.

[35] G. Wei, J. S. Wainright, and R. F. Savinell, “Catalytic activity for oxygen reduction reaction of catalysts consisting of carbon, nitrogen and cobalt,” *J. New Mater. Electrochem. Syst.*, vol. 3, no. 2, pp. 121–129, 2000.

[36] K. Wrighton-Araneda, R. Ruby-Figueroa, H. Estay, and D. Cortés-Arriagada, “Interaction of H2O with (CuS)n, (Cu2S)n, and (ZnS)n small clusters (n = 1–4, 6): relation to the aggregation characteristics of metal sulfides at aqueous solutions,” *J. Mol. Model.*, vol. 25, no. 9, pp. 1–11, 2019.

[37] B. Ni, J. R. Kramer, and N. H. Werstiuk, “Atoms in molecules computational study on the molecular structure of (Cu2S)n clusters,” *J. Phys. Chem. A*, vol. 107, no. 16, pp. 2890–2897, 2003.

[38] F. Hao *et al.*, “One-step complexed preparation of nitrogen and Cu co-doped oxidative active carbon catalysts Cu-N/OAC for furfural selective hydrogenation with high yield,” *Catal. Commun.*, vol. 151, p. 106266, 2021.

[39] V. Krylova and M. Andruleviçius, “Optical, XPS and XRD studies of semiconducting copper sulfide layers on a polyamide film,” *Int. J. Photoenergy*, vol. 2009, no. Ii, 2009.

[40] M. Fan *et al.*, “An efficient nanostructured copper(I) sulfide-based hydrogen evolution electrocatalyst at neutral pH,” *Electrochim. Acta*, vol. 215, no. August, pp. 366–373, 2016.

[41] M. Li, R. Zhao, Y. Su, J. Hu, Z. Yang, and Y. Zhang, “Hierarchically CuInS2 Nanosheet-Constructed Nanowire Arrays for Photoelectrochemical Water Splitting,” *Adv. Mater. Interfaces*, vol. 3, no. 20, 2016.

[42] H. Z. and Y. W. Xiaoqian Zhao, Li Liu, Yan Zhang, “Uniquely confining Cu2S nanoparticles in graphitized carbon fibers for enhanced Oxygen Evolution Reaction,” no. December 2016, pp. 11–14, 2018.

[43] Tarachand *et al.*, “Thermoelectric properties of Ag-doped CuS nanocomposites synthesized by a facile polyol method,” *Phys. Chem. Chem. Phys.*, vol. 20, no. 8, pp. 5926–5935, 2018.

[44] J. Wang, M. M. Rahman, C. Ge, and J. J. Lee, “Electrodeposition of Cu2S nanoparticles on fluorine-doped tin oxide for efficient counter electrode of quantum-dot-sensitized solar cells,” *J. Ind. Eng. Chem.*, vol. 62, pp. 185–191, 2018.

[45] A. Rigoldi, “Sulfur chemical state at mineral surfaces - An XPS and XAES investigation,” Mar. 2011.

[46] E. Desimoni and B. Brunetti, “X-ray Photoelectron Spectroscopic characterization of chemically modified electrodes used as chemical sensors and biosensors: A review,” *Chemosensors*, vol. 3, no. 2, pp. 70–117, 2015.

[47] T. R. Gengenbach, G. H. Major, M. R. Linford, and C. D. Easton, “Practical guides for x-ray photoelectron spectroscopy (XPS): Interpreting the carbon 1s spectrum,” *J. Vac. Sci. Technol. A*, vol. 39, no. 1, p. 013204, 2021.

[48] J. Dong *et al.*, “Nitrogen-doped hollow carbon nanoparticles as efficient counter electrodes in quantum dot sensitized solar cells,” *J. Mater. Chem.*, vol. 22, no. 19, pp. 9745–9750, 2012.

[49] E. Bi, H. Chen, X. Yang, F. Ye, M. Yin, and L. Han, “Fullerene-Structured MoSe2 Hollow Spheres Anchored on Highly Nitrogen-Doped Graphene as a Conductive Catalyst for Photovoltaic Applications,” *Sci. Rep.*, vol. 5, no. March, pp. 1–10, 2015.

[50] Y. Xing, X. Zheng, Y. Wu, M. Li, W. H. Zhang, and C. Li, “Nitrogen-doped carbon nanotubes with metal nanoparticles as counter electrode materials for dye-sensitized solar cells,” *Chem. Commun.*, vol. 51, no. 38, pp. 8146–8149, 2015.

[51] G. Yue, X. Ma, W. Zhang, F. Li, J. Wu, and G. Li, "A highly efficient flexible dye-sensitized solar cell based on nickel sulfide/platinum/titanium counter electrode," *Nanoscale Res. Lett.*, vol. 10, no. 1, pp. 1–9, 2015.

[52] D. Nechiyil, B. P. Vinayan, and S. Ramaprabhu, "Tri-iodide reduction activity of ultra-small size PtFe nanoparticles supported nitrogen-doped graphene as counter electrode for dye-sensitized solar cell," *J. Colloid Interface Sci.*, vol. 488, no. March 2018, pp. 309–316, 2017.

[53] K. Sim, S. Sung, H. J. Jo, D. Jeon, and D. Kim, "Electrochemical Investigation of High-Performance Dye- Sensitized Solar Cells Based on Molybdenum for Preparation of Counter Electrode," vol. 8, pp. 8272–8281, 2013.

[54] X. Chen *et al.*, "Size-controllable synthesis of NiCoSe2 microspheres as a counter electrode for dye-sensitized solar cells," *RSC Adv.*, vol. 8, no. 46, pp. 26047–26055, 2018.

[55] M. Aftabuzzaman and H. K. Kim, "Porous Carbon Materials as Supreme Metal-Free Counter Electrode for Dye-Sensitized Solar Cells," *Emerg. Sol. Energy Mater.*, 2018.

[56] C. S. Kim, S. H. Choi, and J. H. Bang, "New insight into copper sulfide electrocatalysts for quantum dot-sensitized solar cells: Composition-dependent electrocatalytic activity and stability," *ACS Appl. Mater. Interfaces*, vol. 6, no. 24, pp. 22078–22087, 2014.

[57] H. M. Choi, I. A. Ji, and J. H. Bang, "Metal selenides as a new class of electrocatalysts for quantum dot-sensitized solar cells: A tale of Cu1.8Se and PbSe," *ACS Appl. Mater. Interfaces*, vol. 6, no. 4, pp. 2335–2343, 2014.

[58] G. Zhou, Y. Zhao, and A. Manthiram, "Dual-confined flexible sulfur cathodes encapsulated in nitrogen-doped double-shelled hollow carbon spheres and wrapped with graphene for Li-S batteries," *Adv. Energy Mater.*, vol. 5, no. 9, pp. 1–10, 2015.

[59] J. Xu, F. He, S. Gai, S. Zhang, L. Li, and P. Yang, "Nitrogen-enriched, double-shelled carbon/layered double hydroxide hollow microspheres for excellent electrochemical performance," *Nanoscale*, vol. 6, no. 18, pp. 10887–10895, 2014.

[60] H. Sun, Y. Zhu, B. Yang, Y. Wang, Y. Wu, and J. Du, "Template-free fabrication of nitrogen-doped hollow carbon spheres for high-performance supercapacitors based on a scalable homopolymer vesicle," *J. Mater. Chem. A*, vol. 4, no. 31, pp. 12088–12097, 2016.

[61] F. Bella *et al.*, "Unveiling iodine-based electrolytes chemistry in aqueous dye-sensitized solar cells," *Chem. Sci.*, vol. 7, no. 8, pp. 4880–4890, 2016.

[62] C. Justin Raj, B. C. Kim, W. J. Cho, W. G. Lee, Y. Seo, and K. H. Yu, "Electrochemical capacitor behavior of copper sulfide (CuS) nanoplatelets," *J. Alloys Compd.*, vol. 586, pp. 191–196, 2014.

[63] T. Q. Nguyen and C. Breitkopf, "Determination of Diffusion Coefficients Using Impedance Spectroscopy Data," *J. Electrochem. Soc.*, vol. 165, no. 14, pp. E826–E831, 2018.

[64] M. A. Airo *et al.*, "Probing the stoichiometry dependent catalytic activity of nickel selenide counter electrodes in the redox reaction of iodide/triiodide electrolyte in dye sensitized solar cells," *RSC Adv.*, vol. 10, no. 65, pp. 39509–39520, 2020.

[65] A. Drygala, "Influence of TiO2film thickness on photovoltaic properties of dye-sensitized solar cells," *IOP Conf. Ser. Earth Environ. Sci.*, vol. 642, no. 1, 2021.

Chapter 6

General conclusions and recommendations

6.1 Conclusions

Hollow carbon spheres were synthesized using chemical vapour deposition inside a horizontal furnace. Mesoporous silica spheres of different morphologies were used as sacrificial templates to synthesize single and double-shelled hollow carbon spheres. Different carbon sources were used to determine the better carbon source under similar synthesis parameters. From the TEM and BET results of the single-shelled HCSs, it was observed that toluene was a better carbon source as the synthesized materials exhibited thicker outer shells and higher BET surface areas. Therefore, toluene was used to prepare the double-shell HCSs. Both single and double-shell HCSs were annealed at 900 °C under Ar gas for 1 h to improve their thermal stability and purity. TGA analysis indicated that the annealing step improved the thermal stability of the single-shelled HCSs. The thermal stability of the double-shelled HCSs decreased slightly its amorphous nature. Nitrogen-doping dopants were varied to realize the better doping source that improved the catalytic properties of the carbon. Ammonia was found to be the better dopant as it led to increased surface areas of the single and double-shelled HCSs. The low surface area of double-shelled HCSs can be ascribed to the incomplete removal of the silica template or the porogen used. From these results, it was concluded that the porous single-shelled HCSs that were carbonized with toluene and nitrogen-doped with ammonia had better properties. They exhibited thicker shells that assisted with maintaining their shape, showed better stability and a higher surface for catalytic reactions.

Colloidal synthesis was employed for Cu_2S nanoparticles and the copper sources were varied to determine their effect on the morphology of Cu_2S particles. The time study showed that the nucleation for CuCl was fast and the growth process was slow compared to $Cu(acac)_2$. For $Cu(acac)_2$ the dissociation of the copper source was slow which resulted in gradual nucleation and different growth times for the particles. Both copper sources gave varied Cu_2S composition and produced particles with the same hexagonal morphology. However, particles from $Cu(acac)_2$ were significantly smaller in size compared to CuCl synthesized particles. Making them the better material for electrocatalytic properties due to their small sizes.

The electrochemical properties of the N-HCSs, Cu_2S, and Cu_2S/N-HCS composites were tested using CV. These CE materials were deposited on FTO-glass using spin coating for even distribution of the ink. Their electrocatalytic abilities were examined under similar conditions as the Pt-CE that they were compared to. The CV curves were analyzed and the N-HCS, Cu_2S, and Cu_2S/N-HCS composites showed higher current density and electrochemical double-layer capacitive current compared to Pt. Furthermore, the 25 wt% N-HCS composite had a high current density, lower peak-to-peak separation, and high electrochemical double layer capacitive current suggesting that it has good catalytic abilities. However the 75 wt% N-HCS had a high current peak density, high electrochemical double layer capacitive current, low R_s, low R_{ct}, high J_0 value, high J_{lim}, high power conversion efficiency and a high J_{sc} value. This suggests that it is the better performing composite and can potentially substitute Pt-CE in DSSCs and consequently lower the DSSCs synthesis costs.

6.2 Recommendations

- The double-shelled HCSs showed a compromised porosity. This can be mitigated by using a different porogen to make the sacrificial template. Furthermore, employing longer etching times to ensure complete removal of silica could also help to improve the porosity
- The hot injection method can be used to control the particle diameters and particle size distribution in an attempt to produce smaller monodisperse particles.
- Other methods for the preparation of the composites can be explored to improve the composite properties. For instance, an in-situ preparation of the Cu_2S nanoparticles on the surface of the HCSs may help improve the particle diameter and dispersity of the particles, as opposed to the deposition of already synthesized nanoparticles on the surface of HCSs.
- X-ray Absorption Near-Edge Structure (XANES) can be used for deeper surface analysis of the elements present and their bonding arrangements within the composites. This could help with a better understanding of the structural properties and allow for further modifications.
- The type of preparation method used to make the thin film can influence the active surface area. Therefore, it is recommended that other thin-film fabrication methods can be assessed in order to evaluate changes in the current densities and peak-to-peak separations.
- Using different conductive substrates such as indium tin oxide (ITO) to thoroughly evaluate the photovoltaic performances composite as CE materials.
- More importantly, the overall fabrication of the solar cells needs to be optimized.

Supplementary figures

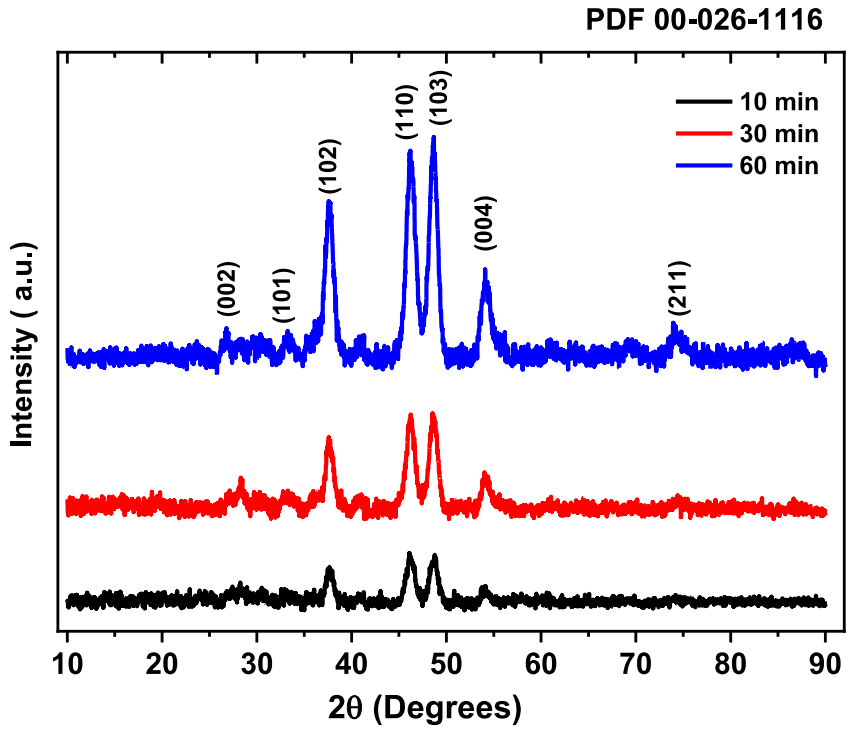


Figure S4.1: XRD pattern of as-synthesized copper sulfide particles at various reaction times of 10, 30, and 60 min using CuCl as a Cu precursor.

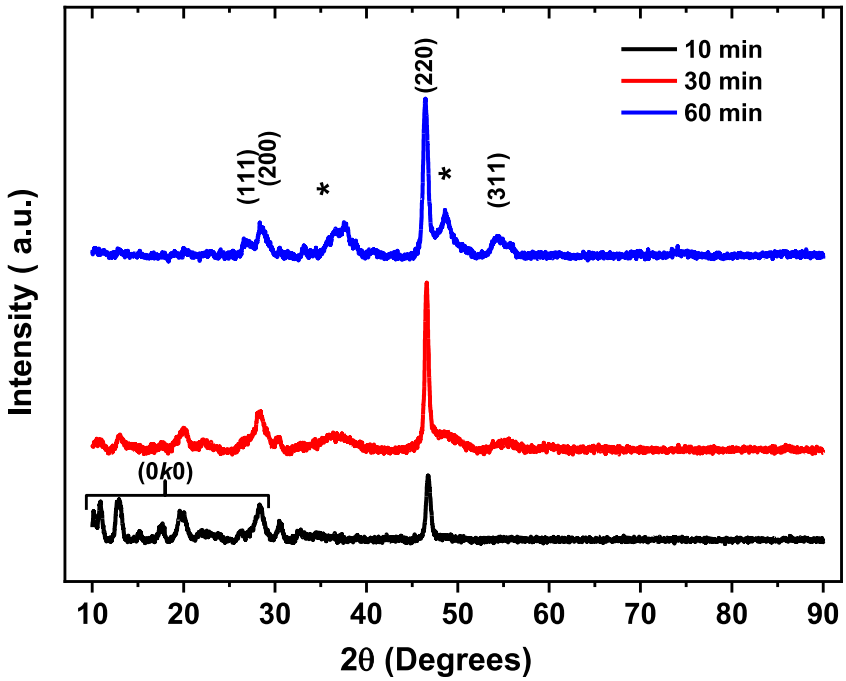


Figure S4.2: XRD pattern of as-synthesized copper sulfide particles at various reaction times of 10, 30, and 60 min using $Cu(acac)_2$ as a Cu precursor.